2013

Bench-Top Validation of "Intelligent" Mouth Guard

Alper Aksu
Cleveland State University

BENCH-TOP VALIDATION OF "INTELLIGENT" MOUTH GUARD

ALPER AKSU

Bachelor of Science in Electrical and Electronics Engineering

Bahcesehir University

June, 2011

Submitted in partial fulfillment of requirements for the degree

MASTER OF SCIENCE IN BIOMEDICAL ENGINEERING

at

CLEVELAND STATE UNIVERSITY

June, 2013

This thesis has been approved

for the Department of Chemical and Biomedical Engineering

and the College of Graduate Studies by

_____

Thesis Chairperson, Dr. Adam J. Bartsch

Department of Spine Research Laboratory, Cleveland Clinic

_____

Date

_____

Dr. Sridhar Ungarala

Chemical and Biomedical Engineering Department, Cleveland State University

_____

Date

_____

Dr. Murad Hizlan

Electrical and Computer Engineering Department, Cleveland State University

_____

Date

_____

Dr. Majid Rashidi

Mechanical Engineering Department, Cleveland State University

_____

Date

ACKNOWLEDGMENT

It is a pleasure to thank those who made this thesis possible. I would like to thank Dr. Orhan Talu and Dr. Joanne Belovich, who guide me whenever I need. I also thank my colleagues Dr. Prasath Mageswaran, Basar Aka, Caglar Ozturk and Victor Perhay for their contributions during my master thesis progress.

Lastly, I offer my regards and blessing to all of the people, especially Rebecca Laird and Darlene Montgomery, who do not hesitate to make my life easier.

BENCH-TOP VALIDATION OF "INTELLIGENT" MOUTHGUARD

ALPER AKSU

ABSTRACT

Concussion is the signature athletics injury of the 21st Century. Scientists are hard at work monitoring effects of hard impacts on the human brain. However, existing tools and devices are inadequate to screen the effects. Hence, a new approach is required to accurately quantify peak values of head impacts or concussions and relate these values to clinical brain health outcomes.

A new head impact dosimeter, the "Intelligent Mouth Guard" (IMG) has been developed and can be conveniently located inside the mouth. In this study, the IMG printed circuit board (PCB) including four (4) high-quality shock resistant sensors has been developed and implemented as a tri-axial impact analyzer in a mouthpiece. The bench-top validation process of the IMG was divided into theoretical uncertainty analysis of linear accelerometers, theoretical uncertainty analysis of angular rate sensors, bench-top uniaxial impact testing of linear accelerometers and bench-top uniaxial static testing of angular rate sensors.

More specifically, this study also presents a method based on National Bureau of Standards (NBS) of analyzing measurement error for any components of a specialized electrical circuit and any types of data acquisition system. In the current application of an IMG printed circuit board (PCB), utilized for linear acceleration, angular acceleration and angular velocity measurements, has sensor uncertainties quantified. The uncertainty model is branched into two parts: The bias error (B) and

the random error (R). In this paper, expected measurement error types for PCB components (ADXL001 linear accelerometer, L3G4200D gyroscope) are quantified and their effects on the IMG system are computed. The uncertainty analysis presented here can be a guide in future in vitro and in vivo IMG validation tests.

During bench-top testing, IMG linear accelerometers quantified peak linear acceleration with 98.2% accuracy and 98.0% precision. The IMG gyroscope quantified peak angular velocity with 97.0% accuracy and 99.7% precision.

In summary, the results showed that the IMG may possess adequate sensors to fulfill the expectations relevant to head concussion diagnosis with a known uncertainty. Future work should involve improvement for optimum data analysis and filtering methods, further validation testing, including in vitro and in vivo tests.

TABLE OF CONTENTS

LIST OF TABLES

LIST OF FIGURES

CHAPTER I

INTRODUCTION

The brain is one of the most essential organs of the human body. It is directly connected to nerve cells that transmit signals, which tell which organ needs to do what in which conditions, into muscles or corresponding parts of the body. Simply, it works like a remote controller. These properties make the brain an indispensable part of the body. Thus, it is required for humans to protect the head and neck against all kinds of impact. However, it is impossible to get a 100% protection of head impacts in some cases, especially in sports games, wars and traffic accidents. As the results of hard impacts, two kinds of brain injury can be commonly seen: focal brain injuries (FBI) and diffuse brain injuries (DBI). Focal brain injuries are seen when head contact occurs. Diffuse brain injuries are seen because of sudden head rotations[1]. Moreover, diffuse axonal injury (DAI), is a more serious level of FBI, is the most common type of traumatic brain injury (TBI). DAI generally causes coma or stroke, after head trauma[2]. These conditions emphasize that there is a need to quantify the effect of an impact on the brain leading to numerous dysfunctions of the nervous system like short-term unconsciousness and coma. Furthermore, according to the research regarding the effects of head impact on the brain, it does not have to be a hard hit for causing serious nervous diseases such as Parkinson's, Alzheimer's or Dementia

Pugilistica[3]. In other words, a healthy sportsman can even have a nervous disease after his retirement, because of the head impacts he sustained during his sports career. This is why it is necessary to monitor the consequences of all head strikes on the human brain. In light of these problems, in order to measure the severity of brain injuries, scientists and engineers at Cleveland Clinic are designing a head impact dosimeter named "Intelligent Mouth Guard (IMG)".

Figure 1.1 Prototype of Intelligent Mouth Guard Version 3.1 (v3.1)

The IMG will be capable of quantifying the peak and temporal values of different types of head impact or concussion. The goal is to give the results of both linear acceleration, in the unit of gravitational force (g), and angular velocity (rad/s), including the time interval (ms) of each head concussions with the goal of less than 5% error. It is also likely to calculate the harmonics of impact frequency, force and moment characteristics of an impact with a simple Matlab code. These properties may make the IMG a premier tool to determine the reliability of head protectors, like helmets, used in many sports games, as well as in the army.

Before IMG can be trusted to measure head impacts in live humans, the IMG measurement uncertainty must be quantified. Therefore, the purpose of this project was to calculate the theoretical uncertainty, and quantify the experimental uncertainty, of the kinematic sensors being used in IMG. This uncertainty quantification methodology will also be useful in future IMG versions should the kinematic sensors change.

BACKGROUND

Statistics

There are several studies to investigate statistically the frequency of head concussion occurred in both sports games and traffic accidents. According to Fuller et al. (2005), 163 head and neck injuries have been detected in twenty Federation Internationale de Football Association (FIFA) tournaments played between 1998 and 2004[4]. He also realized that 30% of total challenges were directly against a player's head. According to another Fuller's study (2004), 8572 tackles have been detected in the videos of 123 international matches. During these games, 78% of total jumping tackles were not declared foul. However, 65% of them required medical attention[5]. These results show referees did not pay enough attention to head contacts in soccer games. Consequently, the number of head injuries increased.

According to Gerbeding et al.'s (2003) study, 1.12 million mild TBI (MTBI) cases, occurred in sports games, such as American Football, hockey, and boxing, are annually reported[6]. In Newman et al.'s (2005) study, 182 head impacts were observed,

both with and without mild TBI, by the National Football Leagues (NFL) Injury Surveillance System from 1997 to 2002. Briefly, numbers in the table show that the most harmful injuries were seen due to head-to-head impacts (**Table 1.1**).

Impact Configuration	Incidents on video	Reconstructions		
		Subtotal	MTBI	Non-MTBI
Head-to-Head	92	27	22	5
Head-to-ground	31	4	3	1
Head-to-body part	44	-	-	-
Unknown contact	15	-	-	-
Total	182	31	25	6

Table 1.1 Distributions of incidents in the NFL-MTBI reconstruction database[7]

In order to realize the importance of head concussions in daily life, Kerrigan et al.'s (2009) study points that the most commonly reported injuries are head injuries reported by pedestrians struck by vehicles[8,9,10,11,12,13]. Additionally, the Centers for Disease Control and Prevention (CDC) believe that 50,000 people in the US die each year because of TBI[14]. Crashworthiness Data System (NASS-CDS) estimates that the cost of head injuries, occurred from 1997 to 2003, is about $6 billion[15].

Rigid Body Equations of Motion (EOM)

As mentioned in Introduction section, IMG will has potential to detect head impacts with very short time duration, ranging from 5-25 ms. In order to measure the effects of head impacts on head center of gravity (cg), rigid body equations of motion (EOM) were utilized to consider the relationship between mouth and head

accelerations. In fact, it is known that the distance between human teeth and head cg is not constant because brain and skull are two non-rigid parts of human body. This means the rigid body assumption for this situation is incorrect. However, as a first attempt, using rigid body assumption was relatively more appropriate for this project to make all related calculations simple by eliminating all Coriolis terms. A similar calculation procedure has been in place for many decades and is commonplace when studying head impacts to humans.

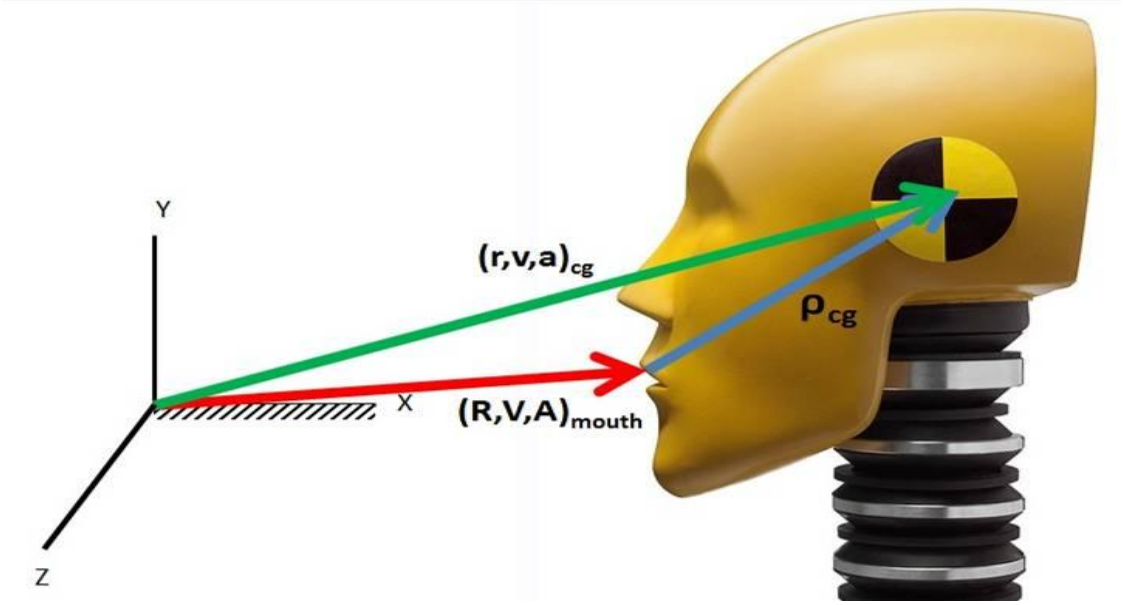

Figure 1.2 Vectorial Notation of Relation between Mouth and Head Accelerations Based on Rigid Body Assumption

Related Equations of Motion

For Rigid Body EOM

$$r_{cg} = R_{mouth} + \rho_{cg}$$

$$v_{cg} = V_{mouth} + (\tilde{\omega} \times \rho_{cg})$$

$$a_{cg} = A_{mouth} + (\tilde{a} \times \rho_{cg}) + (\tilde{\omega} \times \tilde{\omega} \times \rho_{cg})$$

For Non-Rigid Body EOM

$r_{cg} = R_{mouth} + \rho_{cg}$

$v_{cg} = V_{mouth} + (\tilde{\omega} \times \rho_{cg}) + \boxed{\rho_{cg}'}$ => (Coriolis Term)

$a_{cg} = A_{mouth} + (\tilde{a} \times \rho_{cg}) + (\tilde{\omega} \times \tilde{\omega} \times \rho_{cg}) + \boxed{2 * \tilde{\omega} \times \rho_{cg}' + \rho_{cg}''}$ => (Coriolis Terms)

For rigid body assumption; ρ_{cg} is constant, so $\rho_{cg}' = \rho_{cg}'' = 0$

IMG Hardware

The Intelligent Mouthguard Printed Circuit Board (IMG PCB) consists of three single-axis microelectromechanical systems (MEMS) linear accelerometers (ADXL001-250, Analog Devices, Norwood, MA, USA), one three-axis MEMS angular rate sensor (L3G4200D, ST Microelectronics, Texas, USA), one microcontroller (dsPIC33FJ128GP804, Microchip Technology Inc., Arizona USA) one 1Megabit Serial Peripheral Interface Memory Module (25AA1024 EEPROM Microchip Technology Inc., Arizona, USA), powered by a lithium polymer battery (Full River Battery Manufacture Company, Ltd., Guang Zhou City, China), all mounted to a flexible PCB (PCB FAB Express, Sunnyvale, California).

In terms of linear accelerometers, ADXL001 linear accelerometers were mounted on three different sides of the IMG PCB. Some properties of the accelerometer are shown below:

- 70-500 g wideband range available
- 22 kHz resonant frequency structure
- Low noise: 4 mg per Hz
- Low Power Consumption: 2.5 mA

The measurement principle of ADXL linear accelerometer is simply based on a change in capacitance. Displacement of the sensor frame changes the capacitance of plate capacitors. The change in capacitance is measured by on-chip circuitry. These properties make ADXL001 a good option for using in the IMG PCB (**Figure 1.3**).

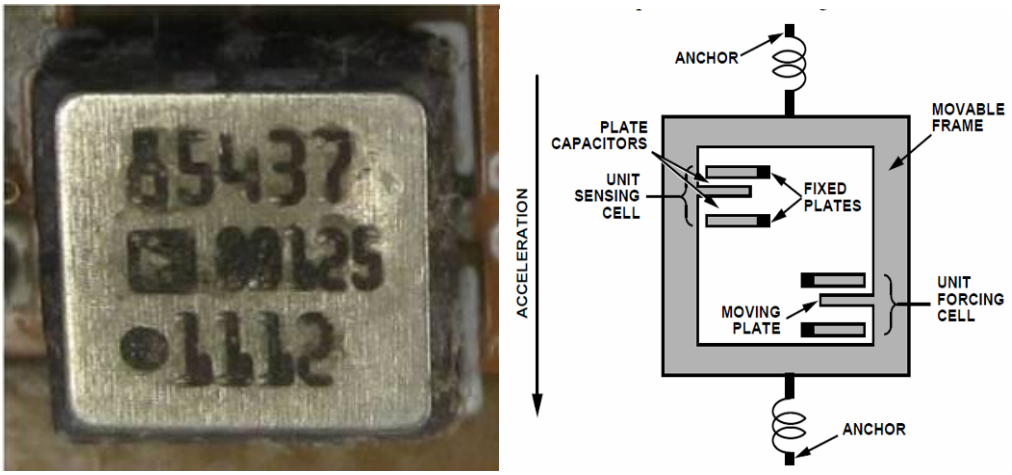

Figure 1.3 Analog Devices ADXL001 MEMS Linear Accelerometer on board (**left**) and Illustrating Internal Architecture with Sensitive Axis (**right**)

The L3G4200D gyroscope is low cost and its properties are shown below:

- Three selectable full scales (FS): 4.25/8.50/34.9 radians per second (rad/s)
- High shock survivability
- Low voltage-compatible (IOs 1.8 V)
- Embedded temperature sensor with the temperature range (-40^{o} to 85^{o})
- Integrated low and high pass filters with user-selectable bandwidth
- 6.1 mA supply current

These properties, especially selectable full scale options, provided high flexibility to measure rotational motion detected by the IMG gyroscope (**Figure 1.4**).

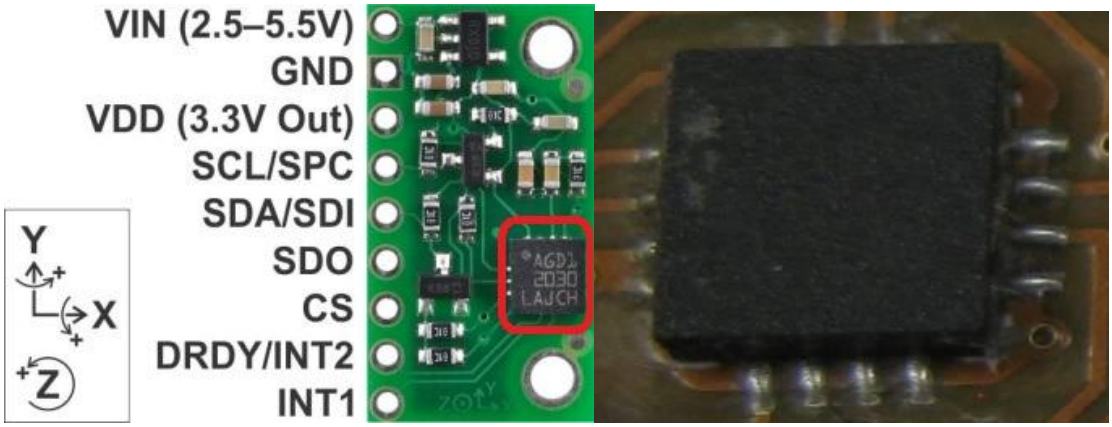

Figure 1.4 L3G4200D Three-Axis Gyroscope Mounted on A Test Board with Sensing Axes and Circled (**left**) and Gyroscope Chip on IMG PCB with Connections (**right**)

In regards to the on-board microcontroller, (dsPIC33FJ128GP804) DSC High-Performance 16-bit Digital Signal Controller was utilized (**Figure 1.5**). The dsPIC33FJ128GP8 was chosen because of a powerful central processing unit (CPU) and peripherals for serial communication, analog to digital (A/D) conversion, direct memory access (DMA), timers, interrupt controller and digital input/output (I/O).

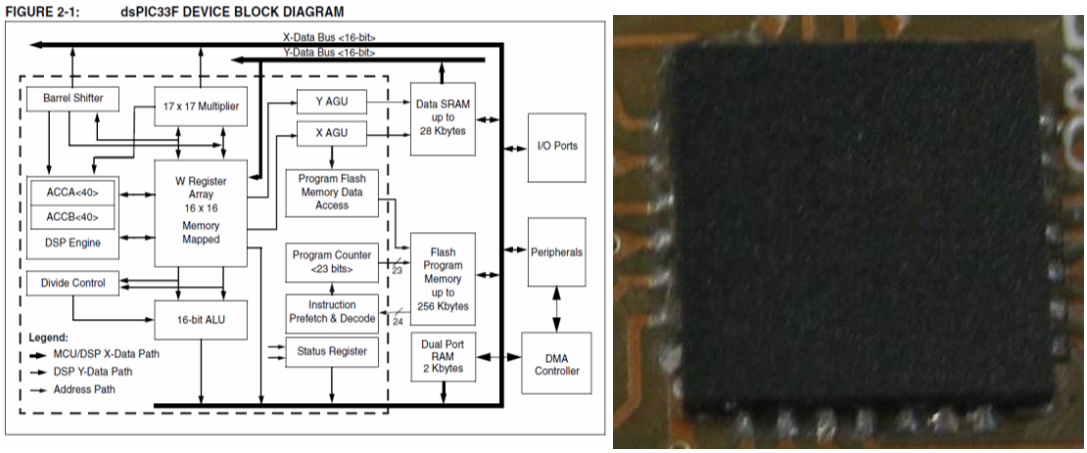

Figure 1.5 Internal Architecture of dsPIC33FJ128GP804 Microcontroller (**left**) and Microcontroller on IMG PCB with Connections (**right**)

In order to store the collected data, a memory module, 25AA1024 EEPROM was used. Some features of the EEPROM are shown below:

- Maximum Write Current: 5 mA at 5.5 V, 20 MHz
- Read Current: 7 mA at 5.5 V, 20 MHz
- Standby Current: 1 µA at 2.5 V (very low power consumption)
- Non-Volatile Memory

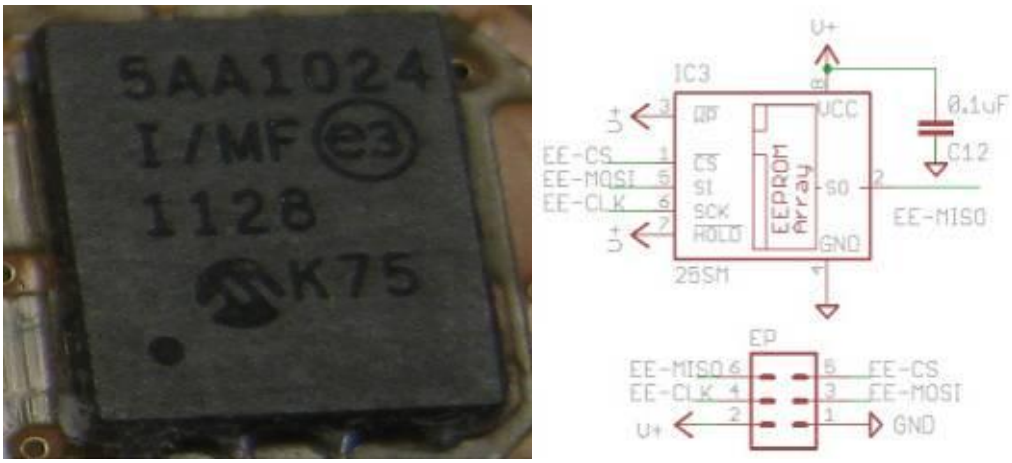

Figure 1.6 Microchip Inc. 25AA1024 EEPROM on test board (**left**) and its schematics (**right**)

In the first version of the IMG PCB (v3.0), EEPROM was not used and that sometimes caused loss of data. Hence, this non-volatile memory module was located on the next IMG PCB versions (v3.1 and later) to prevent data loss.

A small 130mAh lithium polymer battery was also mounted on the IMG PCB (**Figure 1.7**). It provides all required power for the IMG PCB, up to 4 hours of data collection on a single charge, and the serial connector was used to download up to 250 total events after testing.

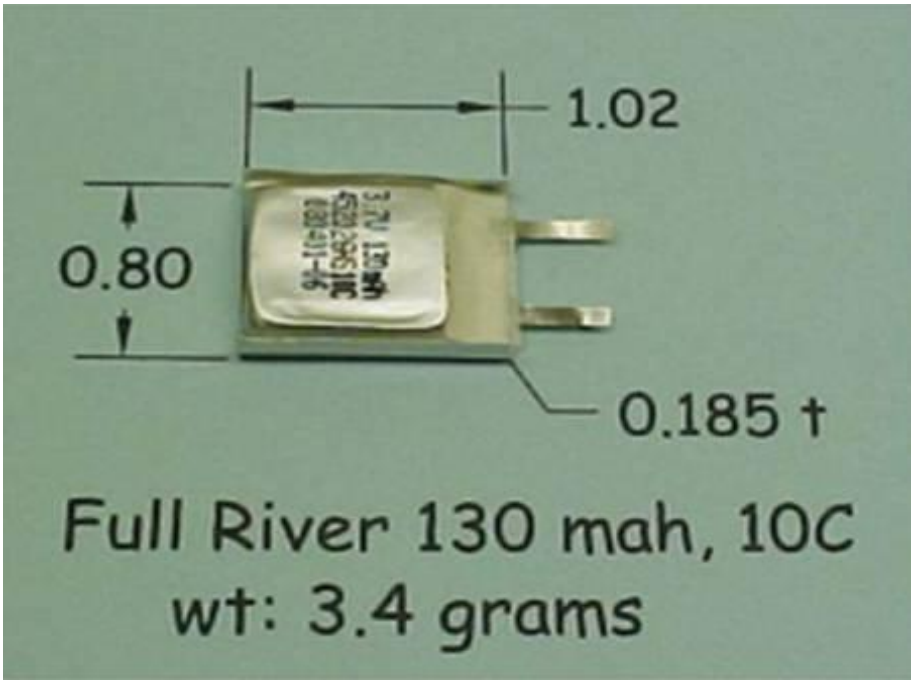

Figure 1.7 IMG PCB Lithium Battery, Physical and Technical Properties

In the first part of validation process, flexible PCBs were utilized for IMG performance tests. Flexible PCBs are resistant to any kinds of bending. Therefore, it was considered that new version of IMG will be durable against chewing, squeezing and stretching (**Figure 1.8**).

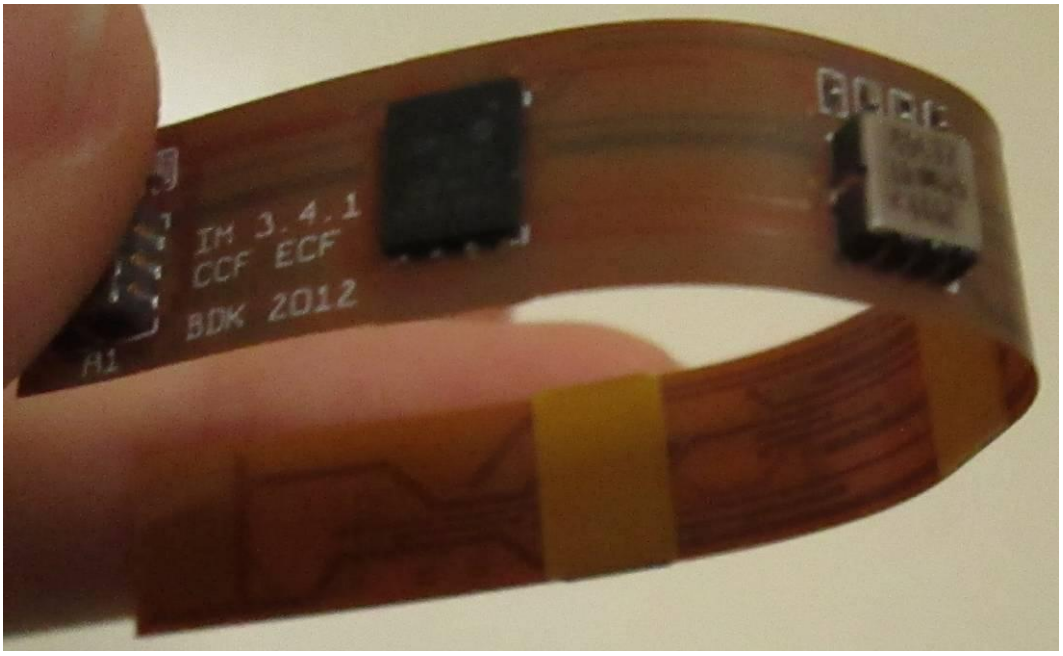

Figure 1.8 Flexible IMG Printed Circuit Board (v3.4)

Consequently, complete IMG PCB v3.4 consists of three single-axis linear accelerometers, one three-axis angular rate sensor, one microcontroller, one EEPROM, and one lithium battery (**Figure 1.9**).

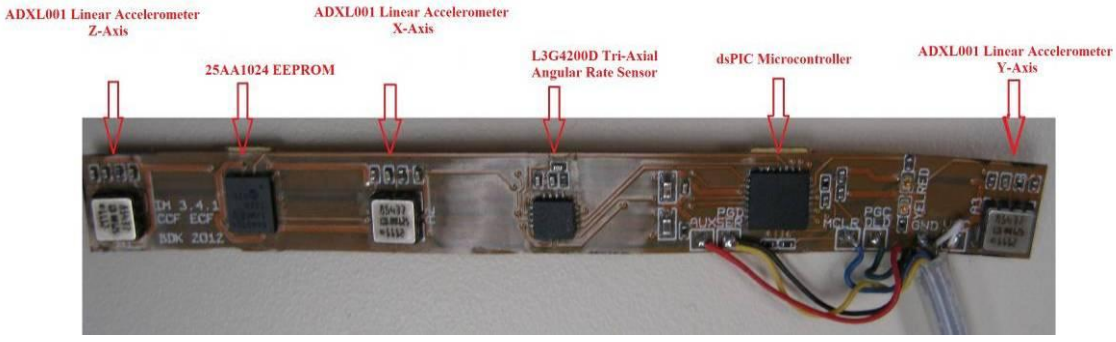

Figure 1.9 Complete IMG PCB v3.4

IMG Firmware

In regards to the system firmware, IMG firmware is based on an Assembly language, which provides relatively faster code execution time than the same sort of programming languages. This code controls sampling rate of IMG sensors, how to store collected data, and intensity and color of LED indicator (**Figure 1.10**). IMG firmware also allows user to modify sampling rate, pre-triggering time, sampling duration and trigger threshold value for each individual test.

Figure 1.10 IMG LED Blinking Yellow When It Works (**left**) and Blinking Red When It is Triggered (**right**).

IMG Data Acquisition Components

In order to transmit data from IMG PCB to a computer, a simple data transmission tool, also called IMG PC Interface, was developed by the Cleveland Clinic Electronics Core. The data transmission tool consisted of a black USB cable and a blue serial port cable to hook up to the IMG PCB serial port input located on the battery pod. These two cables were connected into an adaptor (**Figure 1.11**).

Figure 1.11 IMG PC Interface

The IMG battery is also capable to be charged via USB connection. An LED indicator on the IMG PC Interface Adaptor shows whether IMG is fully charged or not. The LED is on when IMG Battery is connected to a PC or a laptop to be charged and automatically turns off when IMG is fully charged (**Figure 1.12**).

Figure 1.12 LED Located in IMG PC Interface is on (**left**) and off (**right**)

Methodology to Determine IMG Sensor Accuracy and Precision

Accuracy and precision are two essential issues for impact measurements because impact suddenly occurs, in a range between 5-25 milliseconds (ms), and accurately and precisely measuring kinematics parameters like peak linear acceleration and angular velocity is challenging.

Accuracy is defined as how close the measured value to the true value is. In this project, reference sensor measurements are accepted as true values and IMG measurements are accepted as measured values.

Precision, also called reproducibility and repeatability, is defined as the closeness of the results of repeated measurements under the same conditions. In order to determine precision of a data set, dispersion of data points should be considered. In statistics, the dispersion of a mass or a cluster is quantified in a specific range, also called standard deviation. Standard deviation is a statistical method to determine the randomness of a bunch of related quantities. Engineering practice generally prefer 2-sigma (σ) standard deviation to other sigma values because it corresponds to 95.4% confidence interval (CI) for a set of number, which means that when a test is repeated under the same conditions, at least 95 of 100 collected data points from the same sensor should remain in the estimated region (**Figure 1.13**).

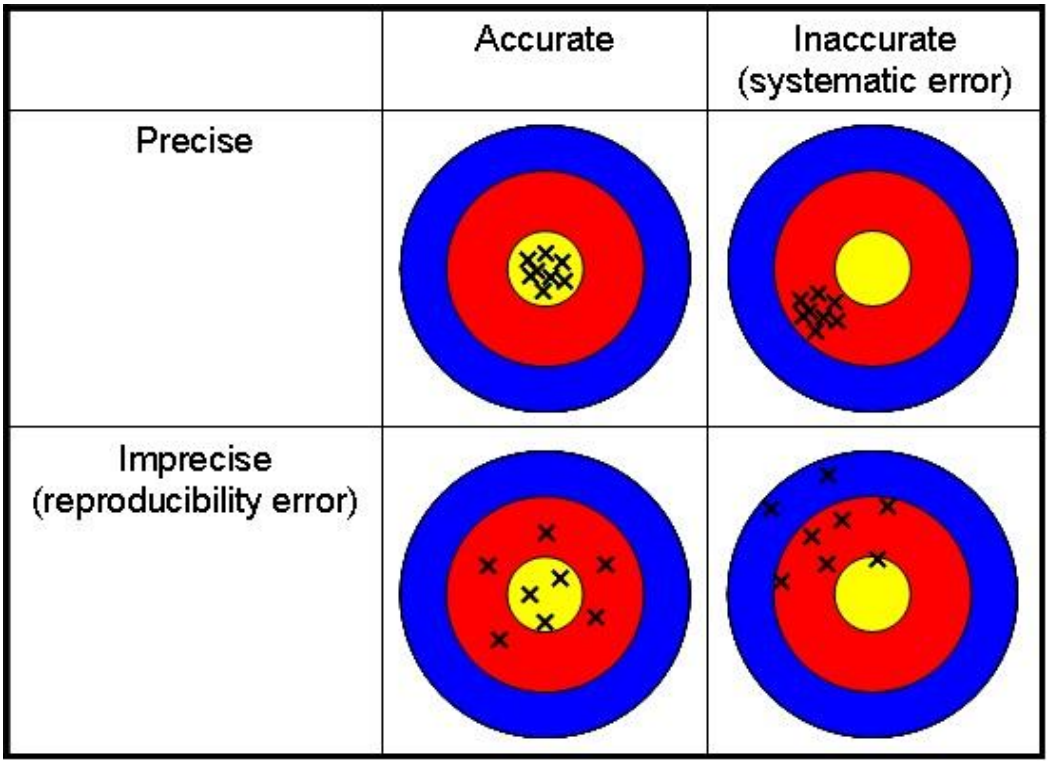

Figure 1.13 Illustration of Accuracy and Precision. High Accuracy and High Precision (**Upper Left**) are desired.

In light of these definitions, in order to quantify IMG linear accelerometer and angular rate sensor accuracy and precision, measurements from IMG PCB mounted sensors (ADXL001, L3G4200D) were compared with reference sensors (64B, ARS) in two types of tests. In the first set of tests, the IMG linear accelerometers were mounted on a sliding plate and dropped onto pads with several stiffness values to generate linear accelerations ranging from -500g to 500g. During these drop tests, reference linear accelerometers (Model 64B – Measurement Specialties, Hampton, VA, USA) were also attached to the sliding plate with their sensitive axes aligned with the IMG linear accelerometers.

The Model 64B reference linear accelerometer is a highly sensitive piezo-resistive accelerometer typically used in impact tests. This accelerometer also meets the SAE J211 standards for dynamic impact tests[16]. This sensor is capable of

measuring linear accelerations up to 500g. It works over the temperature range of 0°C to + 50°C, and has a Wheatstone bridge circuit with fixed resistors (**Figure 1.14**).

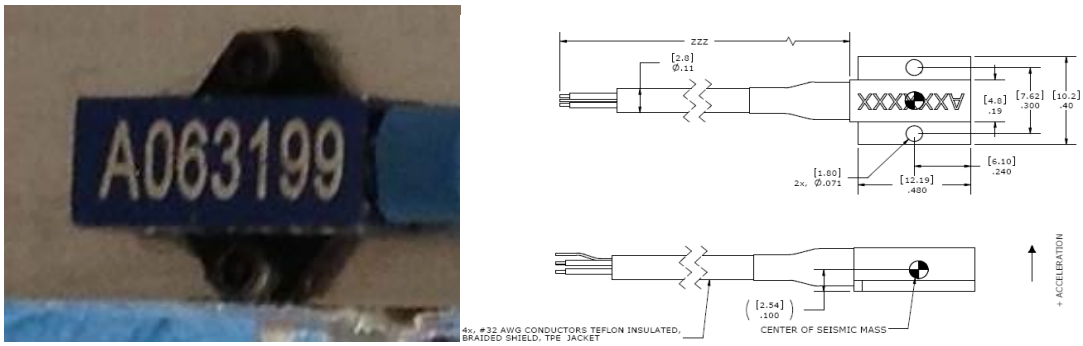

Figure 1.14 Model 64B Reference Linear Accelerometer Top View (**right**) and Its Dimensions and Sensitive Axis (**left**)

Uncertainty Analysis

According to related sources in literature, even though there are several methods to determine uncertainty of a system, there is no unique way to determine uncertainty. However, uncertainties in a system are generally divided into three parts in terms of uncertainty sources: Methodology uncertainty, measurement uncertainty, and personnel uncertainty. Uncertainty due to methodology may be defined as using an inappropriate test setup for a desired test goal. For example: in order to test a single axis linear accelerometer, a test setup provides linear or uniaxial motions should be designed. Uncertainty due to measurement may involve sensor uncertainty, dedicated data acquisition system uncertainty, uncertainty due to test environment, etc. Personnel uncertainty can be defined as uncertainty due to human acts like hand shaking or lack of concentration when performing tests. Total system uncertainty is equal to summation of these three uncertainty types. In my project, I assumed neither

methodology nor personnel uncertainty was involved into total uncertainty of the system. Therefore, total uncertainties of dedicated test setups were equally set to measurement uncertainties of them.

In any measurement system, there are three types of measurement uncertainty, bias (B), and random (R). If an uncertainty affects a system either only positively or only negatively and it is also eliminative and its effect is predictable, this uncertainty is a bias uncertainty that can be removed. For example: the effect of gravitational force on linear accelerometers is a bias uncertainty that can be removed. In my project, zero-g-bias of a sensor was classified as an absolutely constant elementary uncertainty. Absolutely constant elementary uncertainty is a type of bias uncertainty that is constant for all tests performed with the same sensor. Figure 1.15 provides a graphical description of normally distributed test data with and without bias uncertainty.

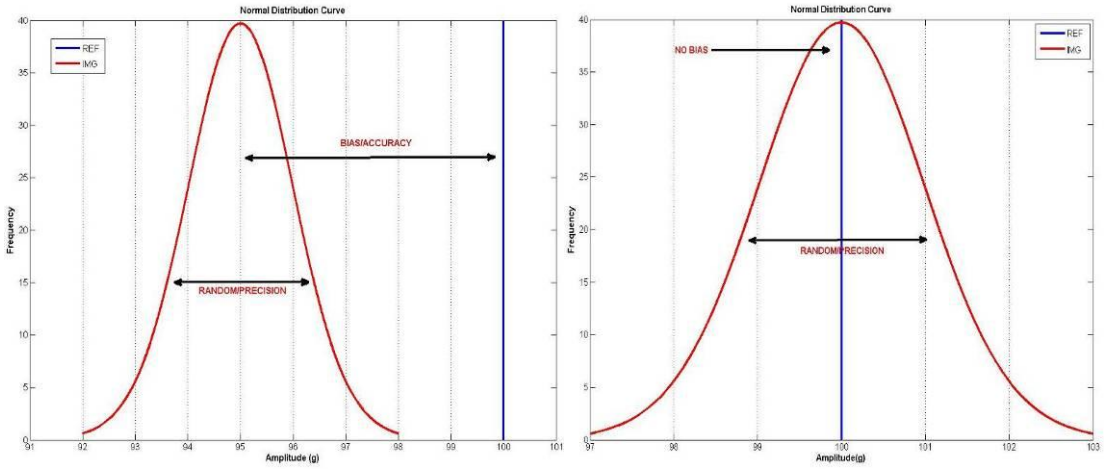

Figure 1.15 Illustration of Normally Distributed Sensor Measurements with (**top**) and without Bias Uncertainty (**bottom**)

On the other hand, if the effects of an uncertainty are varying among different tests (sometimes positive and sometimes negative), this is a random uncertainty[17]. For

example: electrical noise in IMG data is a random noise (**Figure 1.16**). There are also sub-random types, such as conditionally constant elementary uncertainty, purely random uncertainty, and quasi-random uncertainty. Conditionally constant elementary uncertainty is a type of random uncertainty that affects only one side of measurement (only positive or only negative), and its effect varies among tests. Purely random uncertainty is a type of another random uncertainty that may affect two sides of measurement (both positive and negative). Electrical noise is a good example of purely random uncertainty.

In contrast to experimental uncertainty, theoretical uncertainty analysis is conducted to predict possible measurement ranges due to all possible uncertainty sources before the start of testing. In other words, theoretical uncertainty analysis is pre-analysis, and experimental uncertainty analysis is post-analysis of system uncertainty.

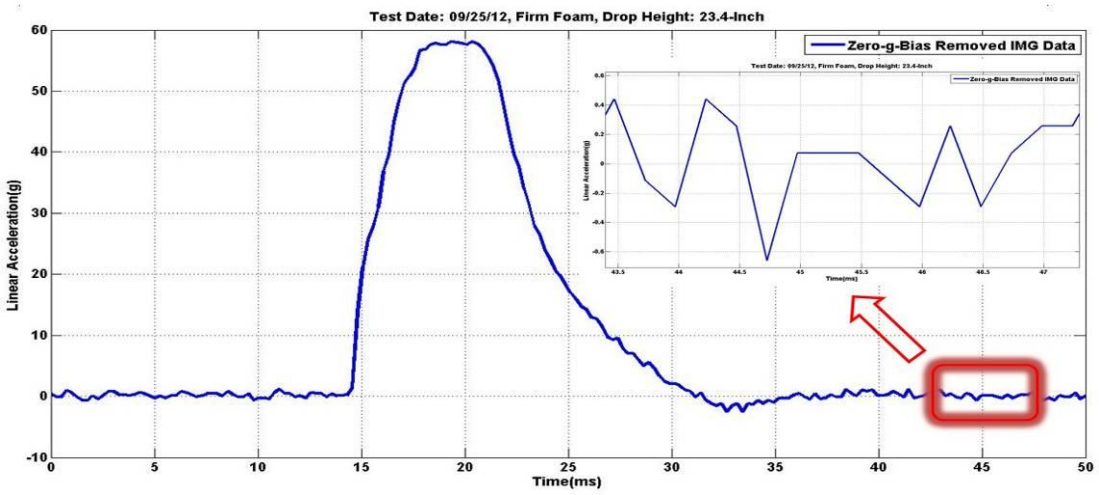

Figure 1.16 A Closer View of Random Noise in IMG Data

According to the related literature search, total system uncertainty can be defined as the difference between the true quantity and the measured quantity. In this project, reference sensor measurements (64B, ARS) were accepted as true quantities and IMG measurements (ADXL001, L3G4200D) were accepted as measured quantities. In order to provide a better explanation about calculations of total system uncertainty, related calculations are presented below:

$$U_{tot} = U_{met} + U_{meas} + U_p \quad (1)$$

Where;

U_{tot} = Total System Uncertainty,

U_{met} = Methodology Uncertainty,

U_{meas} = Measurement Uncertainty,

U_p = Personnel Uncertainty.

It is assumed U_{met} and U_p are equal to zero. Hence,

$$U_{tot} = U_{meas}$$

In summary, the method to calculate bias and random uncertainties has the steps listed below:

1) Determine the purpose of measurement and desired measurement uncertainty.

2) Consider the properties of measuring instruments employed.

3) Compile the list of possible uncertainties with estimated limits.

4) Determine dominant uncertainty sources.

5) Make sure that all uncertainty sources are independent.

6) Determine whether bias or random uncertainties are present.

7) Take the mean value of multiple measurements performed under the same conditions.

8) Make theoretical (pre) and experimental (post) estimations of uncertainty.

9) Present total system uncertainty as $\mathbf{U_{tot} = U_B\% \pm U_R\%}$ **(Worst Case)**

The next step is about how to combine the uncertainties determined in the previous section. In this study, the root sum square (RSS) method was chosen to combine the same type of uncertainties[18]. RSS method calculates square root of summation of squares of each uncertainty term. Another commonly used method to calculate system uncertainty is Monte Carlo Simulation. This method uses partial differential equations to determine systemic bias and precision[19]. However, based on engineering judgment, the RSS method was used in this project as a first approach. Future uncertainty analyses may make use of Monte Carlo Simulation or more sophisticated uncertainty methods.

Thus, in order to calculate bias uncertainty using RSS method, equation 1 is shown below to account for 1, 2…k bias uncertainties:

$$U_B = \left[B_1^{\,2} + B_2^{\,2} + ... B_k^{\,2}\right]^{\frac{1}{2}} \qquad (1)$$

Similarly, one would use the same RSS equation to calculate random uncertainty:

$$U_R = \left[R_1^{\,2} + R_2^{\,2} + ...R_k^{\,2}\right]^{\frac{1}{2}} \quad (2)$$

After calculating bias and random uncertainty RSS values, the 95% confidence interval system uncertainty with 99.7% coverage (U_{t1}), referred to in this project as the worst case, can then be found via the equation shown below:

$$U_{t1} = U_B + U_R \quad \Rightarrow 99.7\ \%\ \text{Coverage (Worst Case)} \quad (3)$$

Additionally, another uncertainty term, called U_{t2}, was considered to calculate total system uncertainty. U_{t2} is simply based on an assumption that bias uncertainty can be removed post-hoc. In other words, U_{t2} is equal to U_R.

$$U_{t2} = U_R \quad \Rightarrow 95.4\ \%\ \text{CI} \quad (4)$$

The confidence interval simply represents the reliability of an estimate for consecutive tests performed under the same conditions such as ambient temperature, drop height, impacting material, etc. Briefly, it is estimated that the results of 95 of 100 drop tests performed under the same conditions should remain in the estimated

uncertainty range. As shown in Figure 1.17a, the 95% confidence interval encompasses approximately ± 2 standard deviations (σ) with a systematic bias.

As seen in Figure 1.17, for the t distribution, 95% CI encompasses approximately ± 2 standard deviations (σ) with systematic bias removed signal.

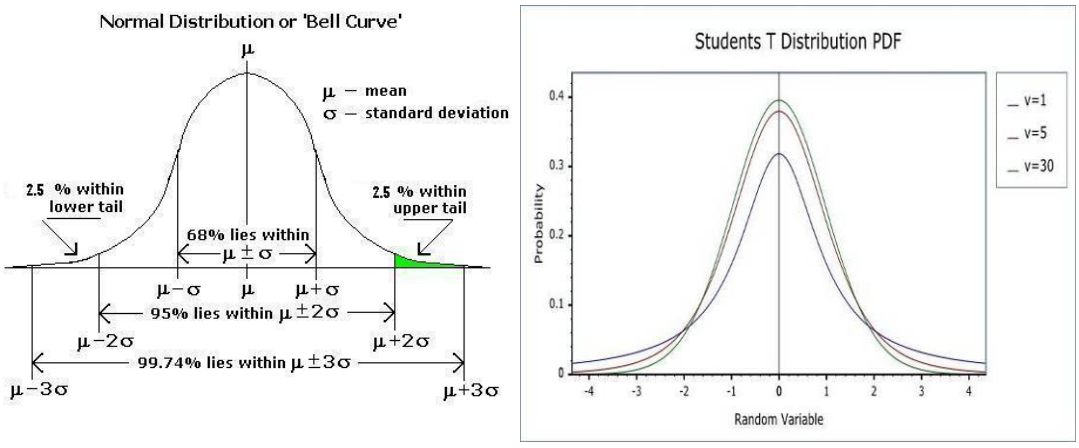

Figure 1.17 Simple Descriptions of Mean Values and Confidence Intervals **(left)**, and Standard Deviation (σ) in Normal Distribution (**right**)

CHAPTER II

IMG THEORETICAL UNCERTAINTY ANALYSIS

ADXL001 Linear Accelerometer Theoretical Uncertainty Analysis

Methodology

In this study, IMG PCB and reference sensors were used as two impact detectors. In order to determine IMG PCB measurement accuracy and precision, reference sensors were utilized as the true value and IMG sensors as THE measured value.

According to the datasheet provided by Analog Devices (**1/09—Revision 0: Initial Version**), individual ADXL001 linear accelerometer uncertainties were quantified by the manufacturer. For analyzing the ADXL001 linear accelerometer, it was assumed that uncertainties based on a large number of test samples (n>30) will allow for use of 95% CI individual uncertainty values. The possible uncertainties due to ADXL001 linear accelerometer were listed and the types of uncertainties were determined with respect to their effects on the IMG PCB measurements (**Table 2.2**).

Uncertainties	Uncertainty Type	Description
Non-Linearity	Random	Inconsistency of the ratio between the output voltage and INPUT loading
Cross-Axis Sensitivity	Random	The measure of how much output is seen on one axis when acceleration is imposed on orthogonal axis
Low Noise	Random	Random deviation of the signal
Sensitivity	Bias	The ratio of change in output signal (mV) divided by input (acceleration-g)
Zero-g-Bias	Bias	The output level when there is ZERO input
Frequency Response	Bias	Measurement of the output level of a device at difference EXCITATION frequencies
Sensitivity due to Temperature Change	Bias	The effect of ambient temperature on sensor sensitivity

Table 2.2 The List of Uncertainties Due to ADXL001 Linear Accelerometer

The cross-axis sensitivity directly affects the total uncertainties due to ADXL001 linear accelerometer, but the effect on bias or random uncertainty is a function of cross-axis linear acceleration. For example, an acceleration to be

measured in the X-axis will still measure some undesirable output from Y-axis and Z-axis accelerations acting orthogonal to the sensor. This term will be accounted for after the bias and random uncertainties are quantified.

Non-linearity

In order to calculate the effect of each term on total uncertainty, related numbers and histograms in the ADXL001 datasheet states non-linearity is typical ±0.2% and maximum ±2% of FS. For uncertainty calculations, even though non-linearity is given as a rectangular distribution, it will be assumed that the 95% CI (±2σ) for non-linearity is ±2%.

Parameter	Conditions	ADXL001-70			ADXL001-250			ADXL001-500			Unit
		Min	Typ	Max	Min	Typ	Max	Min	Typ	Max	
SENSOR											
Nonlinearity			0.2	2		0.2	2		0.2	2	%
Cross-Axis Sensitivity	Includes package alignment		2			2			2		%
Resonant Frequency			22			22			22		kHz
Quality Factor			2.5			2.5			2.5		

Figure 2.18 Non-Linearity Uncertainty of ADXL001 Linear Accelerometer

Sensitivity

For calculating uncertainty due to sensor sensitivity, the same specification sheet has been utilized, as well as a related histogram.

Parameter	Conditions	ADXL001-70			ADXL001-250			ADXL001-500			Unit
		Min	Typ	Max	Min	Typ	Max	Min	Typ	Max	
SENSOR											
Nonlinearity			0.2	2		0.2	2		0.2	2	%
Cross-Axis Sensitivity	Includes package alignment		2			2			2		%
Resonant Frequency			22			22			22		kHz
Quality Factor			2.5			2.5			2.5		
SENSITIVITY											
Full-Scale Range	$I_{OUT} \leq \pm 100$ µA	−70		+70	−250		+250	−500		+500	*g*
Sensitivity	100 Hz		16.0			4.4			2.2		mV/*g*

Figure 2.19 Sensitivity Uncertainty of ADXL001

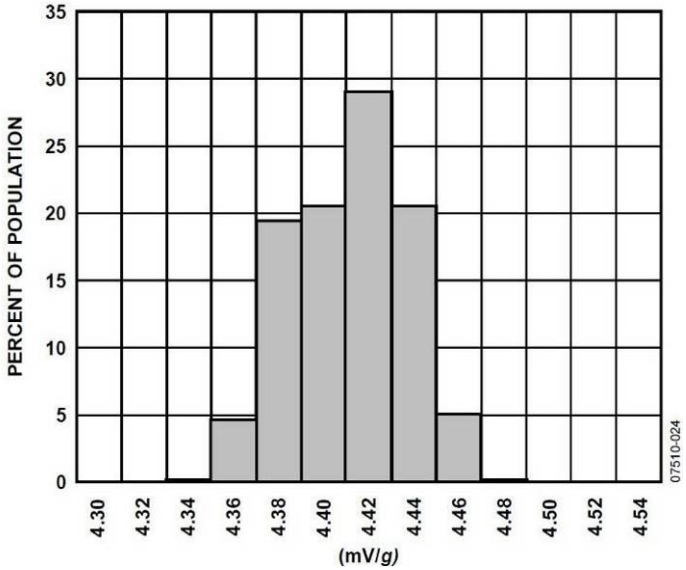

Figure 2.20 Related Histogram shows Sensitivity Distribution of ADXL001 (25°C)

Calculations for Sensitivity Uncertainty

Mean Value of Histogram=

[(3*4.36mV/g)+(18*4.38mV/g)+(21*4.40mV/g)+(28*4.42mV/g)+(21*4.44mV/g)+(4*4.46mV/g)]/95

Mean Value of Histogram= 4.41 mV/g

Standard Deviation= 0.050 mV

(95% CI) = ± 2 σ Standard Deviation

Calculated Uncertainty: (4.45 mV/g - 4.36 mV/g)/4.45 mV/g

Calculated Uncertainty = 1.8 %

According to the final results of the calculation, the mean value of ADXL001-250 Sensitivity Distribution histogram is equal to 4.41 mV/g, and its standard deviation is 0.050 mV ($p<0.05$). Therefore, 95% CI uncertainty due to sensor sensitivity is ± 1.8%.

Low Noise

According to ADXL001 linear accelerometer datasheet, the linear accelerometer provides 3.65mg extra acceleration per square root of system frequency. Hence, in order to clarify how much linear acceleration is contributed by the sensor, the IMG PCB was exposed to several impacts, and then signals coming from sensors were collected with the help of IMG data transmission system. In order to observe frequency components of the signals, sample data were collected. The collected data were first inspected visually and found to have a maximum frequency component approximately up to 400Hz. To confirm this visual inspection, a Fast Fourier Transform (FFT) was applied to each signal in Matlab (**Figure 2.21**).

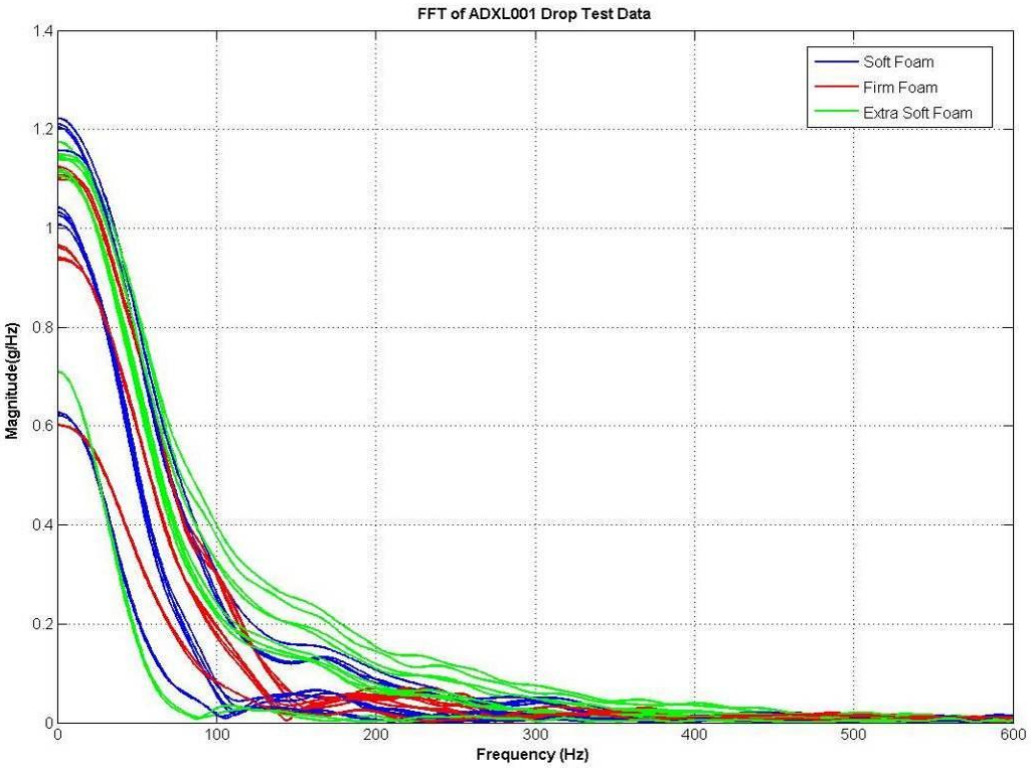

Figure 2.21 FFT of Data Samples of Drop Test Performed with Several Impacted Objects

Calculations for LN Uncertainty

LN= 3.65mg/√Hz (from ADXL001 Datasheet)

LN= 3.65mg /√400 (considered from FFT Plot of Drop Test Data)

LN= 3.65mg /20

LN= 0.1825mg

LN= 0.00018g

The FFT results pointed that any performed impact tests has the majority of signal power at frequencies less than 400Hz. Therefore, in order to calculate

maximum uncertainty provided by sensor low-noise (LN), 400Hz was considered as a conservative estimate. According to the calculation for gathering sensor LN contribution to total sensor uncertainty, it provides 0.00018g uncertainty, which is negligible for the uncertainty analysis.

Cross Axis Sensitivity

The uncertainty due to cross-axis sensitivity is equal to 2.0%, as shown in Figure 2.22

Parameter	Conditions	ADXL001-70 Min	ADXL001-70 Typ	ADXL001-70 Max	ADXL001-250 Min	ADXL001-250 Typ	ADXL001-250 Max	ADXL001-500 Min	ADXL001-500 Typ	ADXL001-500 Max	Unit
SENSOR											
Nonlinearity			0.2	2		0.2	2		0.2	2	%
Cross-Axis Sensitivity	Includes package alignment		2			2			2		%
Resonant Frequency			22			22			22		kHz
Quality Factor			2.5			2.5			2.5		

Figure 2.22 Cross-Axis Sensitivity of ADXL001

For example: two linear accelerometers are located on different sides of a rectangular plate. The plate is then exposed to a bi-axial impact (100g from each side) to observe the effect of cross-axis sensitivity on linear accelerations. According to the numbers in the datasheet, it is expected to read sensor outputs in a range between 98 – 102 g for both axes. In other words, if a multi-axial impact is detected by the IMG PCB, transverse accelerations (y-axis, z-axis) should be taken into account to determine the true longitudinal acceleration measurement (x-axis). However, as mentioned previously, this cross-axis uncertainty will be accounted for after the RSS uncertainty; a combination of bias and random uncertainties, for the primary sensing axis was calculated.

Zero-g Bias

Zero-g-bias is defined as the voltage output when a linear accelerometer is not moving. In order to determine uncertainty due to sensor zero-g-bias, related numbers and a histogram have been examined from the data sheet in the same manner as shown in Figure 2.23.

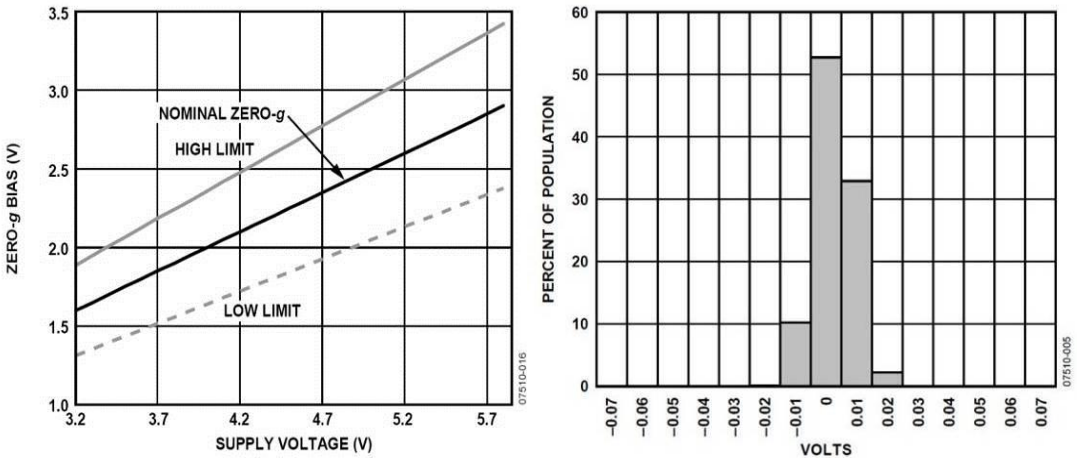

Figure 2.23 Zero-g-Bias Curve (left) and Zero-g-Bias Distribution of ADXL001 (right)

<u>Calculations for Zero-g-Bias</u>

Mean Value of Histogram= [(11%*(-0.01V)) + (53%*0V) + (34%*0.01V) + (2%* 0.02V) / 100%]

Mean Value of Histogram= 0.003 V = 3 mV

Mean Zero-g-Bias = 3mV/4.41mV/g = 0.68g

Standard Deviation= 0.0067V = 6.7mV

Standard Deviation Zero-g-Bias = 6.7mV/4.41mV = 1.5 g

Hence, after zero-g-bias is eliminated, the uncertainty of IMG PCB due to ADXL001 linear accelerometer zero-g-bias distribution is 0.68g, which is relatively small and so ignored.

Frequency Response

The frequency spectrum of the ADXL001 accelerometer has been defined in the Analog Devices datasheet (**Figure 2.24**).

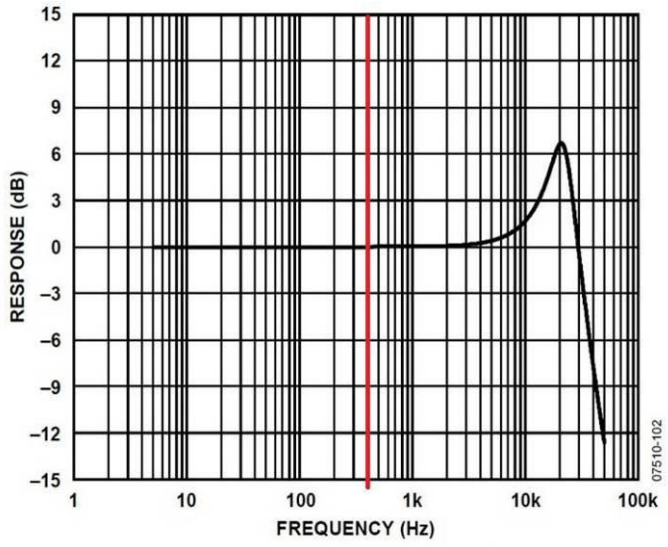

Figure 2.24 Frequency Response of ADXL001 Linear Accelerometer. Red Line indicates where the highest frequency (400HZ) observed in IMG tests.

The frequency response figure shows a linear response up to approximately 2 kHz with negligible change in signal energy[20]. Based on the prior literature search, the IMG characteristic frequencies of interest (25Hz-400Hz) reside in the linear response range of the ADXL001 linear accelerometer. Accordingly, as shown in figure related to FFT of Drop Test, the maximum frequency of the IMG PCB was about 400Hz.

Therefore, uncertainty due to frequency response of ADXL001 is considered negligible.

Sensitivity Due to Temperature Changes

The sensitivity of ADXL001 linear accelerometer is variable over the industrial temperature range (-40°C - 125°C). However, the IMG PCB has been tested at room temperature (25°C) to body temperature (37°C). Although there is no calculated sensitivity value at body temperature, it was previously determined that sensitivity at room temperature was 4.41mV/g. Therefore, to determine the formula for sensitivity as a function of temperature uses this room temperature value and the sensitivity value at 125°C as shown in Figure 2.25.

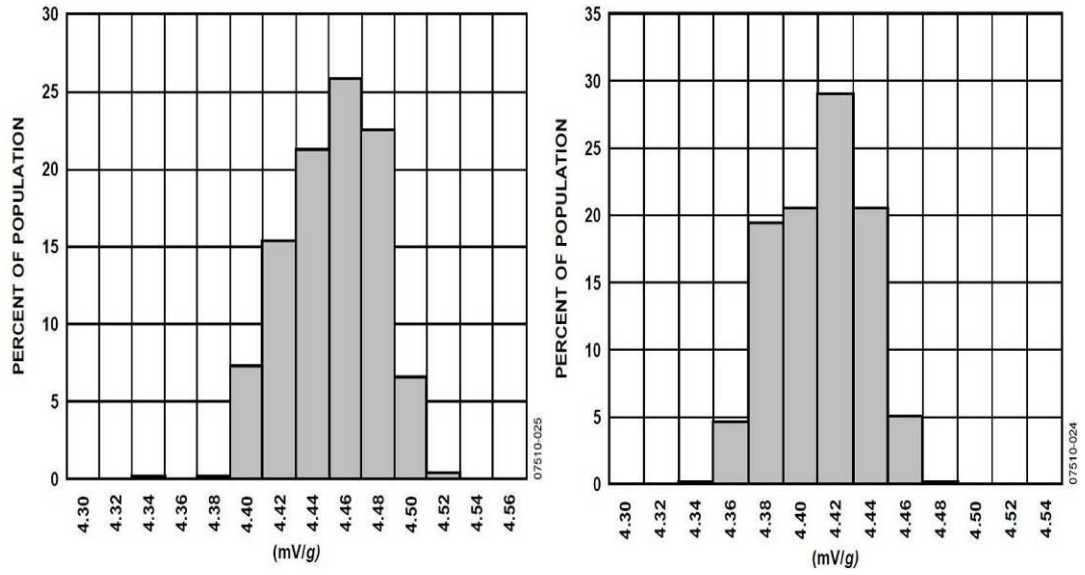

Figure 2.25 Sensitivity Distribution of ADXL001 at 125°C **(a)** and at 25°C **(b),** respectively.

Calculations for Sensitivity at 125°C

Mean Value of Histogram= [(7%*4.40mV/g) + (15%*4.42mV/g) + (22%*4.44mV/g) + (26%*4.46mV/g) + (23%*4.48mV/g) + (7%*4.50mV/g)/100]

Mean Value of Histogram @ 125°C = 4.45 mV/g

Standard Deviation @ 125°C = 0.11 mV

Calculation for Sensitivity at 37°C

Assume that temperature increase is linearly proportional to sensitivity change.

Sensitivity at 25°C = 4.41 mV/g and Sensitivity at 125°C = 4.45 mV/g

Sensitivity change per 1°C = (4.45 mV/g – 4.41 mV/g) / (125°C - 25°C)

= 0.05 mV/g / 100°C = 0.0005 mV/g

Sensitivity at 37°C = 4.41 mV/g + (37°C - 25°C) * 0.0005 mV/g

= 4.42mV/g

Assuming that sensitivity is linearly increasing from 25°C up to 125°C, this sensitivity at 37°C is 4.42mV/g. This equates to small 0.14 g bias for a 100g impact measured at body temperature vs. room temperature. Therefore, changes in sensitivity of ADXL001 linear acceleration sensor due to temperature have been ignored.

Frequency Response Due To Temperature Changes

Like sensitivity, the frequency response of ADXL001 linear accelerometer is responsive to temperature changes. According to the ADXL001 specification sheet, frequency response of the sensor leads to 2.0% uncertainty due to high temperature (Over 120°C). However, this is not a problem for IMG PCB because it was tested at room temperature and the maximum temperature it possibly experiences is the standard human body temperature. Therefore, frequency response uncertainty due to high temperature was ignored for IMG PCB uncertainty calculations.

Figure 2.26 Nominal Frequency Response Values of ADXL001 Linear Accelerometer

Results

According to theoretical uncertainty analysis, ADXL001 linear accelerometer has 1.8% bias uncertainty and 2.0% random uncertainty, as shown in the table below:

Uncertainty Analysis for Linear Accelerometer			
Uncertainties	**Type**	**ADXL001(2σ)**	**Notes**
Non-Linearity	R	2.0%	Given in ADXL Datasheet
Low Noise	R	0.00018g	Calculated from ADXL Datasheet (Negligible)
Cross-Axis Effect	R	2.0%	Given in ADXL Datasheet
Human Error	R	N/A	Assumed Negligible
Sensitivity	B	1.8%	Given in ADXL Histogram
Zero-g-Bias	B	0.52%	Removed by in-circuit filter
Frequency Response (0-120°C)	B	2%	Negligible
Sensitivity Due to Temperature Change	B	0.14%	Negligible

Table 2.3 Uncertainty Values of ADXL001 Linear Accelerometer Utilized in IMG Drop Test

In order to combine dominant bias and random uncertainties, determined uncertainty values were inserted into related equation to calculate total system uncertainty due to ADXL001 linear accelerometer shown below:

$U_B = (1.8)^2$ and $U_R = (2.0)^2$, So

$U_{t1} = 1.8\% + 2.0\%$

$U_{t1} = 3.8\%$ => 99.7% Coverage (Worst Case)

$U_{t2} = 2.0\%$ => 95% CI

At the end of whole process, 3.8% total system uncertainty due to ADXL001 linear accelerometer uncertainty has been calculated as the worst case. When the uncertainty due to cross-axis sensitivity has been directly added to final result, the total system uncertainty is equal to **3.8% ± 2.0% of cross-axis sensitivity**.

L3G4200D Gyroscope Theoretical Uncertainty Analysis

Methodology

According to the datasheet provided by ST Microelectronic (**Doc ID: 17116 Rev 3**), the uncertainty of L3G4200D angular rate sensor has been determined. As mentioned previously, L3G4200D is a triaxial sensor, which means it is able to measure angular rotation along X, Y and Z axes. Moreover, instead of axes names, technical terms are generally used to prevent misunderstanding about axes directions. Therefore, spinning around Z-axis is called yaw (Y), around Y-axis is pitch (P) and around X-axis is roll (R) (**Figure 2.27**).

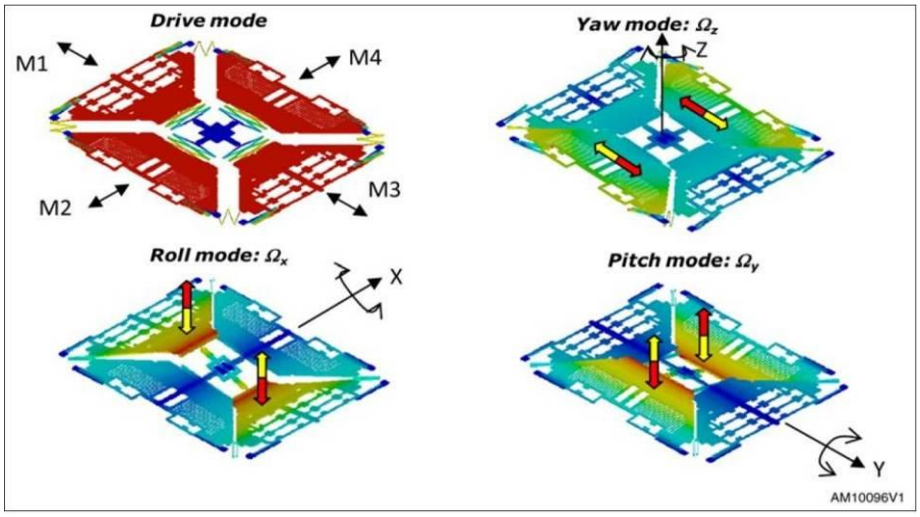

Figure 2.27 Technical Terms of Spinning Axes

The list of uncertainties for the L3G4200D is shown below:

Non-linearity

Sensor uncertainty due to non-linearity as mentioned in ST Micro (**Doc ID: 022032 Rev 1, Page 13**), contains a table that includes non-linearity uncertainty with corresponding full scale (FS), which is equal to 34.9 rad/s. According to this table, L3G4200D sensor uncertainty due to non-linearity is 0.3% of FS.

	NLP	NLR	NLY
FS	[%FS]	[%FS]	[%FS]
250	0.11	0.09	0.10
500	0.15	0.16	0.14
2000	0.28	0.30	0.32

Figure 2.28 Non-Linearity (NL) Percentages of L3G4200D for All Three Axes in Different FS Numbers

Sensitivity

The sensitivity of L3G4200D is equal to 70mdps/digit (milli degree per second per digit). For calculating uncertainty due to the sensor sensitivity, the related histogram has been utilized, which is shown in ST Micro extended datasheet (**Doc ID: 022032 Rev 1, Page 22)**. Calculations for the sensor sensitivity were completed for

each axis. Mean uncertainty due to sensitivity variation was considered on Yaw axis, which is about 0.4%. Maximum uncertainty due to sensitivity variation for each axis is almost 3.0%. In order to make a better prediction for IMG PCB measurements, uncertainty due to sensitivity variation was considered by 3.0% of FS.

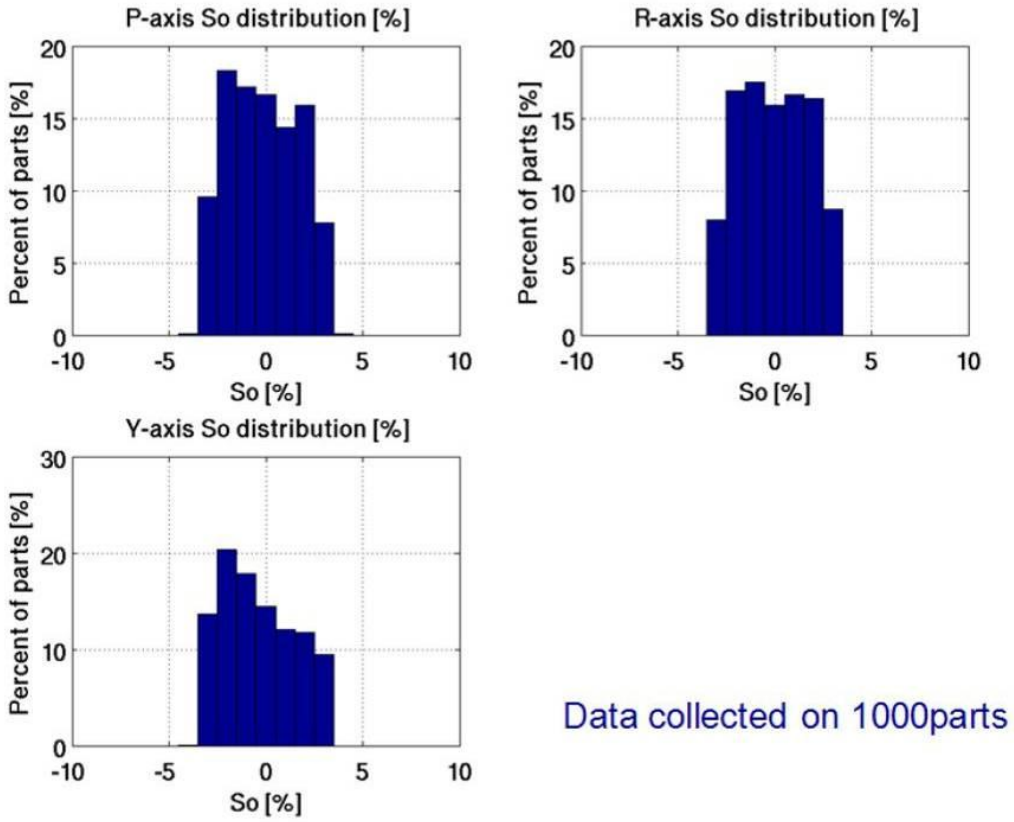

Figure 2.29 Sensitivity Distribution of L3G4200D for All Three Axes

Calculations for Sensitivity Uncertainty

Calculations for Pitch

Sensitivity Offset Pitch = [(-0.03x9) + (-0.02x18) + (-0.01x17) + (0x17) + (0.01x14) + (0.02x16) + (0.03x9)] / 100

= (-0.27 -0.36 -0.17 + 0 + 0.14 + 0.32 + 0.27) / 100

Sensitivity Offset Pitch = -0.07 %

Yaw and Roll offsets were calculated with the same method above:

Sensitivity Offset Roll = -0.03 %

Sensitivity Offset Yaw = -0.37 %

Low Noise

According to the L3G4200D extended datasheet (**Doc ID: 022032 Rev 1, Page 27**), the angular rate sensor provides approximately 0.03 degree over square root of maximum frequency of the system to the total rotation measurement (**Figure 2.30**).

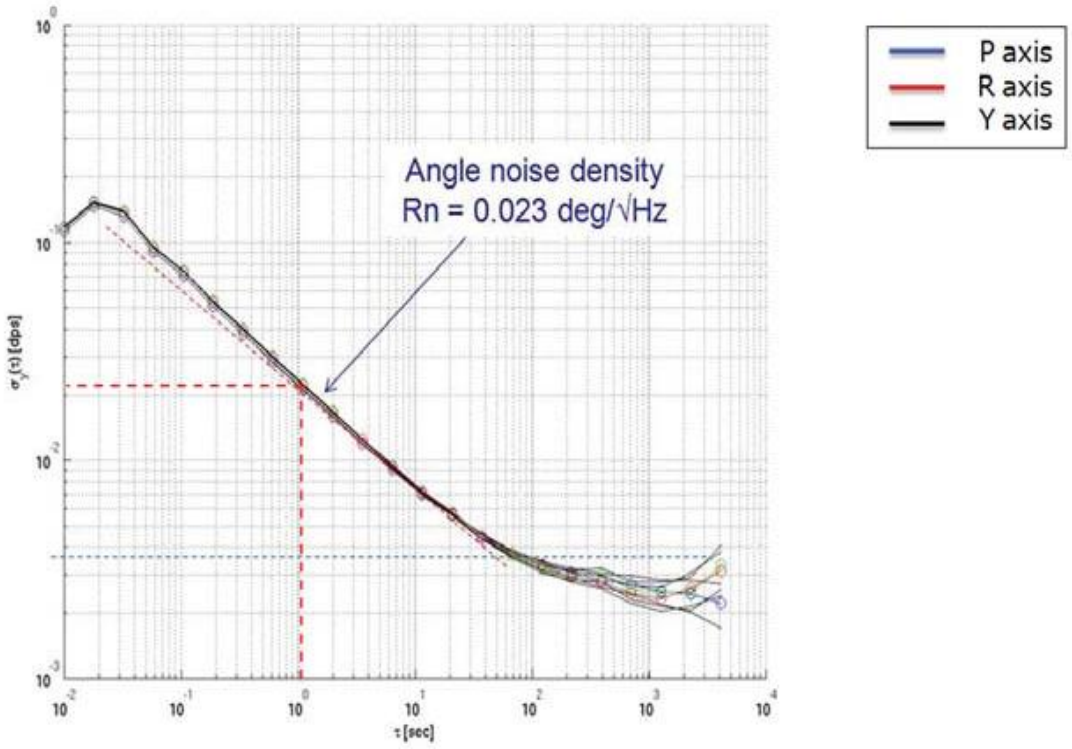

Figure 2.30 Comparison between L3G4200D and Another Gyroscope in terms of Low-Noise Characteristics

As mentioned in Figure 2.30, the maximum low noise value of L3G4200D gyroscope for any frequencies is less than 0.09 rad/s, which is also equal to 0.15mrad/s.

Calculations for LN Uncertainty

LN = 0.09dps/√Hz (Max LN Value from L3G4200D Extended Datasheet)

LN = 0.09dps/√110Hz (L3G4200D Cut-off Frequency)

LN = 8.6mdps

LN = 0.15mrad/s

According to the calculation for gathering sensor LN contribution to total sensor uncertainty, it provides 0.15mrad/s uncertainty, which is negligible for the system.

Zero-g-Bias

According to L3G4200D datasheet (**Doc ID: 17116 Rev 3**), digital zero-g-bias level of the sensor is 75mdps, which corresponds to 1.2 rad/s (3% of FS). However, this bias was successfully removed by internal IMG firmware.

Sensitivity Due to Temperature Changes

According to L3G4200D datasheet (**Doc ID: 17116 Rev 3**), the sensitivity of L3G4200D sensor is responsive to temperature changes. Moreover, there is another graph in the extended datasheet that exhibits variability of L3G4200D for all three axes under different temperature values. Results show that sensitivity of the sensor is not affected if it is working at body temperature.

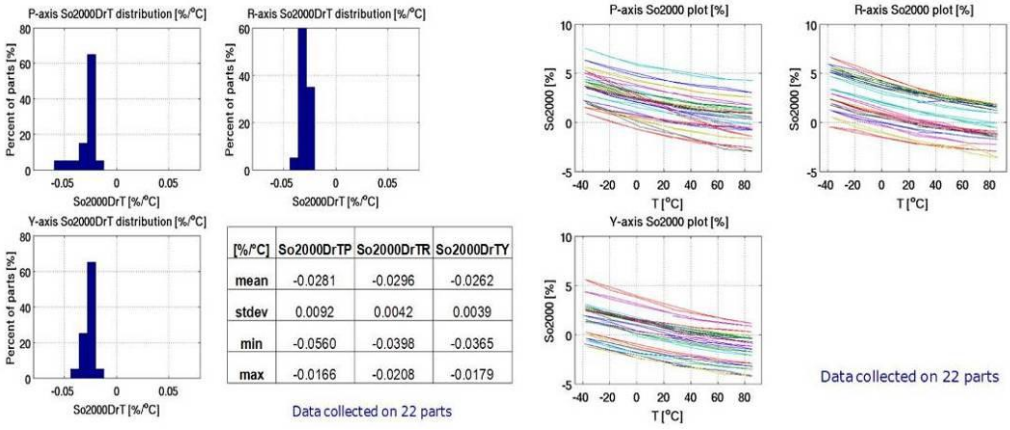

[%/°C]	So2000DrTP	So2000DrTR	So2000DrTY
mean	-0.0281	-0.0296	-0.0262
stdev	0.0092	0.0042	0.0039
min	-0.0560	-0.0398	-0.0365
max	-0.0166	-0.0208	-0.0179

Figure 2.31 Histograms Show the Effect of Temperature Changes **(left)** and Sensitivity Variability of L3G4200D **(right)**

Results

At the end, the uncertainty factors related to L3G4200D angular rate sensor are determined as shown below:

Uncertainty Analysis of Angular Rate Sensors			
	Type	**L3G4200D (2σ)**	**Notes**
Non-Linearity	R	0.3%	Given by Technical Article
Low Noise	R	0.15mrad/s	Negligible
Sensitivity	B	3%	Given by Technical Article
Zero-g-Bias	B	3%	Removed by IMG Firmware

Table 2.4 Uncertainty Values of IMG L3G4200D Gyroscope

After determining uncertainty contributions for each possible source, the uncertainty values are inserted into related equations to calculate total system uncertainty due to the L3G4200D angular rate sensor, as shown below:

$U_B = [(3.0)^2]^{1/2}$

$U_R = [(0.3)^2]^{1/2}$

$U_{t1} = 3.0\% + 0.3\%$

$U_{t1} = 3.3\%$ => 99.7% Coverage (Worst Case)

$U_{t2} = 0.3\%$ => 95% CI

At the end of whole process, 3.3% total system uncertainty due to L3G4200D angular rate sensor uncertainty has been calculated as the worst case. Detailed information is provided in related Appendix Section (See Appendix B).

Theoretical Uncertainty Analysis of Other Electrical Components On IMG PCB

In order to determine the reliability of an electrical printed circuit board (PCB), the main components should be taken into account, as well as extra elements needed for mounted sensors to work properly. The IMG PCB components will be taken into account for calculating total system uncertainties.

RC Filter

In the IMG PCB, a simple RC circuit has been utilized to design an in-circuit filter, which eliminates frequencies exceeding 1769Hz. It simply consisted of a 900 ohm resistor and a 0.1 μF capacitor. However, in accordance with SAE J211 standards, the raw test signal should be exposed to a fourth order low-pass filter, whose -3dB cut-off frequency is 1650Hz. Even though there was a difference between calculated and applied cut-off frequencies, it was unlikely that the difference affected the results because the difference was out of the frequencies of interest for impacts generated for this study.

A/D Converter

As mentioned previously, another component of IMG PCB is the onboard microcontroller (dsPIC33FJ128GP804, Microchip Technology Inc., Arizona USA), which comprises a powerful central processing unit (CPU) and peripherals for serial communication, analog to digital (A/D) conversion, direct memory access (DMA), timers, interrupt controller and digital input/output (I/O). It was determined that one

source for the system uncertainty might be the microcontroller A/D converter resolution. Resolution means the smallest change microcontroller is capable to sense in the quantity that it measures. For instance: a bit change in the microcontroller corresponds to 0.8mV change for the system output. In order to calculate the A/D resolution, PCB operating voltage and the number of bits should be considered because these numbers directly affect the resolution of the A/D converter. The result of calculations shows that regardless of peak value of any tests, the range of uncertainty due to the microcontroller resolution is ±0.18g.

Calculations of Microcontroller Resolution

Resolution=Operating Voltage/ (2^# of bits)

Resolution= $3.3mV/\left(2^{12}\right)$ bits

Resolution=0.8mV per bit

Resolution= $0.8mV/(4.41mV/g)$ (Assumed Sensor Sensitivity=4.41mV/g)

Resolution=0.18g

Results

As the result of IMG PCB uncertainty analysis, factors due to uncertainty were determined and according to datasheets and other documents related to the system components, the effect of each component was scrutinized and then combined with the contribution of RSS method.

Component	Uncertainty (2σ)	Notes
ADXL001-250g linear accelerometer	3.8%	Also include 2.0% cross axis sensitivity post-hoc
L3G4200D - 34.9rad/s angular rate sensor	3.3%	Effects of 110Hz low-pass filtering and 800Hz sampling rate yet to be quantified
dsPIC33F Microcontroller	0.18g	Equal to on-board A/D converter resolution

Table 2.5 Main Components of IMG PCB and Individual Uncertainty Contributions to the System

CONCLUSION OF IMG THEORETICAL UNCERTAINTY ANALYSIS

According to calculations related to the theoretical uncertainty analysis of each IMG component, 3.8% + 2.0% of cross-axis sensitivity uncertainty due to ADXL001 linear accelerometer, 3.3% uncertainty due to L3G4200D angular rate gyroscope, and 0.18g uncertainty due to the microcontroller resolution have been calculated.

In light of the theoretical uncertainty analysis, a realistic estimation that for a 140g resultant translational impact (100g impact coming through x-axis and another 100g impact coming through y-axis), the uncertainty of the IMG measured linear acceleration would be approximately ±5.8g, or ±1.8% of peak amplitude. This is a promising finding as measurement accuracy within ±5% of peak amplitude during dynamic events is the engineering benchmark for IMG. Even though there are different bias values seen in theoretical and experimental uncertainty analysis, about 1%, using a more stable test setup may decrease that difference.

In terms of angular velocity, according to the theoretical uncertainty analysis, the total IMG angular rate sensor uncertainty is about 3.3%, which corresponds to about ±1rad/s change in 34rad/s. According to related experimental uncertainty analysis, L3G4200D angular rate sensor has 0.3% bias and 1.7% random uncertainty. Even though there are different random values seen in theoretical and experimental uncertainty analysis, using a more stable turntable may decrease that difference.

CHAPTER III

IMG SENSOR TESTING

ADXL001 Linear Accelerometer Testing

Materials & Methods

Expected Results

The next step was to expose the IMG PCB to sudden impacts for evaluating its functionality. Before the start of impact tests, it was necessary to do some research about possible outputs because in order to determine whether collected data are satisfied or not, the expected results should be analyzed first and then test data can be compared to results in literature. Moreover, expected results also help to make a clear interpretation about collected data. According to related literature search, in order to determine possible effects of an head impact or a head concussion, impact durations are as important as impact peak g values[21,22,23,24]. According to literature search based on head impact studies, a head impact sensitive system should be capable to detect impacts peak values between approximately 20 and 250g and duration between 5 and 25ms[25,26,27].

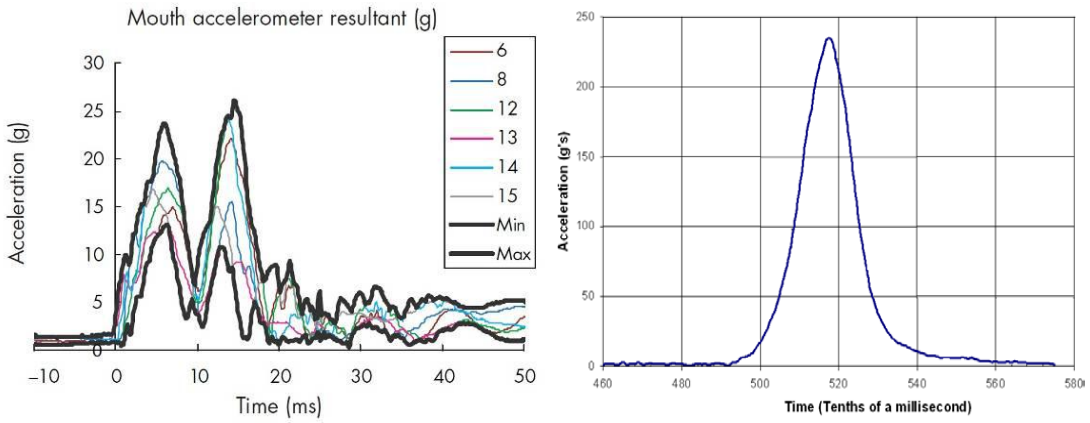

Figure 3.32 Literature Test Results showing Low Amplitude and Long Duration[28] **(left)** versus High Amplitude and Short Duration Impacts[29] **(right)**

Data Acquisition (DAQ) System of Reference Measurement

In order to observe signals coming from reference sensors, a data acquisition (DAQ) system was installed. The DAQ system has two main parts: software and hardware.

In terms of hardware, reference Model 64B linear accelerometers were connected into a DAQ Interface Panel, which was custom made by Cleveland Clinic Electronics and Bio-Robotics Cores. The DAQ Panel was connected to a DAQ Chassis, called NI SCXI-1314, which is capable to transmit data coming from reference sensors to PC without time delay among channels in the DAQ Interface Panel. NI PXI-1042, produced by National Instruments, was utilized to synchronize collected signals and deliver them to PC of the DAQ system (**Figure 3.33**).

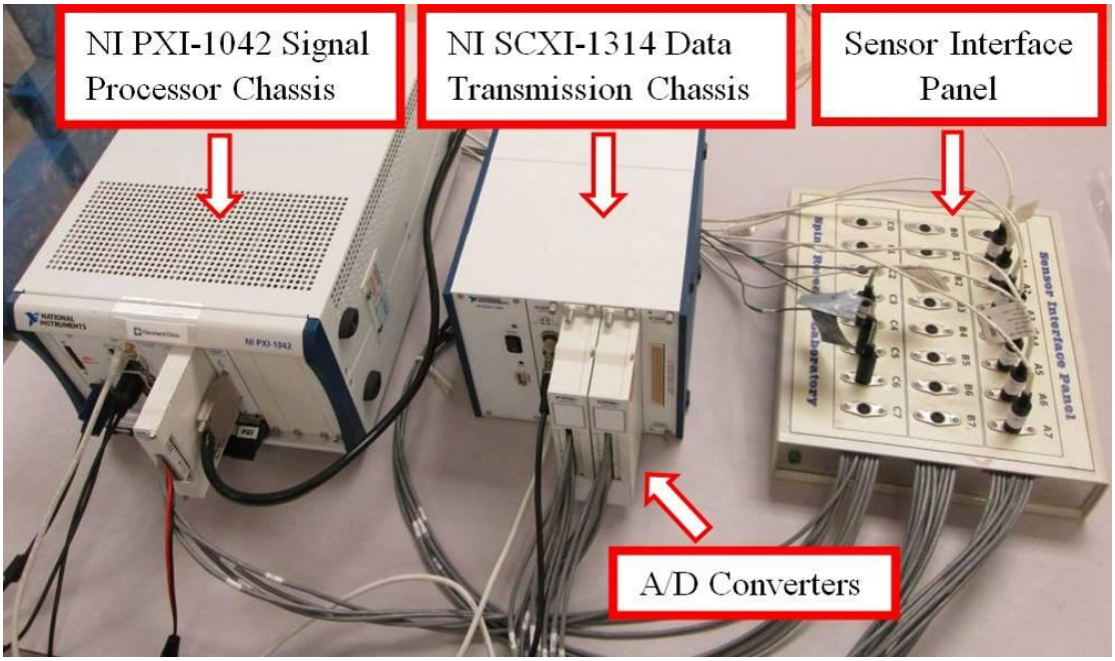

Figure 3.33 DAQ System Hardware Elements and Connections

In terms of software, Labview (National Instruments, Austin, Texas) based software was developed to monitor signals coming from the DAQ hardware. It also provides diversity to the user in terms of sensor calibration, data collection time and real-time data display (**Figure 3.34**)

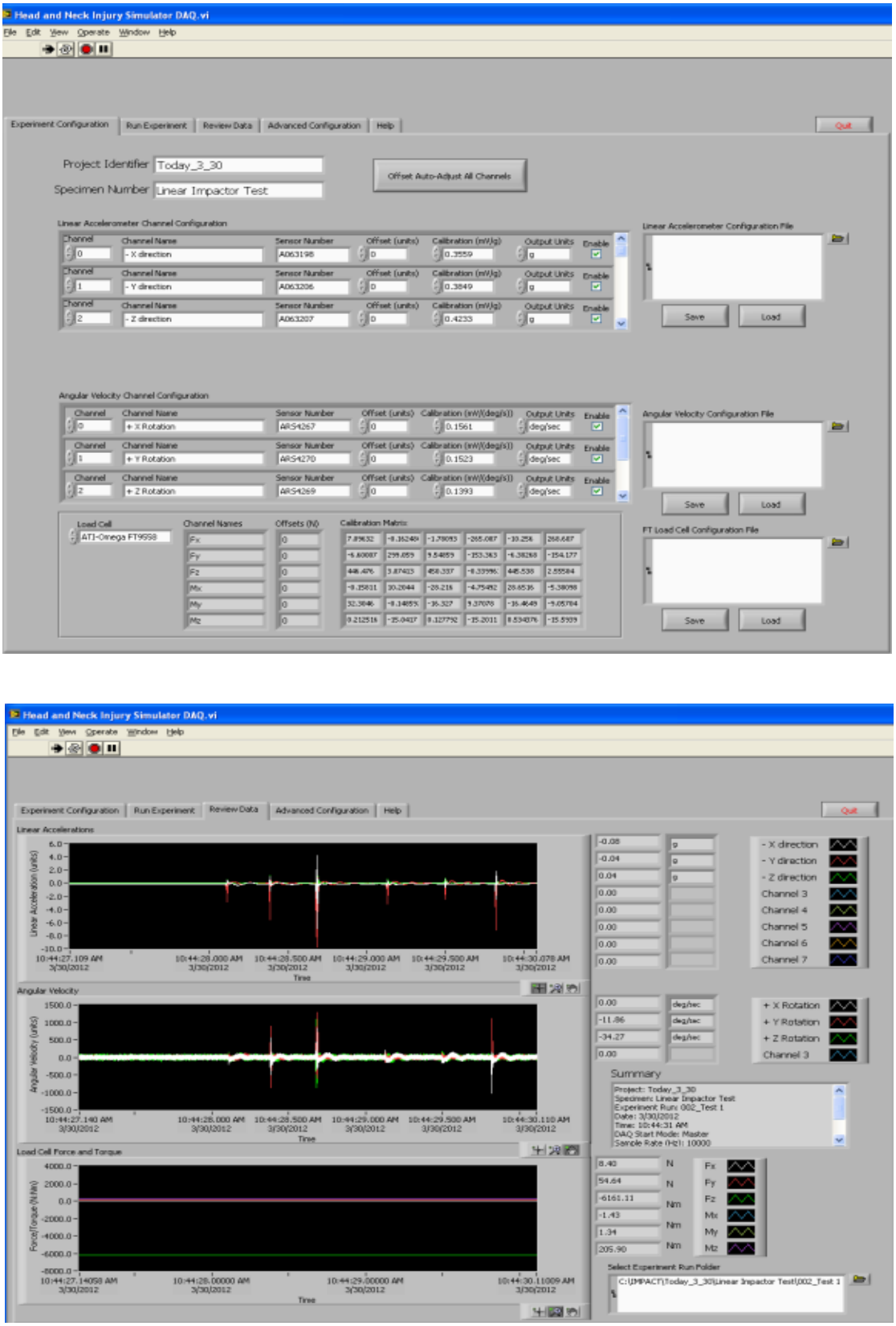

Figure 3.34 Equipment Configuration (**top**) and Review Data Sections (**bottom**) of Labview DAQ System Interface

Additionally, before the start of testing, Model 64B sensor calibration values were entered into the DAQ system because each reference sensor has its own calibration value. The numbers on the calibration sheet were used to calibrate reference sensors.

Mechanical Setup

The purpose of the IMG PCB dynamic uniaxial testing was to test three uniaxial ADXL001-250g linear accelerometers, located on different sides of the PCB, and one tri-axial L3G4200D angular rate sensor, located the center of the PCB. In order to validate the IMG sensors functionality, signals collected by the sensors on the IMG PCB were compared to signals collected by reference sensors (Measurement Specialties 64B linear accelerometers, Hampton, VA) affixed to the calibration fixture (**Figure 3.35**). The calibration fixture consisted of a base, a back frame and a vertical aluminum rails with a sliding plate. The Base was mounted on a balanced pneumatic table to minimize possible vibrations due to an impact.

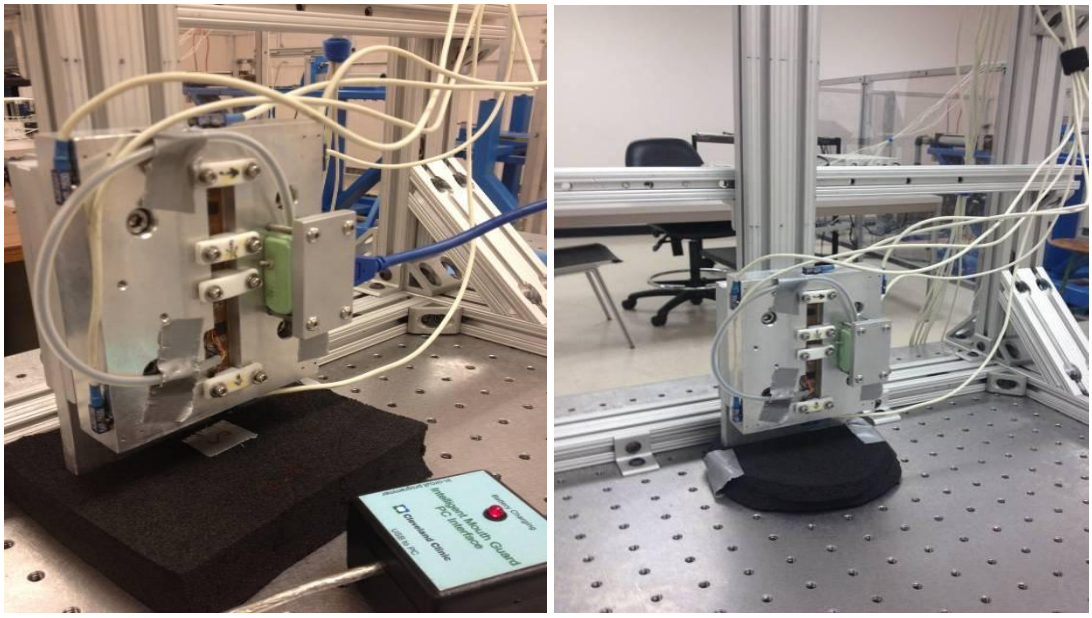

Figure 3.35 A Close View of the Free Fall Test Setup **(left)** and Sliding Aluminum Plate with Metal Plate **(right)**.

The aim of the setup was to quantify the IMG ADXL001 linear accelerometer dynamic outputs compared to 64B reference linear accelerometers. The validation procedure was as follows:

A machined aluminum mounting plate was attached to a sliding carriage. The sliding carriage had polyethylene bearing pads and was free to move in the vertical direction as the carriage was dropped. Therefore, the mass of plate became an important parameter of the test because the sliding plate was only energized with gravitational force. As long as the mass of plate was increased, its total potential energy was increased and impacts with higher energy at the same releasing point were observed. Moreover, care was taken to measure transverse accelerations to quantify potential cross axis accelerometer measurement influences. This custom metal machining utilized in this part of the validation tests is shown in Figure 3.35. The battery pod and download connection tether was held in place by a metal clamp. A

total of six (6) linear accelerometers were attached around the custom metal plate with screws. As mounted in Figure 3.35, the IMG PCB tested two of the three ADXL001 linear accelerometers. In this longitudinal configuration, two of the linear accelerometers were used in a redundant fashion to detect translational motions in the longitudinal, or drop, direction. The other four linear accelerometers were used in a redundant fashion to measure transverse accelerations and quantify rotational acceleration should sufficient rotations be experienced. When the carriage was rotated 90° to test the third IMG linear accelerometer in the transverse direction, the reference scheme was flipped with four redundant linear accelerometers in the longitudinal direction and two redundant linear accelerometers in the transverse direction. Four (4) plastic pieces were used to hold the IMG PCB stationary, with each piece centered over a sensor (three accelerometers, one gyroscope). The blue USB cable was used to charge the IMG battery and also used to download data after an impact occurred.

As seen in Figure 3.36, firm, soft and extra-soft pieces of foam were utilized for designing a known impact surface. Mechanical properties of foams with serial part numbers are mentioned in the related table.

Mechanical Properties / **Foam Types**	**Durometer (OO)**	**Firmness (psi)**	**Density (lbs/cu.ft)**
Extra Soft (85175K27)	40	2-5	4-6
Soft (85175K57)	60	5-9	5.5-7.5
Firm (85175K87)	65	9-13	7-9

Table 3.6 Mechanical Properties of Foams Utilized in IMG Drop Tests (MCMASTER-CARR PART NUMBERS)

In order to adjust impact peak values and duration, different types of foam and drop heights were used. As mentioned previously, impact peak and duration values were extremely important for the IMG validation. In order to observe the effects of impact surface on test results, three types of foam, which have different stiffness, were utilized (**Figure 3.36**).

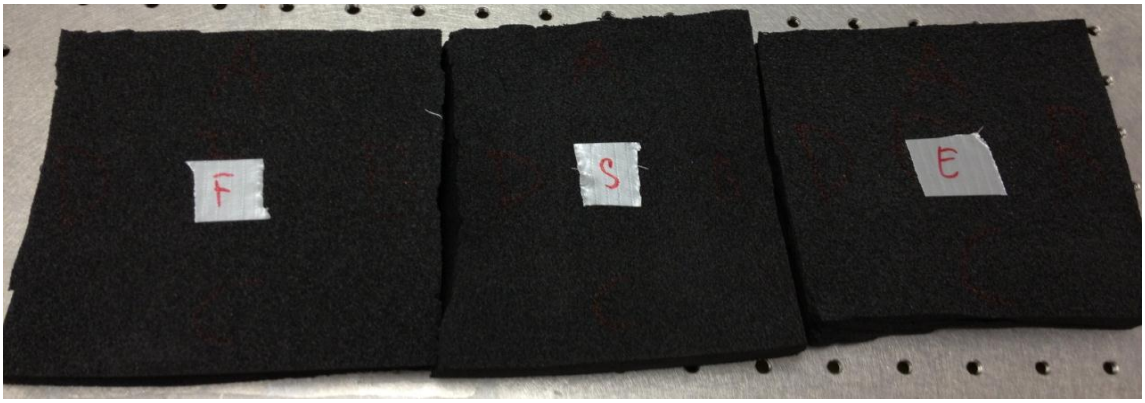

Figure 3.36 Firm (F), Soft (S) and Extra Soft (E) Foam Used In Linear Accelerometer Drop Tests

Additionally, another type of pad, manufactured by Airex Inc., (Brampton, ON, Canada) was used to observe desired impact peak values with desired time duration and a bell-shaped signal. The Airex pad was horizontally cut into three pieces to obtain three different thicknesses, each with a different stiffness. The thickness of the original pad was about 3-cm and the cut pieces of the pad were half, one third and one fourth thickness of the balanced pad, respectively (**Figure 3.37**).

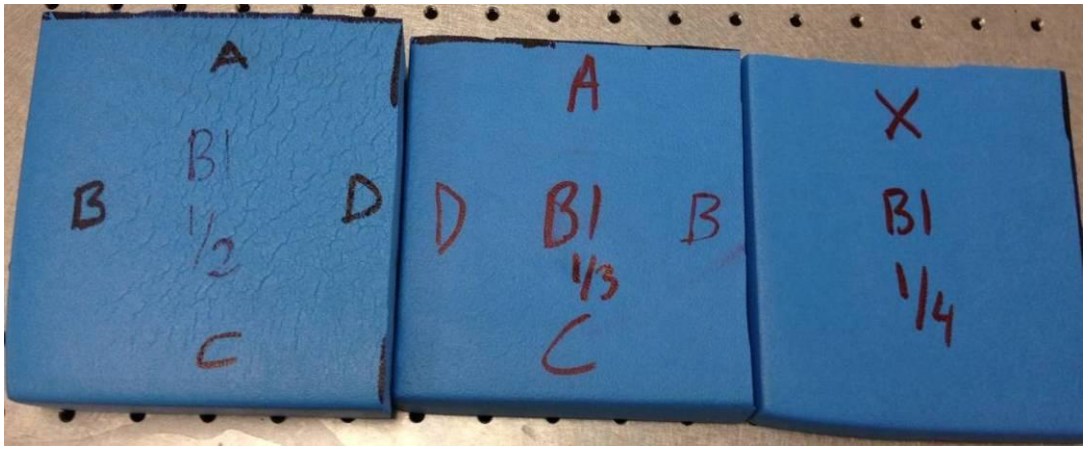

Figure 3.37 Three Slices of Balanced Pad: Half **(left)**, One Third **(center)**, and One Fourth Thickness **(right)**

IMG Firmware Calibrations

User selectable IMG PCB options were adjusted for the linear impact tests to gather the most accurate acceleration results. Sampling rate of the IMG was modified to 4000Hz to minimize the risk of data loss because duration of linear impacts was considered about 5-25ms from the literature search. Event collection duration was set to 125ms for capturing the region of interest of collected data. Pre-triggering time was set to 50ms for considering zero-g-offset values for each impact. This means that when IMG PCB detects an impact, it collects several data points that include useful information from 50 ms before up to 75ms after the impact. Another modification about IMG PCB was related to its storage fashion. Since the IMG detects consecutive impacts, it can keep saving the collected data until either IMG is turned off or its memory gets full (approximately 250 impacts). In order to delete the stored data for more storage space, IMG was turned off and on before using it for a new test. After the off and on process, IMG overwrites detected signals as new data in the EEPROM.

Linear Accelerometer Drop Test Data Analysis

Data Analysis was an important part in validation process of IMG. According to the Society of Automotive Engineers (SAE) standards, head impact signals must be filtered with dedicated Class Frequency Channel (CFC) Filter[30]. The CFC Filter is a fourth order low-pass Butterworth filter. The Butterworth filter is a finite impulse response (FIR) filter that provides a flat frequency response in its passband region. It also has a linear phase response. Each CFC filter was classified with its corner frequency. For example, the corner frequency of CFC1000 is equal to 1000Hz. The -3dB cut-off frequency is approximately equal to CFC x 5/3. The common types of CFC Filter are shown below:

- CFC1000, cut-off frequency 1650 Hz
- CFC600, cut-off frequency 1000 Hz
- CFC180, cut-off frequency 300 Hz
- CFC60, cut-off frequency 100 Hz

Instead of applying a fourth order Butterworth filter once, SAE recommends to design a second order Butterworth filter and apply it to an impact signal once and reverse the filter and apply it again because this method prevents both time and frequency shift in the signal due to filtering. As a result, the product of this process is a fourth order Butterworth filtered version of the initial signal with no phase shift. Accordingly, Matlab code developers created a function called “filtfilt” that works

exactly similar to the SAE J211 Filter. Therefore, the “filtfilt” function was used in this project.

For accelerations measured on the head, CFC1000 is recommended with a -3dB cut-off frequency in 1650 Hz filtering for linear impacts. However, once FFT of a test data was analyzed, it was realized that maximum frequency components of test signals were no greater than 400Hz. Because of this, there may be a custom method to filter each signal, instead of just applying CFC1000 because it was clear that CFC1000 does not have the optimum corner frequency to filter noise in gathered signals collected for this project. In order to fix this problem, imitating real test signals with a proper way should be determined and corner frequency of appropriate CFC filter is then considered at the end of this process. This custom filtering method could be a study in future works.

Results

A total of 223 impact tests were completed with four different types of foams. Different types of foams were utilized to observe a test result that looks similar to a real data in terms of peak values, impact duration and signal shape. In order to minimize any errors due to sensor malfunctions, tests were performed with the contribution of two IMG and two reference sensors that all measure impacts on the same orientation. As expected, tests performed with different types of foams presented different peak values, impact durations and signal shapes (**Figure 3.38**).

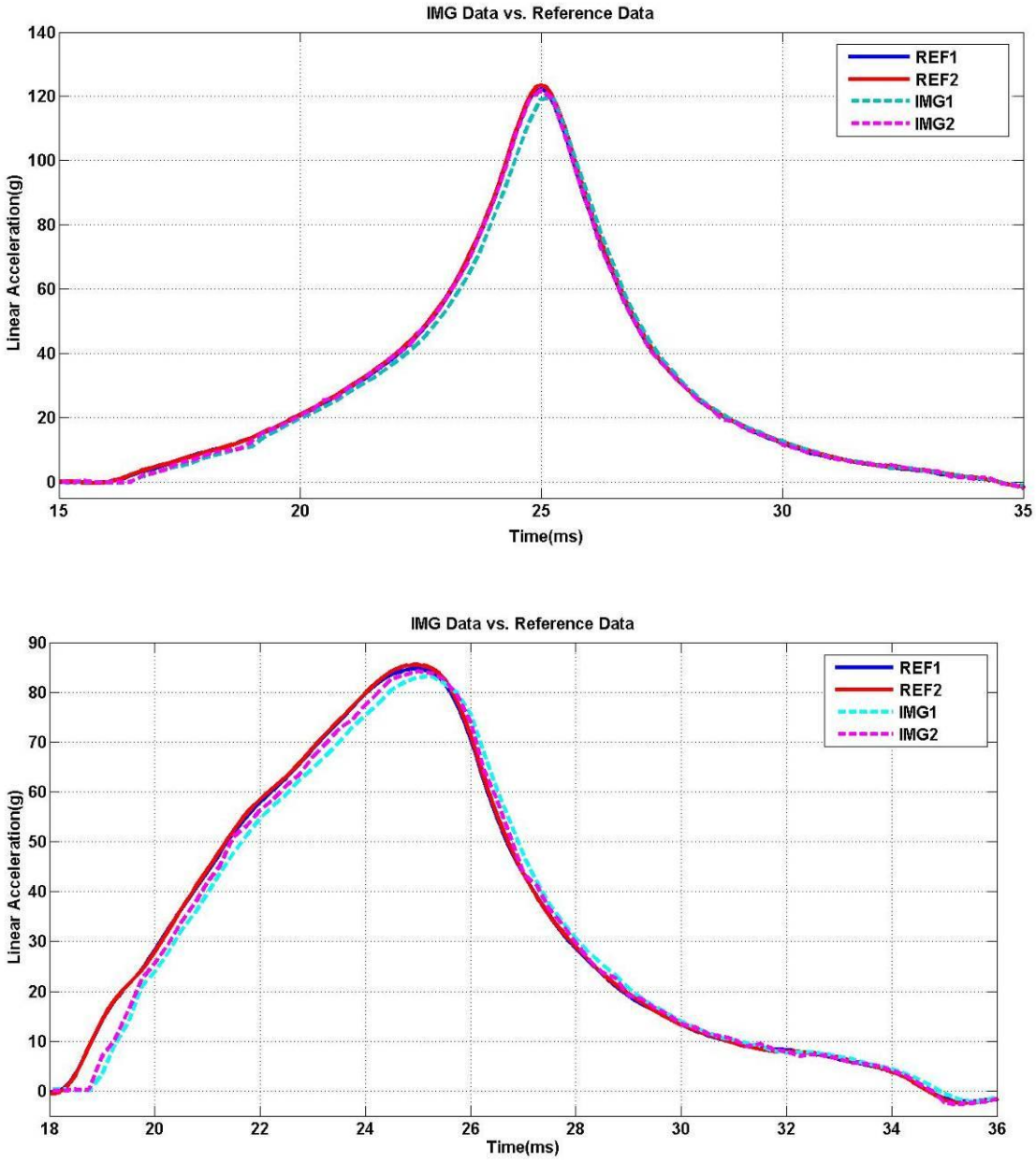

Figure 3.38 Extra Soft Foam, Drop Height=25 inches **(top)**, and Firm Foam, Drop Height=32 inches **(bottom)**

In order to further examine performance, the Airex balance pad and soft foam were also used in drop tests. As expected, they exhibited different responses versus harder foam impacts (**Figure 3.39**).

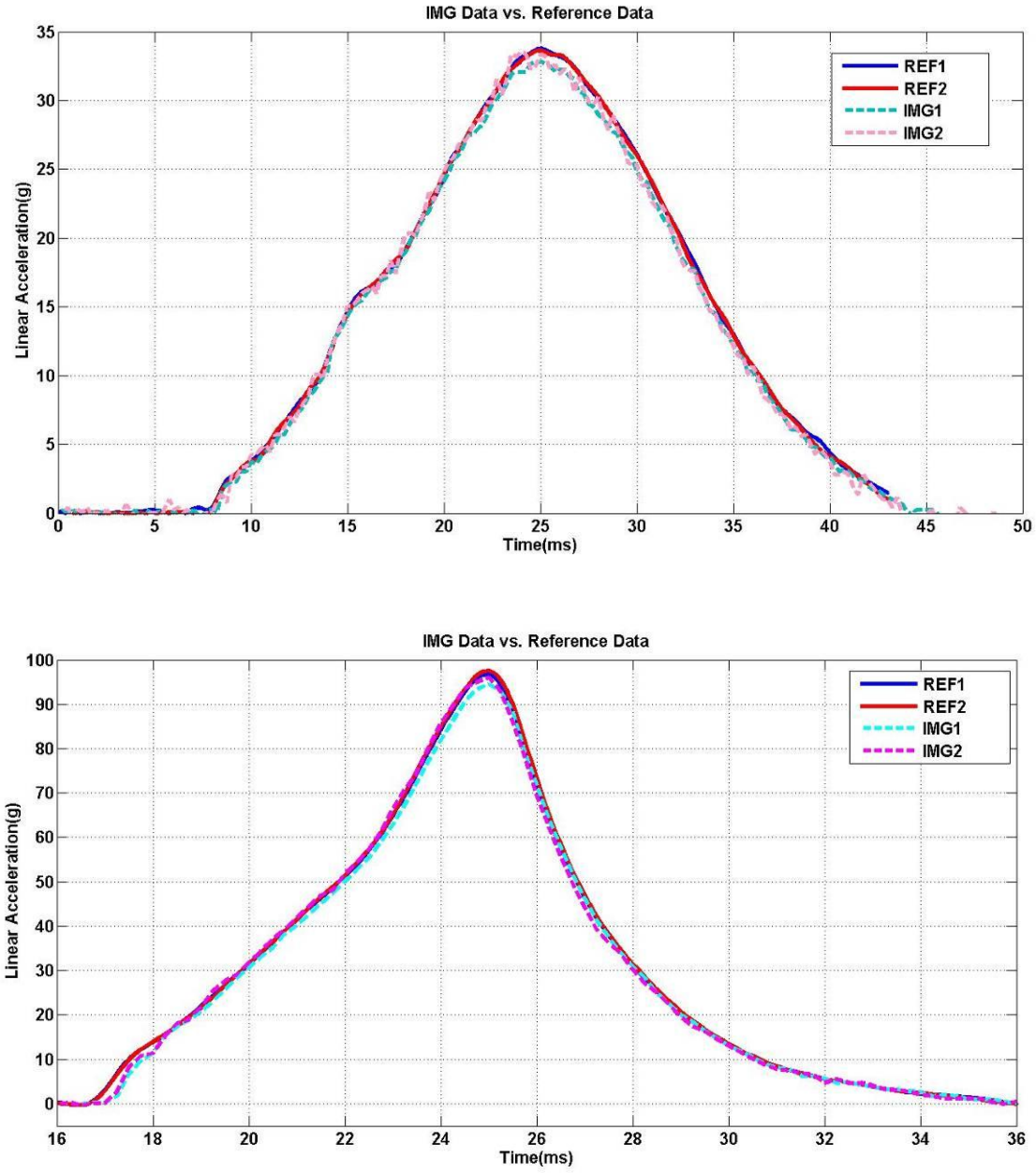

Figure 3.39 Airex Balanced Pad, Drop Height=23.4 inches (left), and Soft Foam, Drop Height= 32 inches (right)

In order to prove repeatability of the test setup, the same foam types were exposed to the same impact level provided by a sliding plate released from the same height. Six tests were performed under the same condition and collected data of each test were plotted in one graph to compare them in terms of peak values and impact

duration. Additionally, in order to determine mean values and standard deviation of the test results, mean values of linear acceleration of data sets were inserted into the graph. This method was firstly applied for IMG data provided by a sliding plate released from 8 inches, and then repeated for 12 inches (**Figure 3.40**).

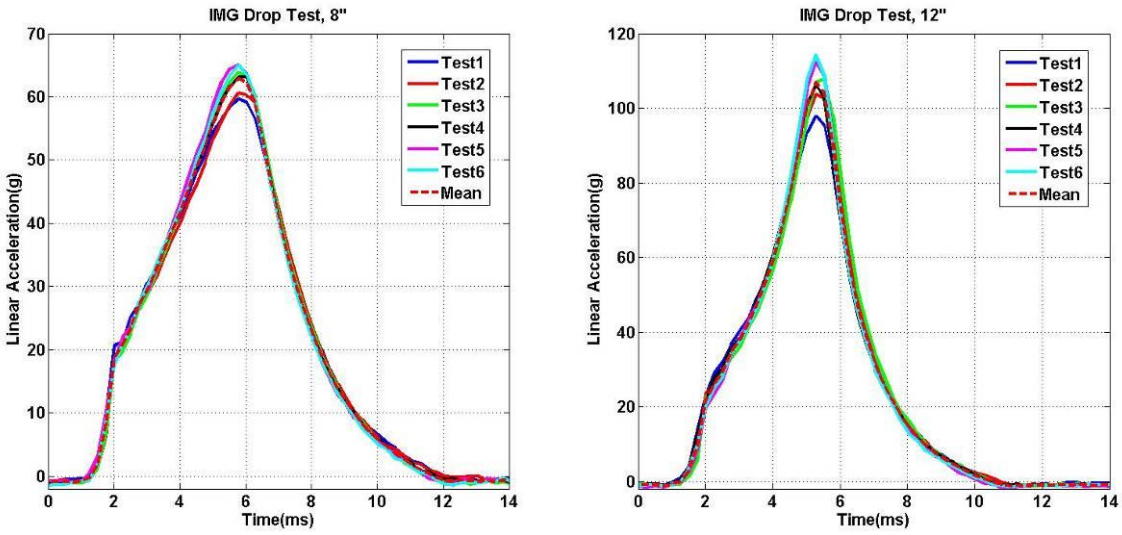

Figure 3.40 Drop Test Impact Data provided by A Sliding Plate Released from 8" **(left)** and 12" **(right)**.

In order to consider characteristic frequencies of the collected signals, an FFT was applied to determine frequency components of IMG data (**Figure 3.41**).

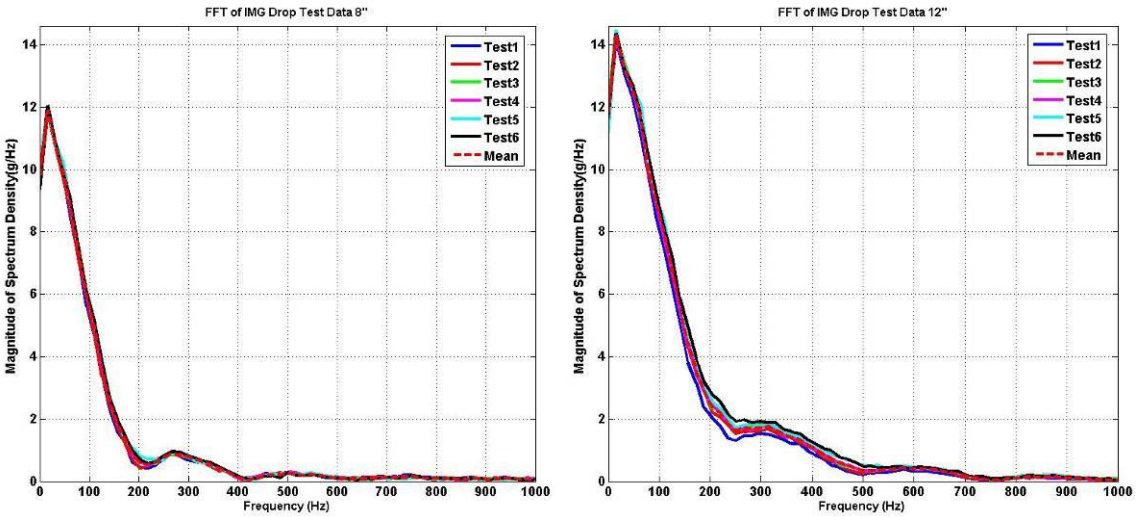

Figure 3.41 FFT of IMG Data Results and Mean Values

As seen in Figure 3.41, FFT responses of six consecutive test results are almost identical. Briefly, this means that the test setup is repeatable to use and the system components give the same responses under the same conditions.

As mentioned previously, the ultimate goal of ADXL001 testing was to determine how much difference between Reference and IMG sensors measurement in impact peak values, in unit of g (1g = 9.81m/s^2). Figure 3.42 displays peak values of 223 drop tests performed with four different types of foam. Moreover, the coefficient of determination (R^2) was calculated to express how well ADXL001 sensor measurements compared to model 64B sensor measurements. The coefficient of determination is a statistical term which predicts future outcomes based on other related variables. In this project, the main variables are impact peak values. It also formulated the relation between Reference and IMG sensor measurement in terms of peak g values. In other words, it formulated the related regression line. As the formula of regression line is defined Y = Ax + B, the value of parameter "A" corresponds to

the percentage of system deviation from perfect correlation between IMG and Reference values, and the value of parameter "B" is the y-axis intercept, or total bias for IMG when no acceleration is sensed by the reference.

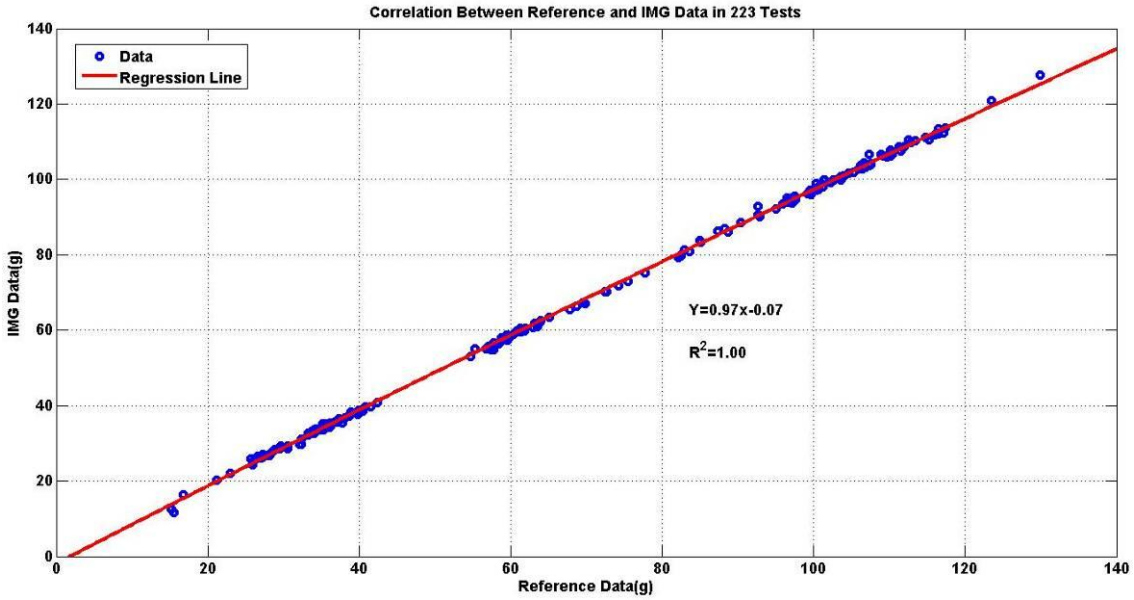

Figure 3.42 Correlation between Reference and IMG data in terms of peak g values.

Experimental Uncertainty Analysis

According to experimental uncertainty analysis, ADXL001 linear accelerometer has 2.9% bias uncertainty and 2% random uncertainty, as shown in Figure 3.43.

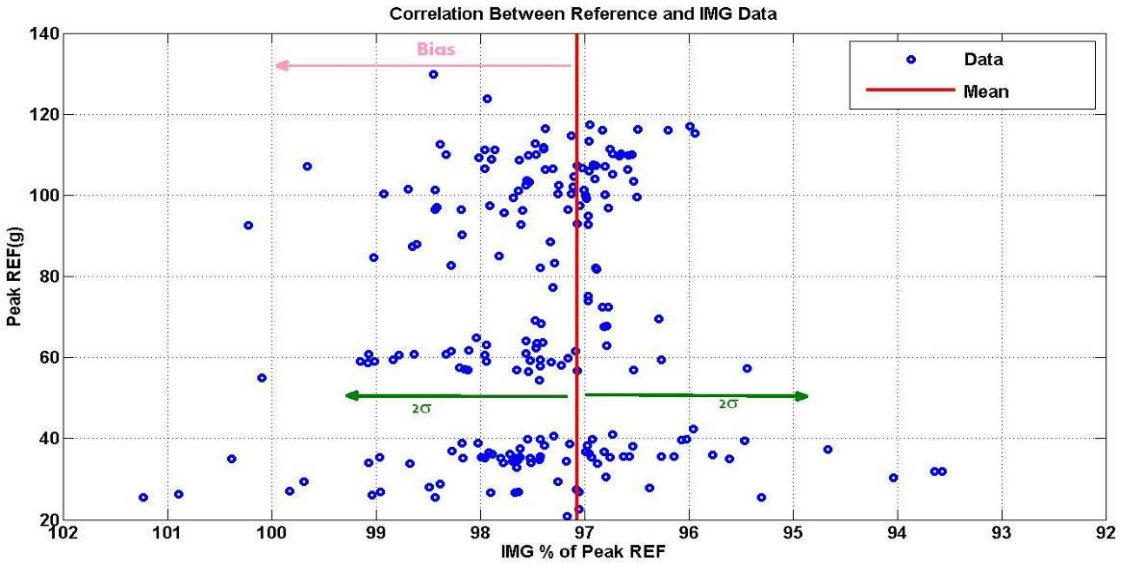

Figure 3.43 Experimental Uncertainty Analysis Results with Bias and Uncertainty Values

Even though there is no random uncertainty difference between theoretical and experimental uncertainty analysis, there is approximately 1% bias uncertainty difference between them. In order to figure this problem out, the effect of cross-axis sensitivity uncertainty on each test was quantified, and presented in Figure 3.44.

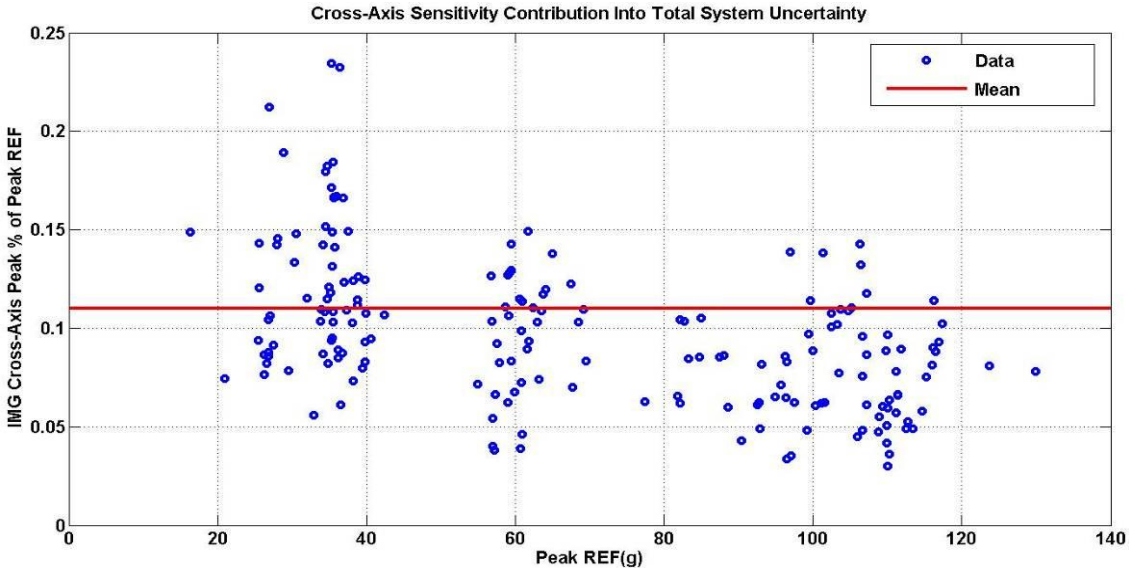

Figure 3.44 Cross-Axis Sensitivity Contribution into Total System Uncertainty.

According to the related figure, cross-axis sensitivity contributed approximately 0.11% bias into IMG measurement. However, there is still 0.9% bias difference between theoretical and experimental uncertainty analysis. According to the related datasheet, it is also known that sensitivity contributed approximately 1.8% bias into IMG measurement. After summation of bias values contributed by cross-axis sensitivity and sensor sensitivity, total uncertainty value in experimental uncertainty became calculated that is equal to 1.91%, which is almost 1% larger than the theoretical uncertainty analysis.

Conclusion of ADXL001 Linear Accelerometer Testing

The main purpose of ADXL sensor testing was to compare ADXL sensor theoretical uncertainty calculations with experimentally determined uncertainties. In order to prove the quality of the sensor in measuring linear acceleration, model 64B sensor was involved to gather reference data in all drop tests. In initial studies, the quality of test fixture was evaluated by using different types of foams. Results show that test method was sufficiently convenient and repeatable.

L3G4200D Gyroscope Testing

Materials & Methods

Expected Results

The purpose of L3G4200D tests was to compare IMG PCB gyroscope theoretical and experimental uncertainty in terms of angular rotation measurements. Before the start of performance tests, it was necessary to do some research about possible outputs because in order to determine whether collected data were satisfied or not, the expected results should be analyzed first and then test data can be compared to results in literature. according to literature search, angular speed results of impact tests had generally Z shaped signals and peak values were varying ranging from 5 up to 40 rad/s[31,32,33].

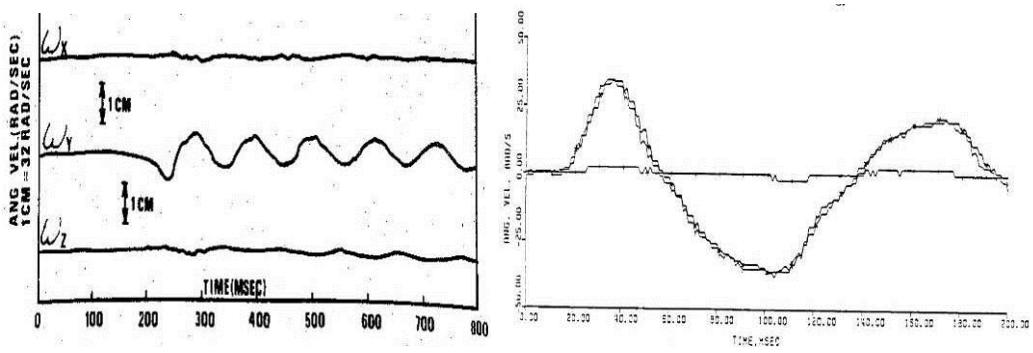

Figure 3.45 Literature Measured Angular Speed with Multiple Linear Accelerometers[34] (**left**) and Multi Directional Gyroscope Performance Test Result[35] (**right**).

In order to prevent any misinterpretations on prospective dynamic rotation tests, a simple static rotation test setup was established to observe the IMG angular

rate sensor response to single axis rotation. This test setup was predicted to provide basic but important outcomes for the three-axial IMG angular rate sensor.

Mechanical Setup

In order to simply test IMG gyroscope, IMG PCB was tested with the contribution of a DC Encoder constant angular velocity turntable. In order to have a better idea about IMG gyroscope zero input response and static noise, five working IMG PCBs with gyroscope were attached on a level table before the first static test. Results were taken notes to use further IMG gyroscope data analysis. As the first attempt, five identical flat IMG PCBs were mounted on three different sides of a rectangular box, made from plastic, attached to a black metal plate of a turntable, respectively. The speed of turntable was controlled with a DC Encoder (Stanford Research Systems Inc., Sunnyvale, CA, USA). The DC Encoder controlled the speed of turntable with a motion sensor attached to the black metal plate. The motion sensor counted the revolution number of the spinning disc and was capable to rotate it up to 250 rad/s. Flat IMG PCBs were attached to top and sides of the rectangular box to do measurements for each axis (**Figure 3.46**).

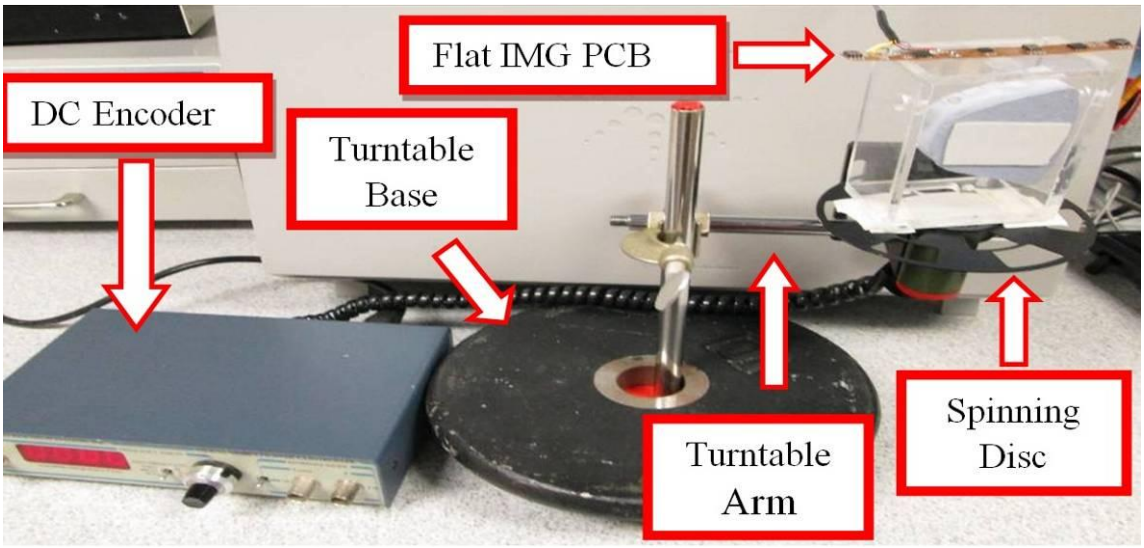

Figure 3.46 DC Encoder and Turntable with a Flat IMG PCB

IMG Circuit Board Adjustments

User selectable IMG PCB options were adjusted before the static rotation impact tests to gather optimum rotation results. Cut-off frequency of the IMG gyroscope built in low-pass filter was set to 110Hz, which is the maximum selectable value for the gyroscope. The IMG gyroscope sampling rate was set to its maximum value (800 Hz) to minimize the risk of data loss. Additionally, the IMG itself duplicated the collected data five times to mimic a 4000Hz sampling rate. Like in the linear impact tests, impact duration of the IMG gyroscope was set to 125ms and its pre-triggering time was adjusted in a range between 50-100 ms to determine angular rate sensor zero-g-offset value and stability analysis.

Results

At the end of IMG gyroscope tests, 65 DC Encoder rotation tests were completed using the five PCBs. According to the results of the first part of IMG gyroscope tests, maximum zero input response was about 0.4 rad/s, which was a negligible number for this project.

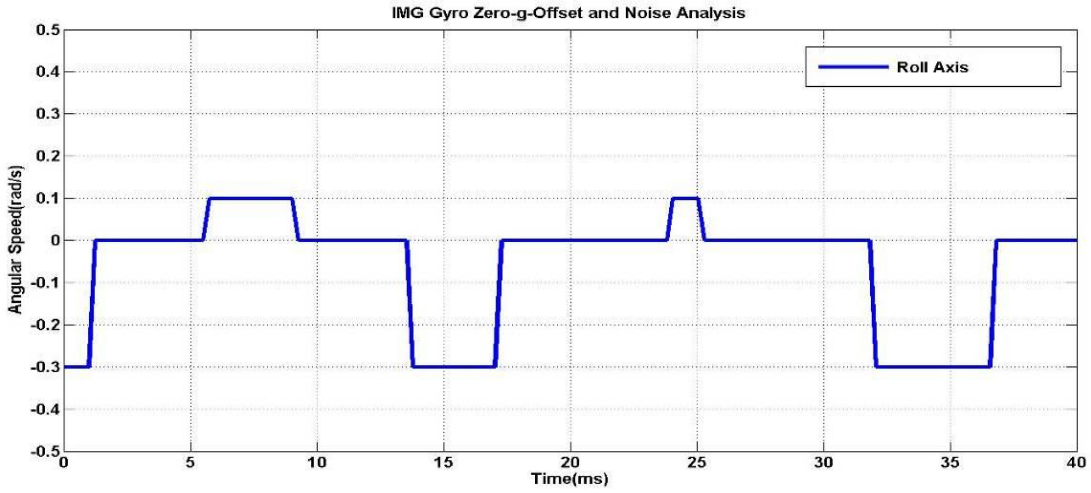

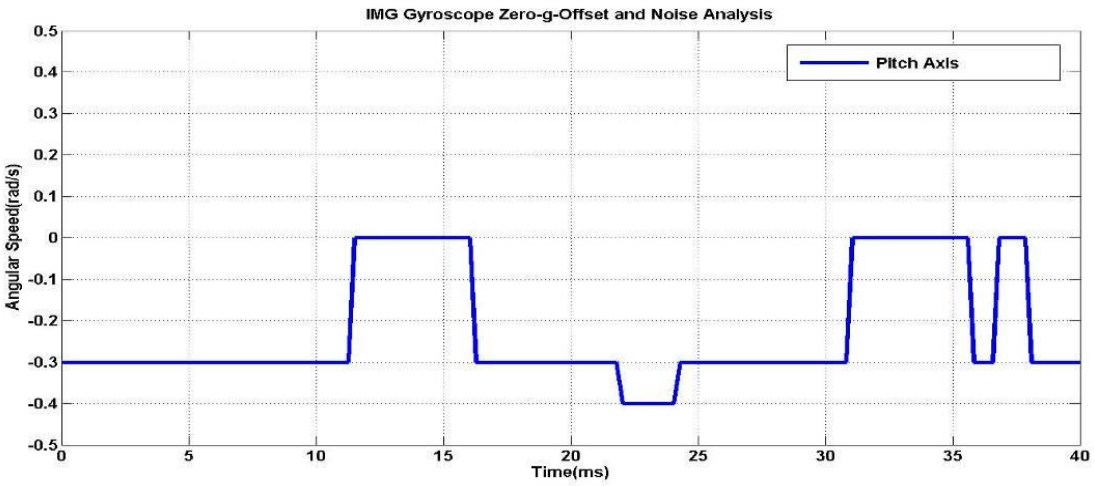

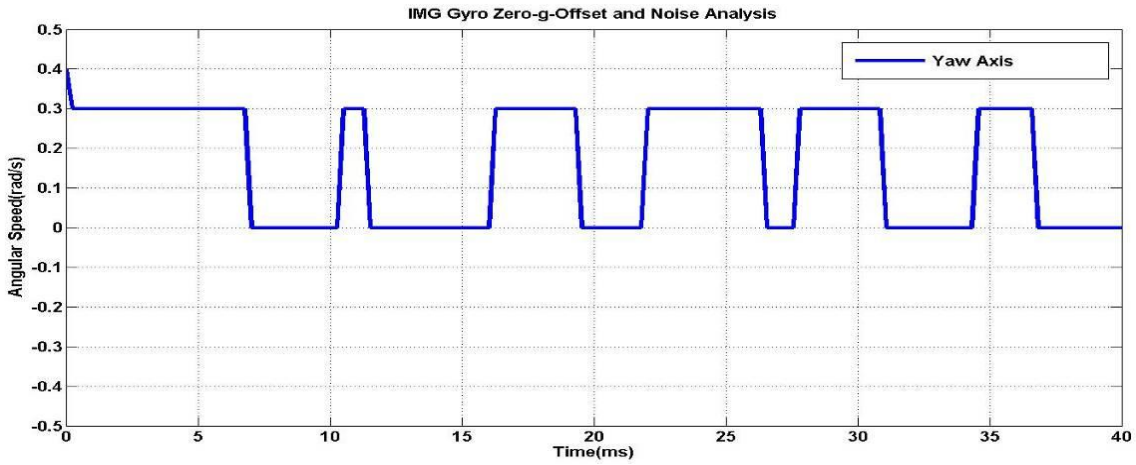

Figure 3.47 Zero-g-Offset and Noise Analysis of a Flat IMG PCB for Roll (**top**), Pitch (**middle**) and Yaw Axes (**bottom**)

At the second part of the study, IMG gyroscope performance was tested with a DC Encoder controlled turntable. As planned before the test, five flat IMG PCBs were exposed to five different rotational speed rates for each axis, respectively. After the test, response of each IMG PCB was analyzed in terms of stability, noise captured at different speed levels, and IMG gyroscope limitations. IMG gyroscope responses for each axis are shown below:

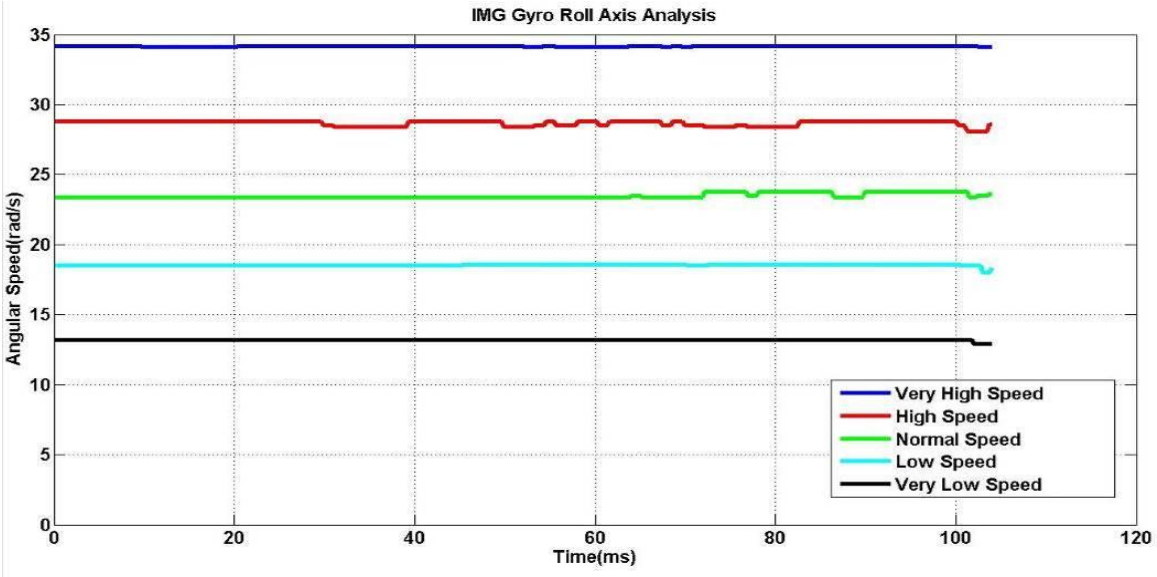

Figure 3.48 A Sample IMG Gyroscope Performance Test Results on Roll Axis

As seen in Figure 3.48, IMG gyroscope exhibits maximum 0.4 rad/s static noise in angular speed measurement while working at a certain/known speed level. For the sake of brevity, only roll axis results were presented. As expected, pitch and yaw axis angular speeds did not exceed 0.4 rad/s static noise limit.

The next step was to determine reliability of the response of each IMG gyroscope axis under the same condition. This step also defined the gyroscope accuracy and precision level (**Figure 3.49**).

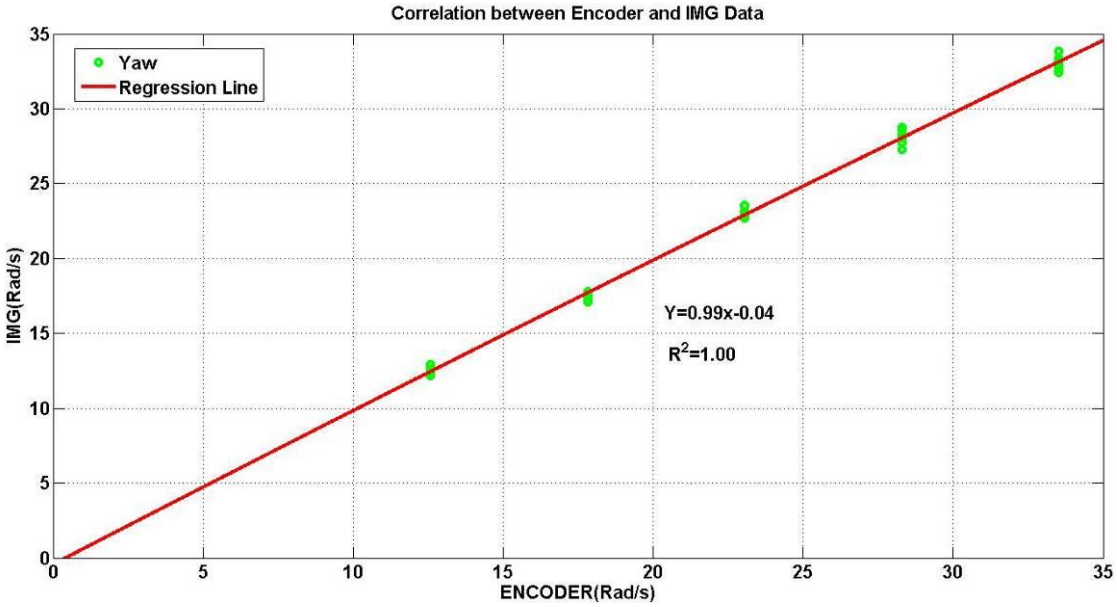

Figure 3.49 Correlation between Encoder and IMG Data For Yaw Axis. Five IMG PCBs were tested at five different speeds, and roll/pitch/yaw axes, in unit of rad/s. A Total of Twenty-Five Data Points Are Displayed.

Experimental Uncertainty Analysis

According to experimental uncertainty analysis, L3G4200D angular rate sensor has 0.3% bias uncertainty and 1.7% random uncertainty, as shown in Figure 3.50.

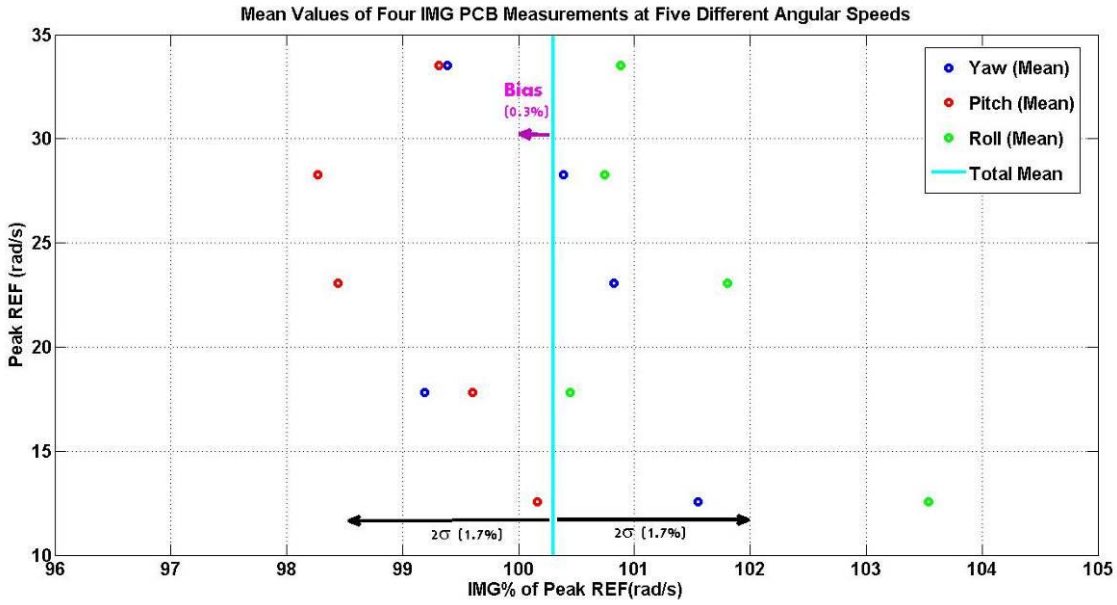

Figure 3.50 Experimental Uncertainty Analysis Results with Bias and Uncertainty Values

Conclusion of L3G4200D Gyroscope Testing

The main purpose of static rotation tests was to compare L3G4200D theoretical and experimental uncertainty. In order to prove the quality of the sensor in measuring angular speed, a DC Encoder was involved to gather reference data in all static rotation tests. In initial studies, the quality of test fixture was evaluated by repeating some static rotation at the same speed. Results showed that test setup was sufficiently convenient and repeatable. Figure 3.48 exhibits that static noise captured by the IMG gyroscope is independent of angular speed and not exceeding 0.4 rad/s for each measurement. Figure 3.49 also shows that each axis of the IMG gyroscope does the same sort of measurement and the results are almost identical, which means the IMG gyroscope is a reliable sensor to be used in angular rotation tests similar to the conditions studied using the DC Encoder.

CHAPTER IV

DISCUSSION

The ultimate goal of this study was to compare theoretical and experimental uncertainties of an impact-sensitive electrical circuit in several bench-top tests. Before the start of bench-top testing, possible sources of theoretical IMG linear accelerometer uncertainty were determined and how these sources individually affected the system was scrutinized. Individual uncertainty values were either calculated or collected from some related documents (datasheets, specification sheets, etc.). The same method was applied for the calculation of IMG gyroscope uncertainty. Consequently, uncertainty numbers for both IMG sensors were satisfying and also close to estimated uncertainty values (equal or greater than 95%). After the theoretical uncertainty analysis, the IMG PCB was exposed to linear impacts for evaluating linear accelerometer reliability. Several foams with different stiffness values were preferred for these series of tests to observe variability of IMG linear accelerometer responses in terms of peak g values and impact durations. Linear impact tests were performed with five different types of impacted surfaces (rubber, extra soft, soft, firm foams, and Airex pad). Each of foams experienced an impact provided by a sliding aluminum released from five different drop heights (32”, 25”, 23.4”, 9”, and 6.5”). This testing fashion was repeated for five

identical IMG PCBs. Results pointed that IMG PCB linear accelerometer was capable to accurately (%98.2) and precisely (%98) capture any impacts whose peak acceleration values ranging from 20g up to 250g and impact durations up to 125ms, which is a sufficient number for a real impact because, as mentioned previously, real head impacts lasting up to 25ms. Additionally, IMG linear acceleration data were compared to reference sensor data. The difference between IMG and reference sensor measurements were less than 5% in terms of peak values, impact duration, and area under curve. These results suggest that the IMG linear accelerometer may report peak linear acceleration within 1% accuracy and 2% precision in-vitro and in-vivo IMG tests to be performed in the future.

After completing linear accelerometer testing, IMG gyroscope uncertainty was theoretically and experimentally determined. In order to determine IMG gyroscope zero-g-offset value, five flat IMG PCBs were attached on a smooth surfaced table. Artificial very low impacts were used to trigger IMG PCB. Collected data were analyzed and all results consistently pointed that the maximum IMG PCB zero-g-offset value was never greater than 0.4 rad/s, which was a negligible number when comparing it to the gyroscope full scale of 34.9 rad/s. Next, the IMG gyroscope was attached to a turn table, whose angular speed was controlled with the contribution of a DC Encoder. The purpose was to consider IMG gyroscope static noise versus constant rotational velocity. All three axes of the gyroscope were tested with five different angular velocities (34rad/s, 29rad/s, 24rad/s, 19rad/s, and 14rad/s). This testing method was repeated for five identical IMG PCBs. Related results consistently indicated that regardless of IMG PCB operational speed below full scale value, IMG PCB static noise was never greater than 0.4 rad/s. These results make the IMG gyroscope as a reliable tool to measure three-axial impacts.

CONCLUSION

Head injury is a major problem for professional sports players, especially for American Football and Ice Hockey players. Even though significant developments regarding human brain dysfunctions screening have been accomplished by scientists, there is no off the shelf device to instantly diagnose severe or mild traumatic brain injuries. As promising performance test results indicated in this study, the “Intelligent” Mouth Guard (IMG) under development at Cleveland Clinic may be able to fill this gap in the future. Moreover, since all required performance tests were successfully completed, IMG might also be modified for the usage of head injury diagnosis in several areas like car crash tests and tests for military equipment.

CHAPTER V

FUTURE WORK

Introduction

In future work, the influence of custom data filtering should be examined. Because SAE J211 was designed for high frequency head impacts to the interior of an automobile, it would be advantageous to determine custom filtering requirements for lower frequency impacts such as occur in athletics. This section details some preliminary concepts relevant to this custom filtering.

$Sinc^2$ Analysis

Background

Theoretically, in order to prove whether two signals are the same or highly similar, these signals have to be compared both in time and frequency domains. It is also known by Fourier's Theorem that all continuous signals can be expressed as a combination of sine and cosine waves. Therefore, as the first attempt, a set of

experimental impact test data was analyzed and its shape and frequency components were determined in Matlab. After that, some fundamental signals were modeled in Matlab and their Fast Fourier Transform (FFT) responses were compared to the FFT of the real data in terms of shape, amplitude and frequency. Consequently, FFT of $sinc^2$ function was considered as the best match with the real data versus preliminary investigation of square, triangular and simple sinusoidal signals. In time domain, the $sinc^2$ function can be represented as a multiplication of two sinc waves. In mathematics, there are two types of sinc function: unnormalized and normalized sinc functions. These functions are formulated as shown below:

$$\text{Unnormalized Sinc Function: } \operatorname{sinc}(x) = \frac{\sin(x)}{(x)}$$

$$\text{Normalized Sinc Function: } \operatorname{sinc}(x) = \frac{\sin(\Pi x)}{\Pi x}$$

Similarly, in frequency domain, the $sinc^2$ function can be expressed as a convolution of identical sinc waves. Convolution is a mathematical operation that shows the relation between two functions in terms of overlap. In light of this information, it is obvious to say that FFT of summation of two sinc waves gives the same outcome with convolution of FFT of two sinc waves.

Matlab has its own sinc function to generate a simple sinc wave. However, sinc function in Matlab is based on unnormalized sinc function, which is generally used in statistics. This means that a normalized sinc function must be generated, which is commonly used in digital signal processing and data analysis. Hence, a normalized sinc function was manually created based on its mathematical formula. Figure 5.51 shows the difference between normalized and unnormalized sinc function in terms of signal shape.

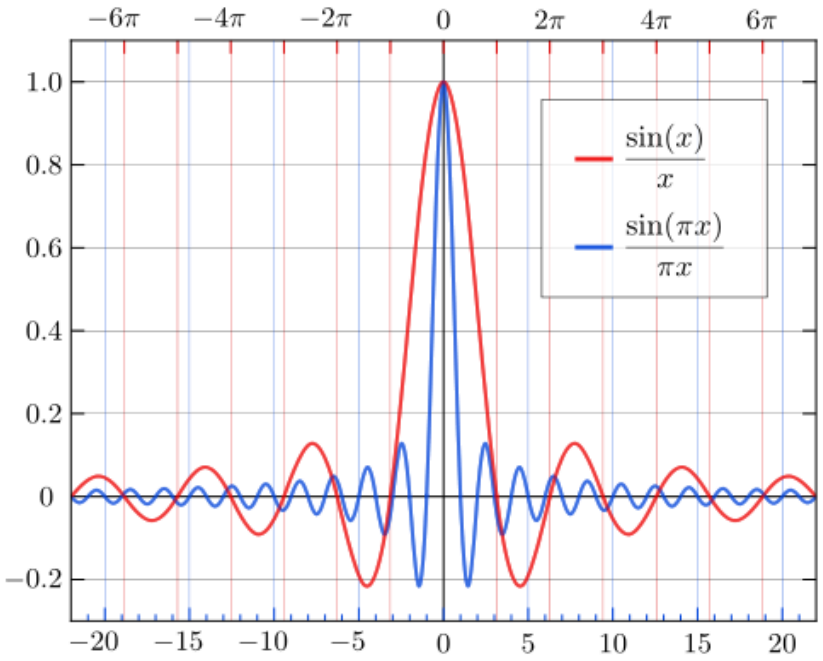

Figure 5.51 Relation between Normalized **(Blue)** and Unnormalized **(Red)** Sinc Functions.

The fundamental frequency is simply defined as the lowest frequency of a periodical signal. It can be calculated with the contribution of period of the signal. For instance; if period of a signal is 20 milliseconds (ms), fundamental frequency of the signal is $\frac{1}{20}$ ms, which is also equal to 50 Hz.

The zero crossing point is a point where the sign of a function changes. Assume that the generated sine wave in Matlab is defined as;

T = sin(2*pi*f*t) where;

f = input frequency,

2*pi*f = zero crossing frequency,

Fundamental frequency = half of zero crossing frequency

Assume that the generated normalized sinc wave in Matlab is defined as;

$Y = A \sin(2*pi*f_i*t)./ (2*pi*f_i*t) = \text{sinc}(2*pi*f_i*t)$ where;

A = Amplitude

f_i = input frequency = fundamental frequency,

Zero cross frequency = 0

Accordingly, assume that the generated normalized sinc^2 function in Matlab is defined as;

$Y = A (\sin(2*pi*f_i*t)./ (2*pi*f_i*t)).\text{^}2 = \text{sinc}^2(2*pi*f_i*t)$ where;

A = Amplitude

f_i = input frequency = 2 * fundamental frequency

Zero cross frequency = 0

There is a difference between the sinc wave and sinc^2 function in terms of relation between input and fundamental frequencies. This difference can be simply explained with the convolution of signals because it is known that multiplication of two signals in time domain corresponds to convolution of them in frequency domain. Therefore, convolution of two sinc waves, which have the same input and fundamental frequencies, creates a sinc^2 function that has the same input frequency, but two times greater fundamental frequency than each of the sinc waves.

Matlab uses a Fast Fourier Transform (FFT) algorithm to compute Fourier Transform of a waveform. FFT is an algorithm to calculate discrete Fourier Transform and its inverse. FFT function in Matlab is based on a simple formula shown below:

$$X(k)=\sum_{j=1}^{N} X(j)\, w_N^{(j-1)(k-1)}$$

Where;

$$w_N=e^{(-2\Pi j)/N}$$

Assuming x(t) = A cos(w_0t)$\omega_0 t$) and FFT of x(t) is equal to X(w).

$$X(w\omega) = \int_{-\infty}^{\infty} X(t)\, e^{(-jwt)}\, dt$$

$$= \int_{-\infty}^{\infty} A\cos(w_0 t)\, e^{-jwt}\, dt$$

$$= A\int_{-\infty}^{\infty} \cos(w_0 t)\, e^{-jwt}\, dt \qquad \cos(w_0 t) = \frac{e^{jw_0 t}+e^{-jw_0 t}}{2}$$

$$= A\int_{-\infty}^{\infty} \left(\frac{e^{jw_0 t}+e^{-jw_0 t}}{2}\right) e^{-jwt}\, dt$$

$$= A\int_{-\infty}^{\infty} \left(\frac{e^{j(w_0-w)t}+e^{-j(w_0-w)t}}{2}\right) dt$$

$$= \frac{A}{2}[\delta(w_0-w)+\delta(-w_0-w)] \qquad \delta(f-f_0)= \int_{-\infty}^{\infty} (e^{j(w-w_0)t})\, dt$$

$$= \frac{A}{2}\,[\delta(w_0-w) + \delta(-w_0-w-\omega_0-\omega)]$$

$$= \frac{A}{2}\,[\delta(w-w_0\omega-\omega_0) + \delta(w+w_0\omega+\omega_0)]$$

$$= \frac{A}{2}\,[\delta(f-f_0 f-f_0) + \delta(f+f_0 f+f_0)]$$

A Bode plot is a graph of the transfer function of a system to show the frequency response in the logarithmic scale. A Bode plot is a useful way to determine the relation between known output and known input for a given frequency, which is also called frequency response of the system. The Bode plot also indicates amount of loss of total signal energy at certain frequency in unit of decibel (dB). If the input of the system is unknown, there are two ways to do: input can be estimated with respect to known output and known uncertainty of a system or another method can be derived to analyze energy loss of a system for a given frequency.

Methodology

Even though FFT function in Matlab is a recommended tool for analyzing frequency components of a signal this function was tested by analyzing a simple cosine function. The Fourier Transform of a cosine function was calculated by hand and then compared to the result in Matlab. Unlike the expected result, the FFT of a cosine function exhibited harmonics of a signal with very small spikes, which are also called leakage.

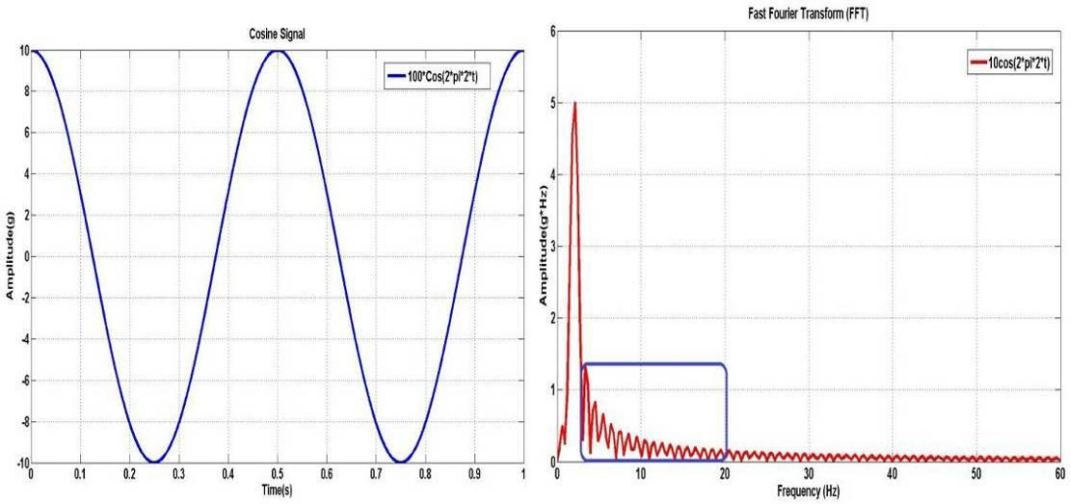

Figure 5.52 A pure cosine wave (F=2Hz) **(a)**, and its frequency spectrum **(b)**. Blue box in Figure4.49b shows unwanted leakages in FFT of the signal (AT 2Hz<F<20Hz).

After this analysis, it was decided to window the collected signal for the frequency analysis. After applying a strict windowing to the signal, the FFT of that signal looked smoother than the non-windowed signal. Moreover, FFT peak values increased and came close to values calculated by hand. "Strict windowing" means windowing the collected signal from the first zero value before peak value up to next zero value. After the strict windowing process, the FFT function was applied to all windowed signals. The shape of the signals in frequency domain was always a triangle which is similar to the FFT of a $sinc^2$ wave looks like a triangle. Therefore, as a pilot study, several $sinc^2$ waves were combined to create a test signal without noise, also called a "true signal".

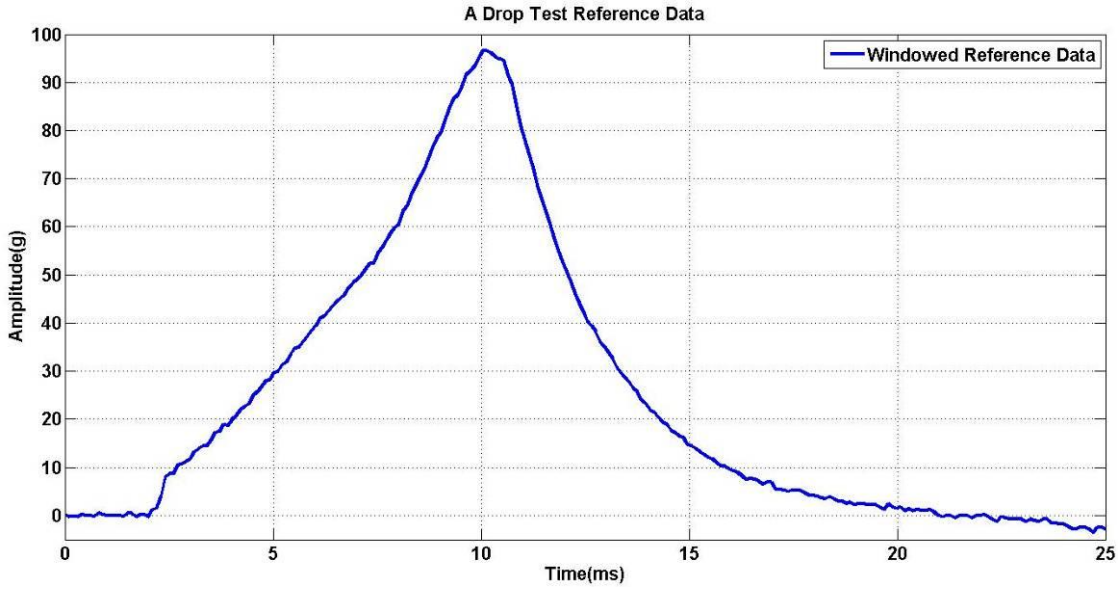
A Drop Test Reference Data
Windowed Reference Data
Amplitude(g)
Time(ms)

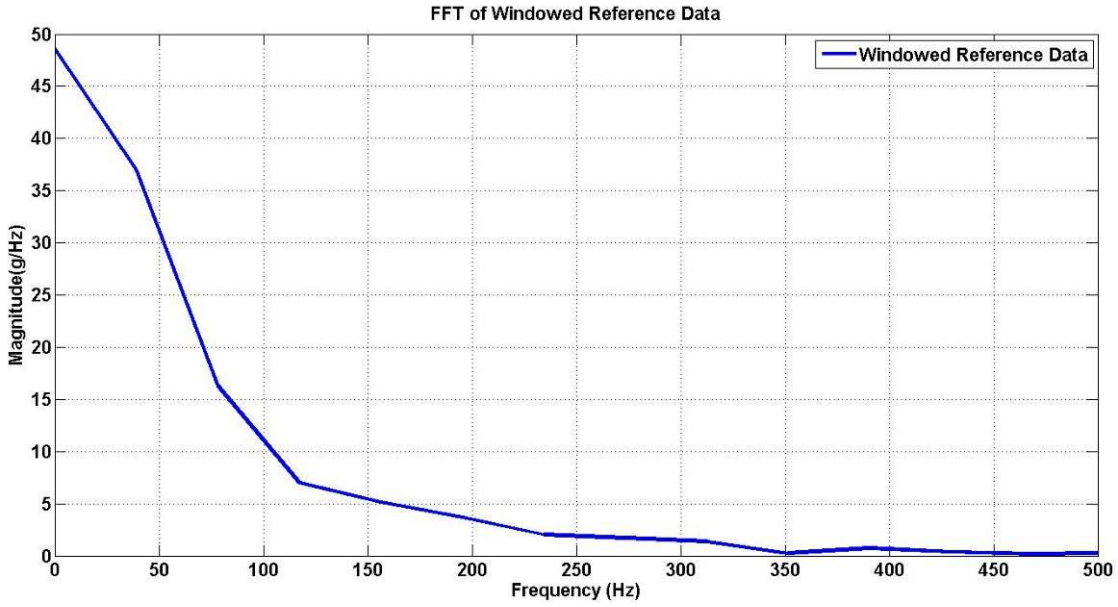
FFT of Windowed Reference Data
Windowed Reference Data
Magnitude(g/Hz)
Frequency (Hz)

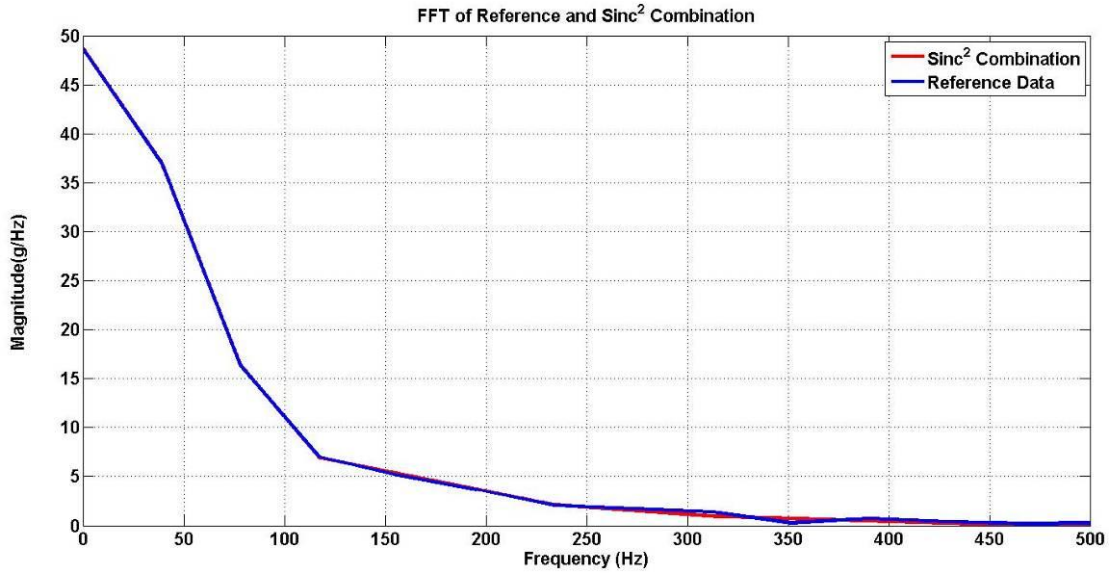
FFT of Reference and Sinc2 Combination
Sinc2 Combination
Reference Data
Magnitude(g/Hz)
Frequency (Hz)

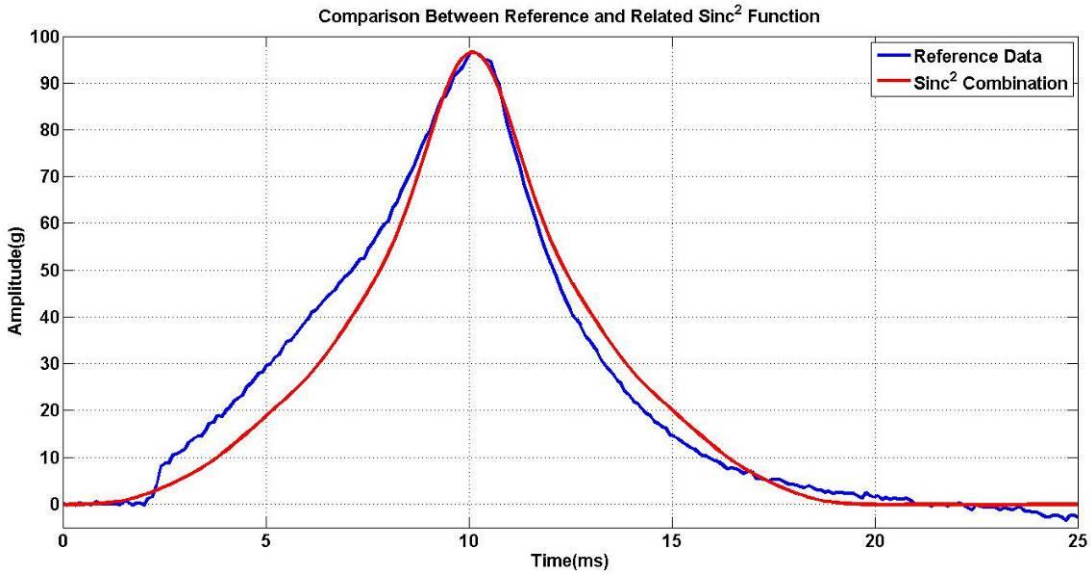

Figure 5.53 A Drop Test Data **(a)**, FFT of The Test Data **(b)**, Virtual and Reference Data in Frequency Domain **(c)**, Virtual and Reference Data in Time Domain **(d)**.

As seen in Figure 5.53.c, the FFT of the two signals have almost the same shape and amplitude values. However, inverse FFT of the two signals are pretty close but not as similar as their FFT responses. In order to quantify the similarities between these two signals, the area under curve of each signal was calculated. These results show that the method used to analyze the correlation between a real set of test data and its modeled version works fine and will be functional for analysis of test data created in similar fashion.

One problem with this method was that all required calculations were made by hand. Therefore, the second step was to automate this system and make it applicable for all test signals. Detailed information of the manuscript function is shown below, respectively:

- Once user enters a test number and runs the code, it starts reading the path of A set of signals corresponding Reference data and stores all data in an excel

document in a struct defined in Matlab. A Matlab struct is capable to store multi arrays. This process was repeated in the same fashion for IMG data.

- As expected, although uniaxial linear drop tests were performed, both Reference and IMG DAQ systems saved all signals for each axis (x, y, and z). The script determines which test performed along which axis by computing peak values for each axis (x, y, and z). After that, the script selects only one axis from Reference and IMG data and makes next computations by using numbers in this axis. At this point, desired data points are ready to use.

- Initially, the script plots Reference and IMG Data. Readings with no computation were classified as "Raw".

- After that, zero-g-offset (bias) was removed from Raw Reference and Raw IMG data and initial g values were set to zero. In order to remove zero-g-bias from raw IMG signals, mean value of the first ten points was calculated and then this calculated value was subtracted from the whole IMG signal. Removing zero-g-bias from Reference Data was done in a similar fashion, but with care to modify number of samples based on the higher reference sampling rate. After that, this mean value was subtracted from whole Reference signal.

- FFTs of zero-g-bias removed Reference and IMG data were plotted to see characteristics of signal in frequency domain.

- Strictly windowed Reference and IMG data were discretely plotted. Additionally, pulse duration of each signal was computed and then time duration, pulse duration, and peak value of each signal was displayed on these figures. Pulse durations were calculated using the estimated linear portion the

acceleration part of each signal. The first step was to find the peak value of the signal. After that, the linear was identified and then two points on the linear portion were selected to formulate a straight line that passes thru the linear portion. From the straight line intersects with x-axis to x value of peak was computed and multiplied by two to find time duration of whole test signal. During this method, instead of deceleration part of the signal, acceleration part was used because generally speaking, acceleration part of test signals were generally more stable than the deceleration part.

- FFTs of strictly windowed Reference and IMG data were discretely plotted. In the plot, two numbers were essential for the next step of data analysis, which is $sinc^2$ analysis. These numbers are maximum frequency component of the test signal and amplitude of test signal at f_0 in FFT plot. These two numbers were also important because both were used in $sinc^2$ analysis as two main parameters.

- Strictly windowed Reference and IMG data were plotted in one figure to visually compare them in terms of peak values and time duration.

- The purpose of the $sinc^2$ analysis was to generate a signal based on fundamental waves (sine, cosine, sinc, etc.) for imitating real test signals. The ultimate goal of the $sinc^2$ analysis was to optimize CFC filtering value for each test signal. As mentioned in Background section, three parameters were required to generate a $sinc^2$ function: Amplitude, input frequency and sampling rate. In terms of sampling rate, the same sampling rate was selected with the sampling rate of the test signal. Input frequencies were determined by inflection points in the FFT plot of windowed reference data. Inflection points

were considered as the point where the slope of a frequency segment changes. Amplitude of each $sinc^2$ component was computed by multiplication of frequency at inflection point and corresponding amplitude value in FFT plot. Before the application of the $sinc^2$ analysis, it was presumed reference data comprises a combination of multiple $sinc^2$ functions. It was also known that since two $sinc^2$ functions are summed in time domain, amplitude in FFT is equal to summation of FFT peak values of the two $sinc^2$ functions. Therefore, as the first step of the $sinc^2$ analysis, the inflection point at greatest frequency in FFT was firstly taken into account, the corresponding amplitude was gathered from FFT plot, and the first $sinc^2$ function was then computed. In each process, in order to compute amplitudes of $sinc^2$ functions, FFT amplitude of one inflection point was subtracted from the FFT amplitude of inflection point at next lowest frequency. The result of this subtraction was multiplied to the corresponding frequency to compute the amplitude of corresponding $sinc^2$ function. This process was repeated until reaching f_0 which is equal to zero. For example; in order to generate a combination of ten $sinc^2$ functions, this process repeated itself ten times.

- The next step was to visualize percentage of similarities between reference and combinations of $sinc^2$ function in terms of area under the curve and peak values. In order to consider whether the $sinc^2$ function method worked properly or not, the shape of the points show up in the figure titled “correlation between Reference data and windowed $sinc^2$ combinations” was evaluated. As an expected result, the initial part of the shape should express an asymptotic increase and after the shape reaches its maximum, it should continue as a straight line. This method was repeated for IMG data. At the end of this step,

both Reference and IMG $sinc^2$ combinations were successfully generated. These generated signals were accepted as true signals and were ready to use for determining the optimum CFC Filtering method. The last part of this step was to generate some noise for each true signal. Before the start of noise generation, a few Reference and IMG data were scrutinized. As a result, it was considered that the amount of noise in both signals was partially random and repetitive. Repetitive means noise values fluctuate in a certain range. In order to create that sort of noise, "repmat" and "rand" functions in Matlab were used. "Repmat" is a Matlab function that provides an array whose numbers are singly increasing and repeat themselves. "Rand" is also another Matlab function that generates uniformly distributed random numbers. A combination of these two functions was created to generate a random and repetitive noise for each true signal. After that, these calculated noise values were added related true signals and produced noisy $sinc^2$ functions that will be used in process for determining proper CFC values to filter Reference and IMG data.

- Noisy $sinc^2$ functions were filtered with CFC filters whose corner frequencies were varying in a range between 1 and 1000Hz. As calculated previously, the uncertainty of ADXL001 linear accelerometer was 3.8%, and model 64B was 1% in terms of peak values (For Detailed Information, see Appendix A). In order to find the optimum CFC value for ADXL001 linear accelerometer, the uncertainty line based on previously calculated uncertainty values was first plotted and the optimum CFC value was then determined as where peak value of CFC filtered IMG signal went down to 96.2% of Raw IMG peak value. The same method was repeated for Reference data by using previously calculated uncertainty value of model 64B. At the end of this section, optimum CFC

values for both sensors were computed. In this project, “Optimum” means that a CFC value that leads to neither overfiltering nor underfiltering because it is known that overfiltering leads to data loss, and underfiltering causes an unwanted increase of computational time and more space for data storage.

- Calculated CFC values for both Reference and IMG data in the previous section were determined and to avoid overfiltering, greater CFC value was preferred to filter both Reference and IMG data. CFC filtered signals were plotted with Raw Reference and Raw IMG data to visually prove the reliability of this method.

- The last two processes were based on peak values. At this point, the same process was repeated but this time it was based on energy value of each signal. As mentioned previously, energy calculations of each signal were based on Parseval’s Theorem. As expected, uncertainty values of energy values were less than uncertainty of peak values because uncertainty based on peak values just considers one point. However, uncertainty based on energy values involves all data points. Therefore, it was predictable that uncertainty line considered by an uncertainty number based on energy values drops little bit down. The amount of drop for each test was proportional to both peak value and time duration of the test.

Results

For the sake of brevity, the results of only one set of test data were presented. Drop test #17 was randomly selected and its results were analyzed. Related figures are presented as mentioned in data analysis section, respectively.

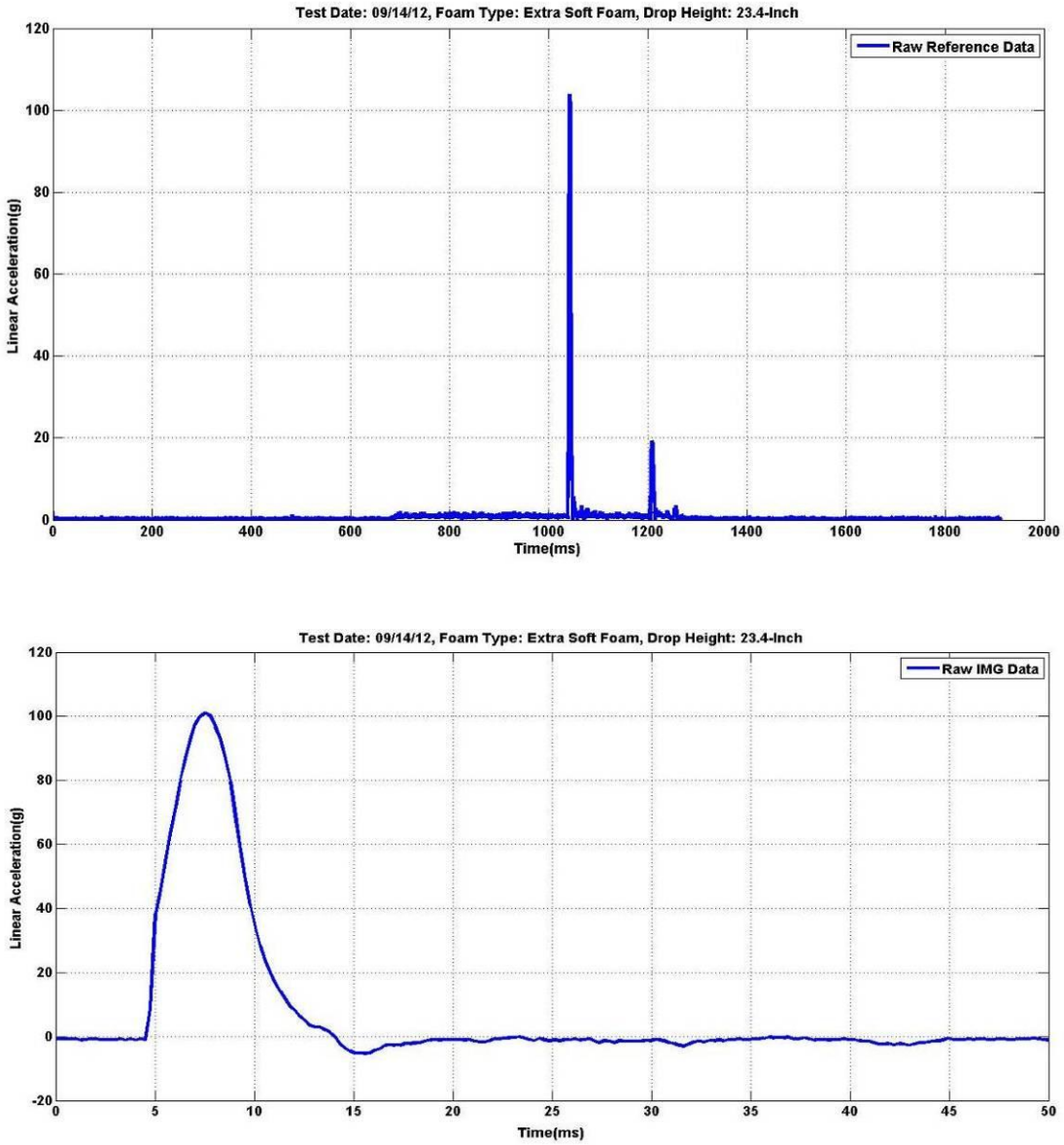

Figure 5.54 Raw Reference (**top**) and Raw IMG data (**bottom**) of Linear Drop Test performed with Extra Soft Foam and Aluminum Fixture released from 23.4”

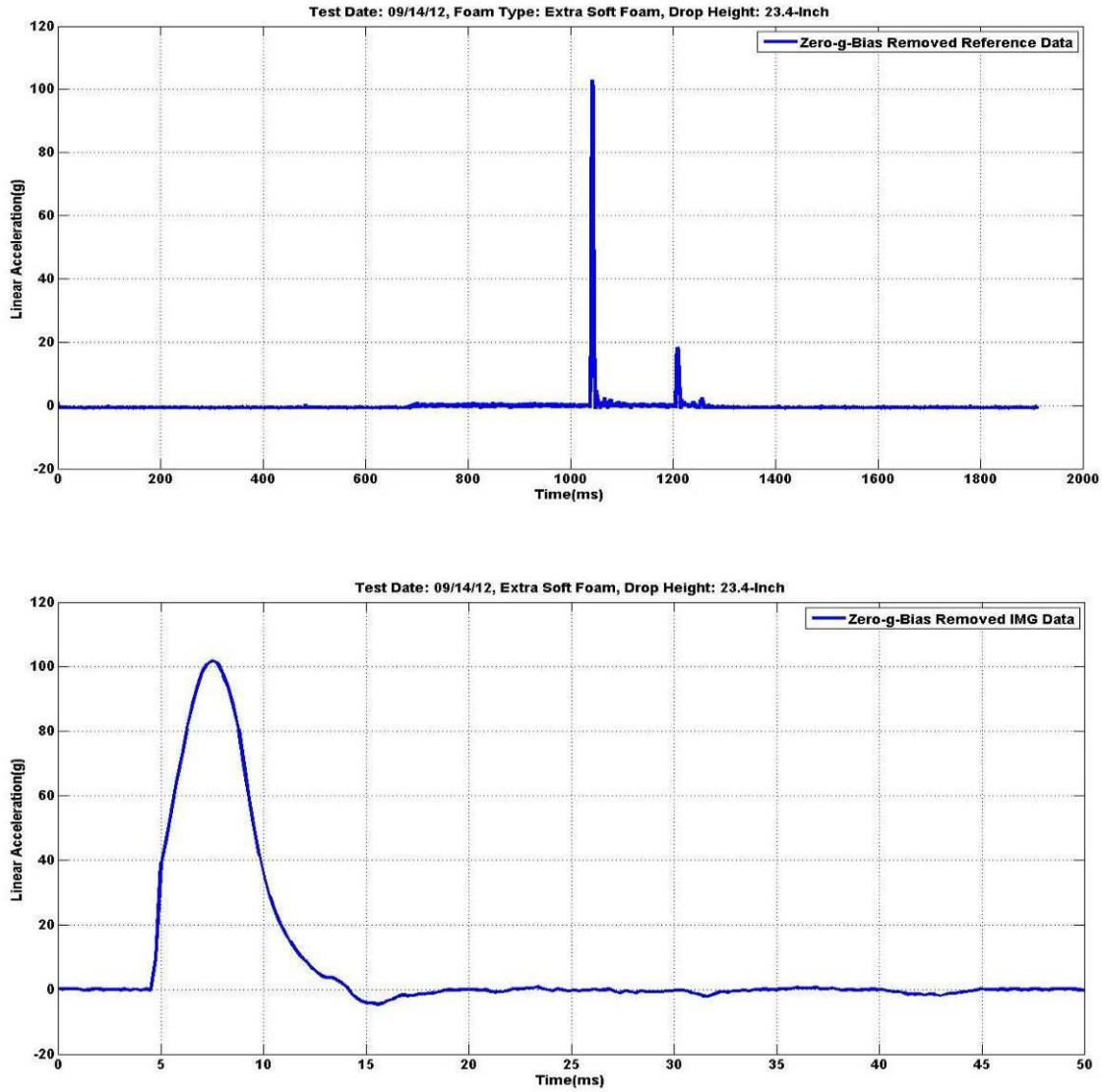

Figure 5.55 Zero-g-Bias Removed Reference (**top**) and IMG (**bottom**) data of Linear Drop Test performed with Extra Soft Foam and Aluminum Fixture released from 23.4”

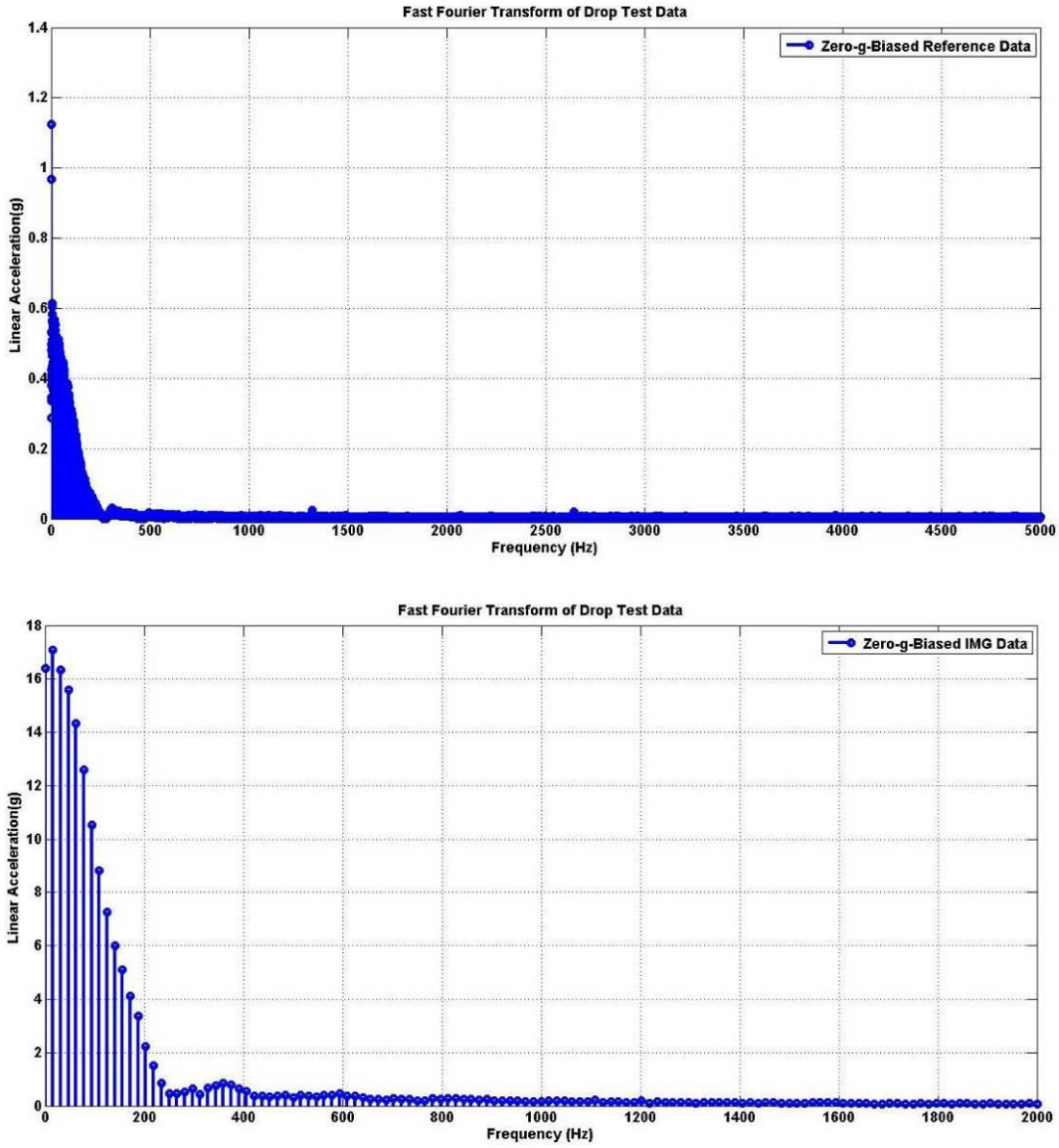

Figure 5.56 FFT of Reference Data with Sampling Frequency is 10 kHz (**top**) and IMG Data with Sampling Frequency is 4 kHz (**bottom**)

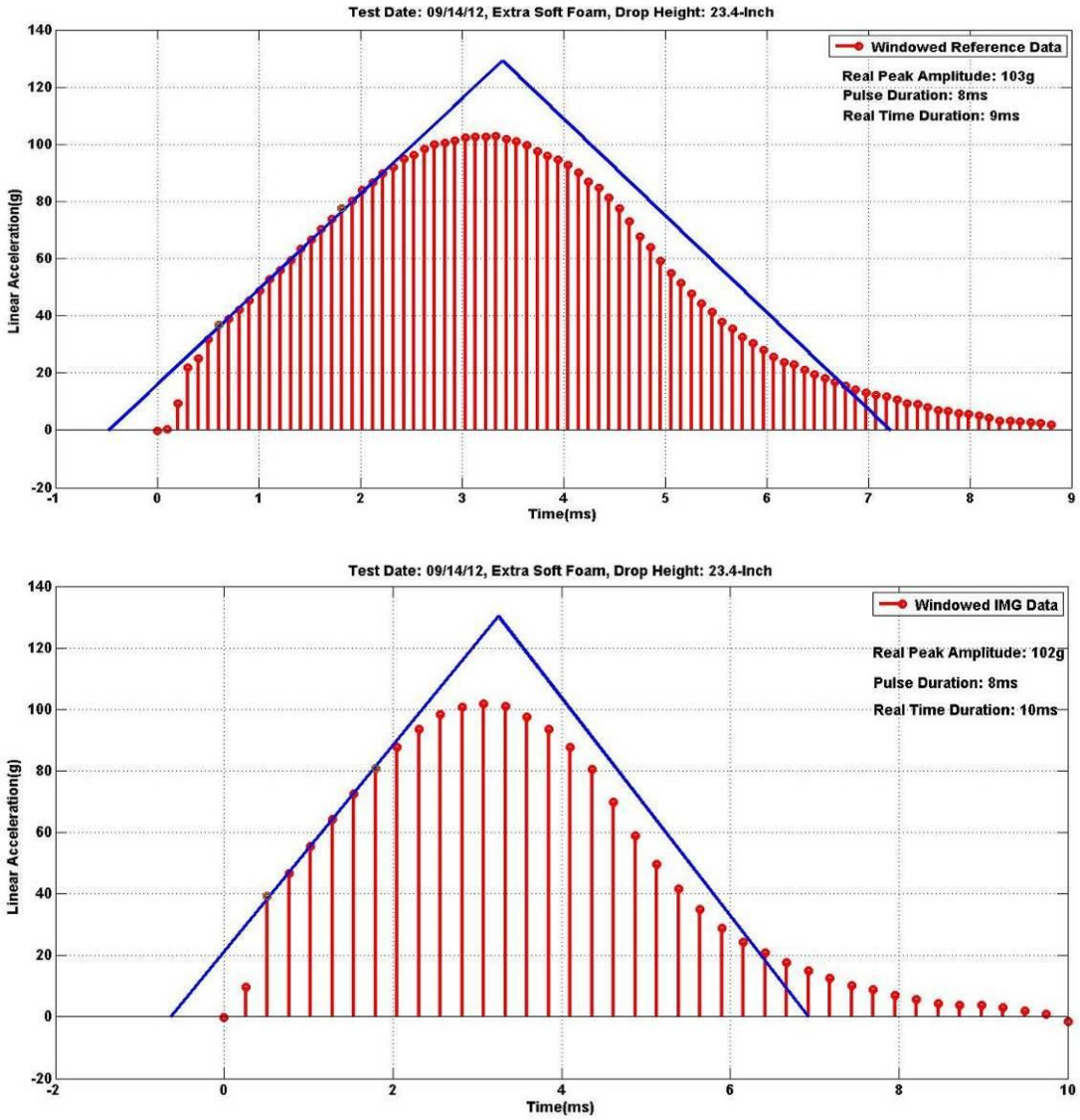

Figure 5.57 Strictly Windowed Reference (**top**) and IMG data (**bottom**). Figures include information of real peak amplitude, pulse duration and real time duration.

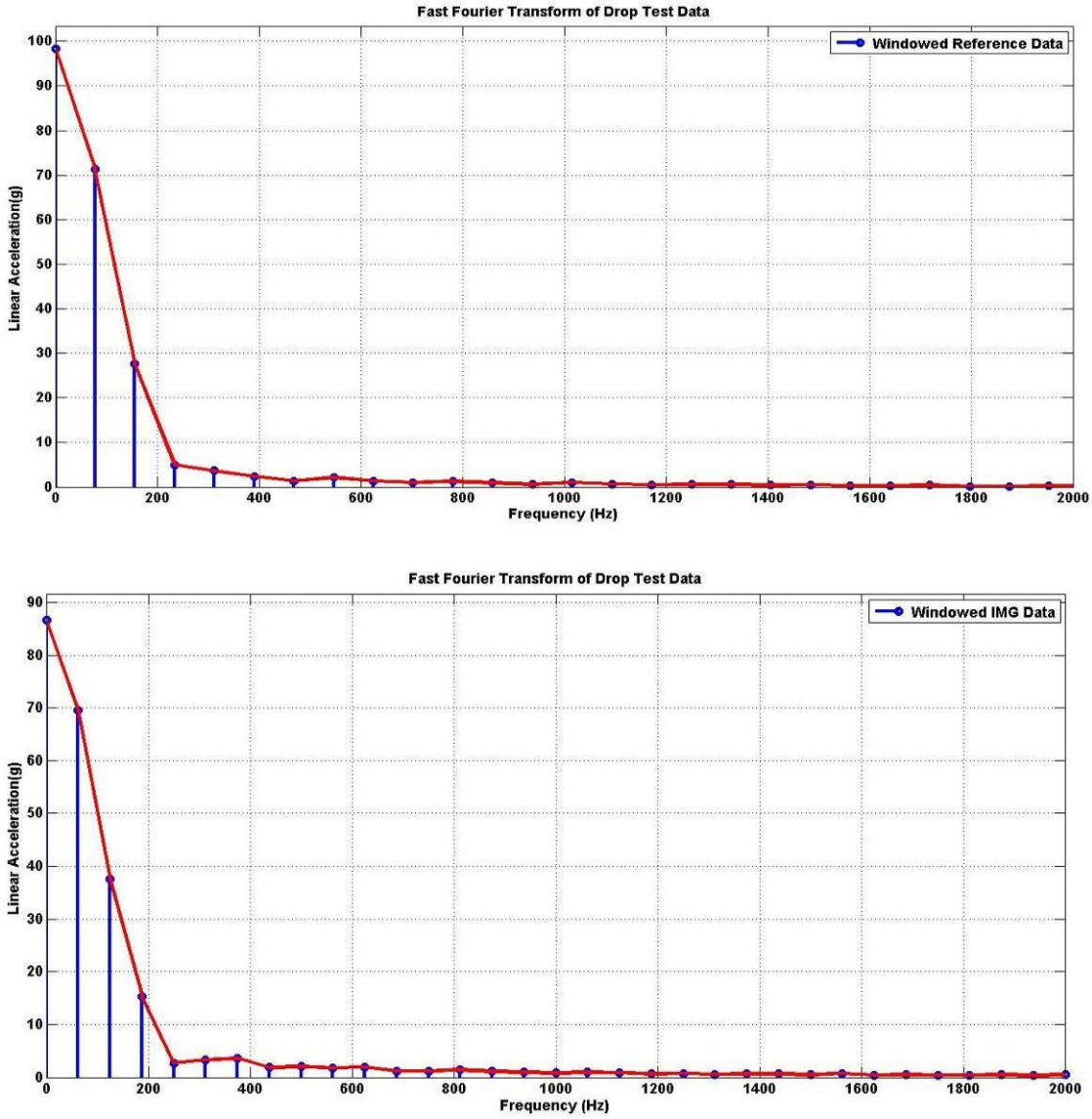

Figure 5.58 FFTs of Windowed Reference (**top**) and Windowed IMG Data (**bottom**).

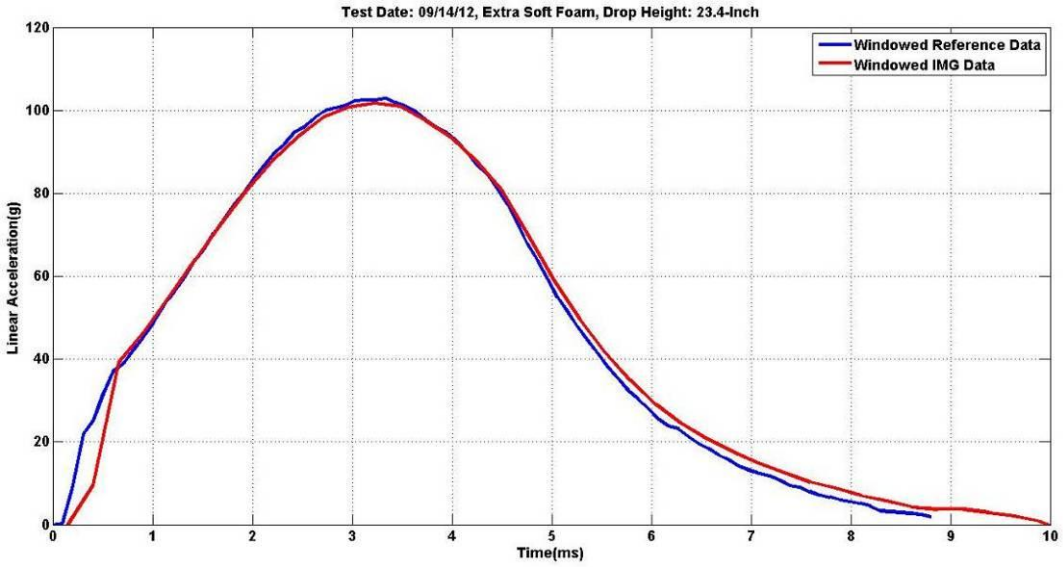

Figure 5.59 Visual Comparison between Windowed Reference and IMG Data

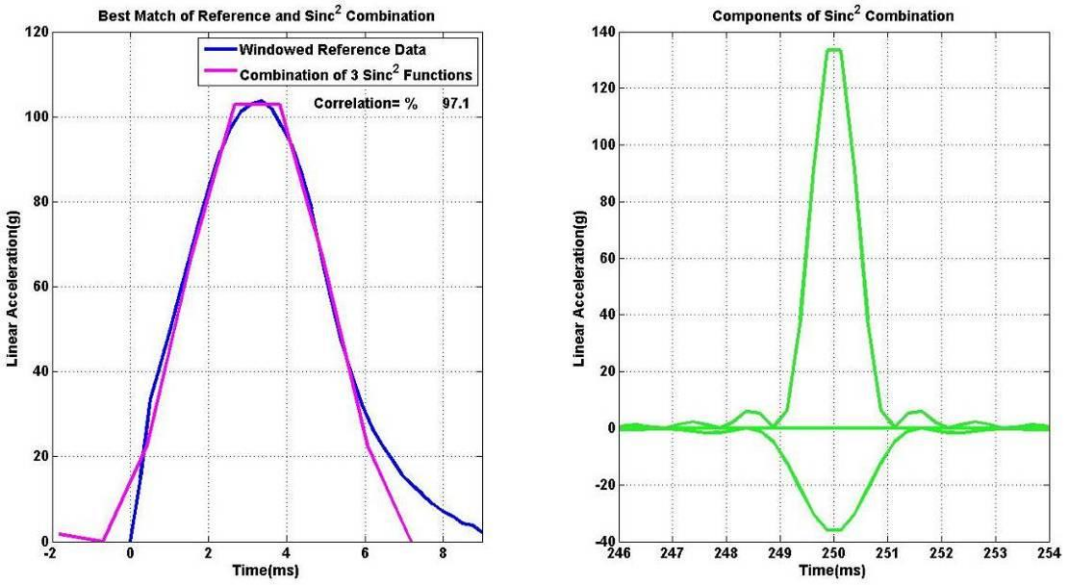

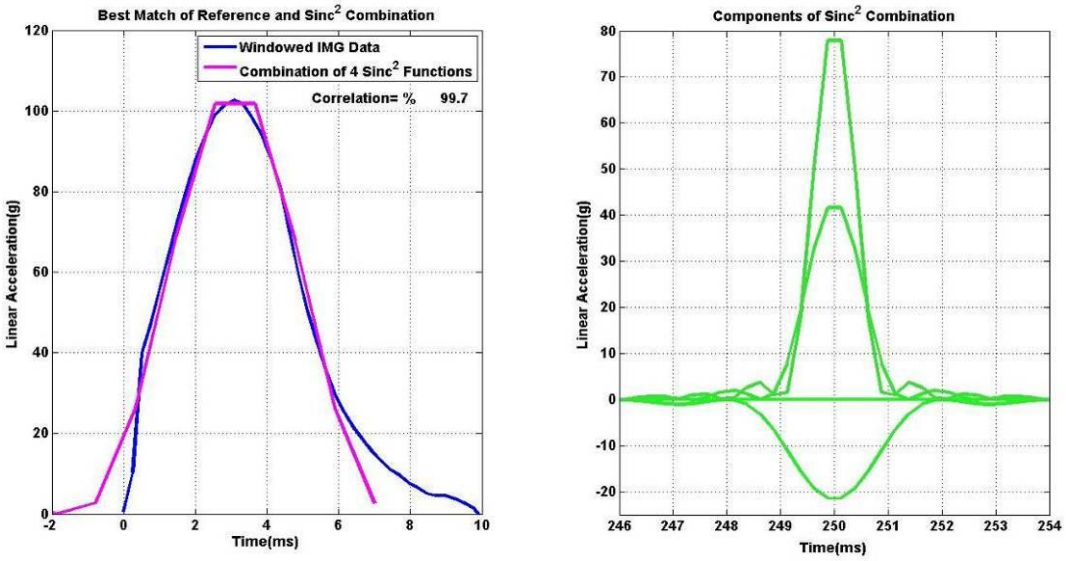

Figure 5.60 Best Matches of Combination of Sinc^2 functions with Corresponding Data Types. Correlation between windowed Reference data and related sinc^2 combination is approximately 97% in terms of area under curve (**top**). Correlation between windowed IMG data and related sinc^2 combination is about 100% (**bottom**).

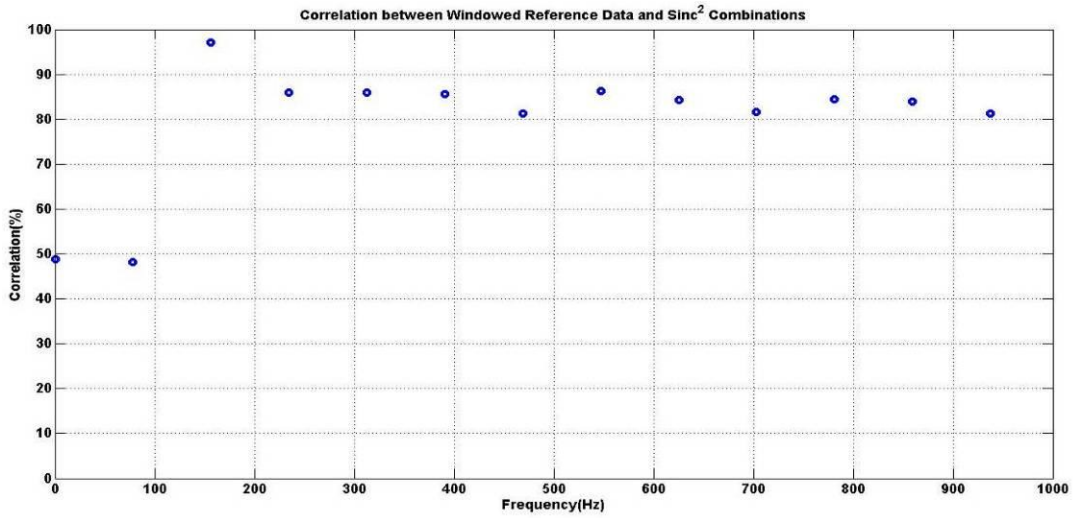

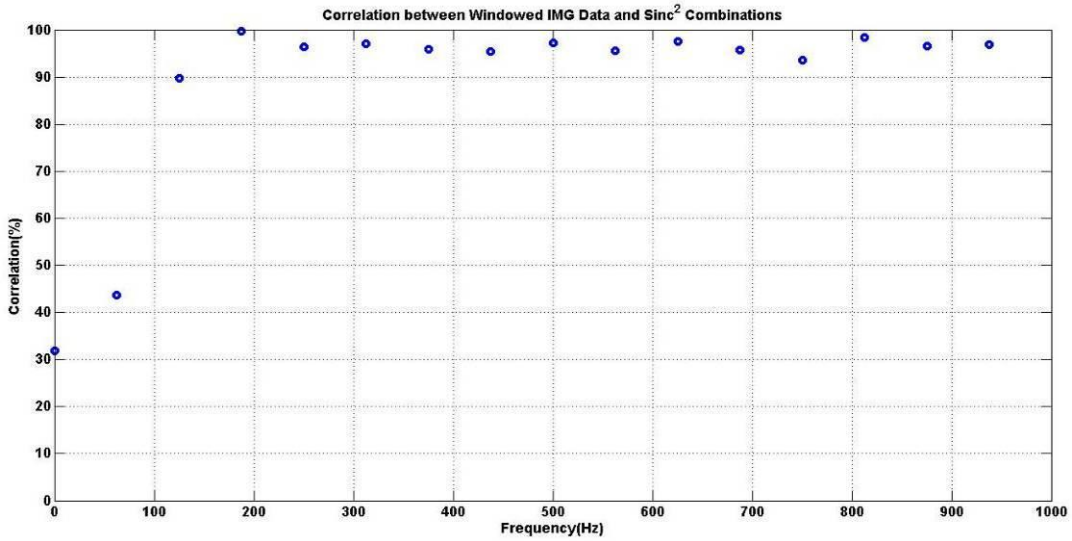

Figure 5.61 Correlation between Real Test Signals and Related $Sinc^2$ Combinations with Respect to Variance in Frequency Components.

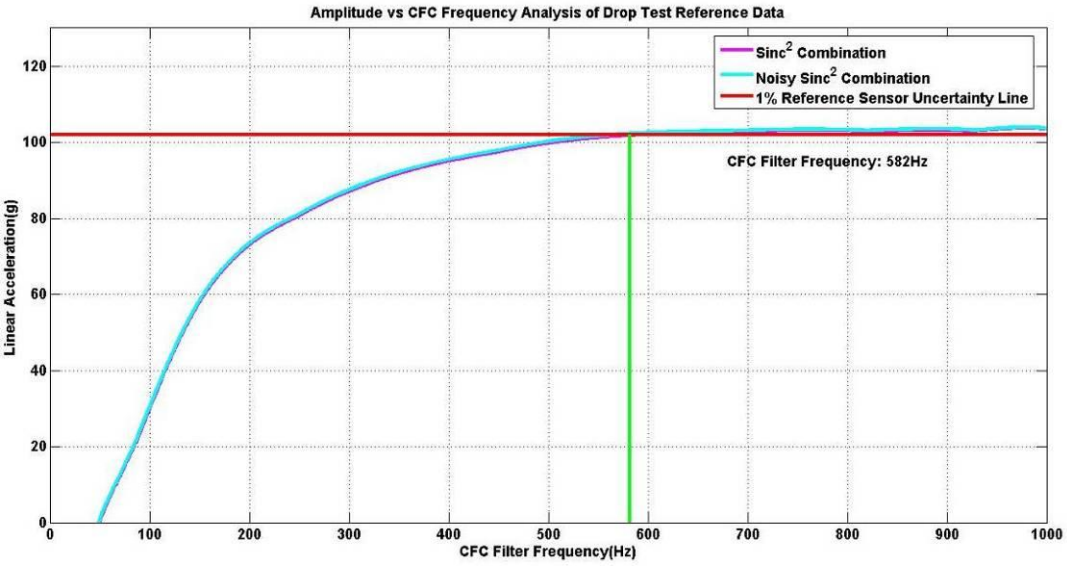

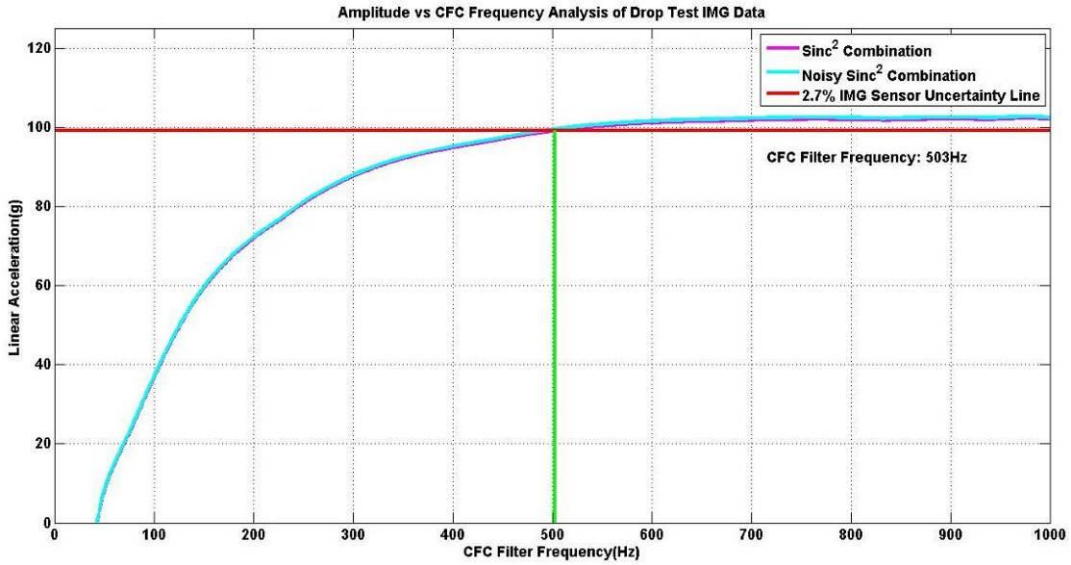

Figure 5.62 Determining the optimum CFC Filtering method based Peak Values for Reference (**top**) and IMG data (**bottom**). Red lines represent lower levels of the uncertainty value for each sensor. Green lines show the frequency values where uncertainty lines intersect with peak values of True Signals, which were filtered with different CFC Filters, whose corner frequencies singly decrease from 1000Hz down to 1 Hz.

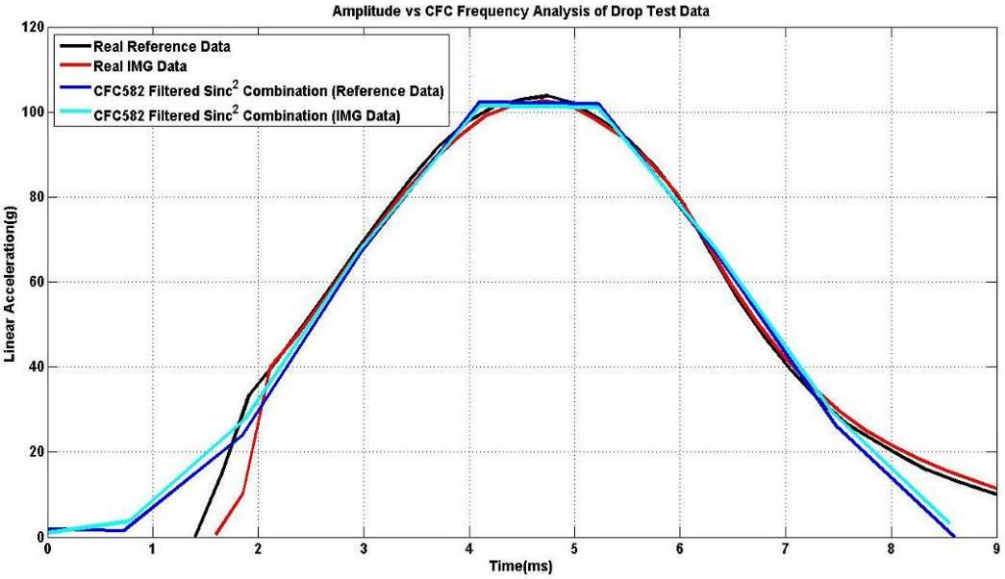

Figure 5.63 Comparison between Real Test Signals with Related CFC Filtered $Sinc^2$ Combinations Determining the Optimum CFC Filtering Method Based on Peak Values

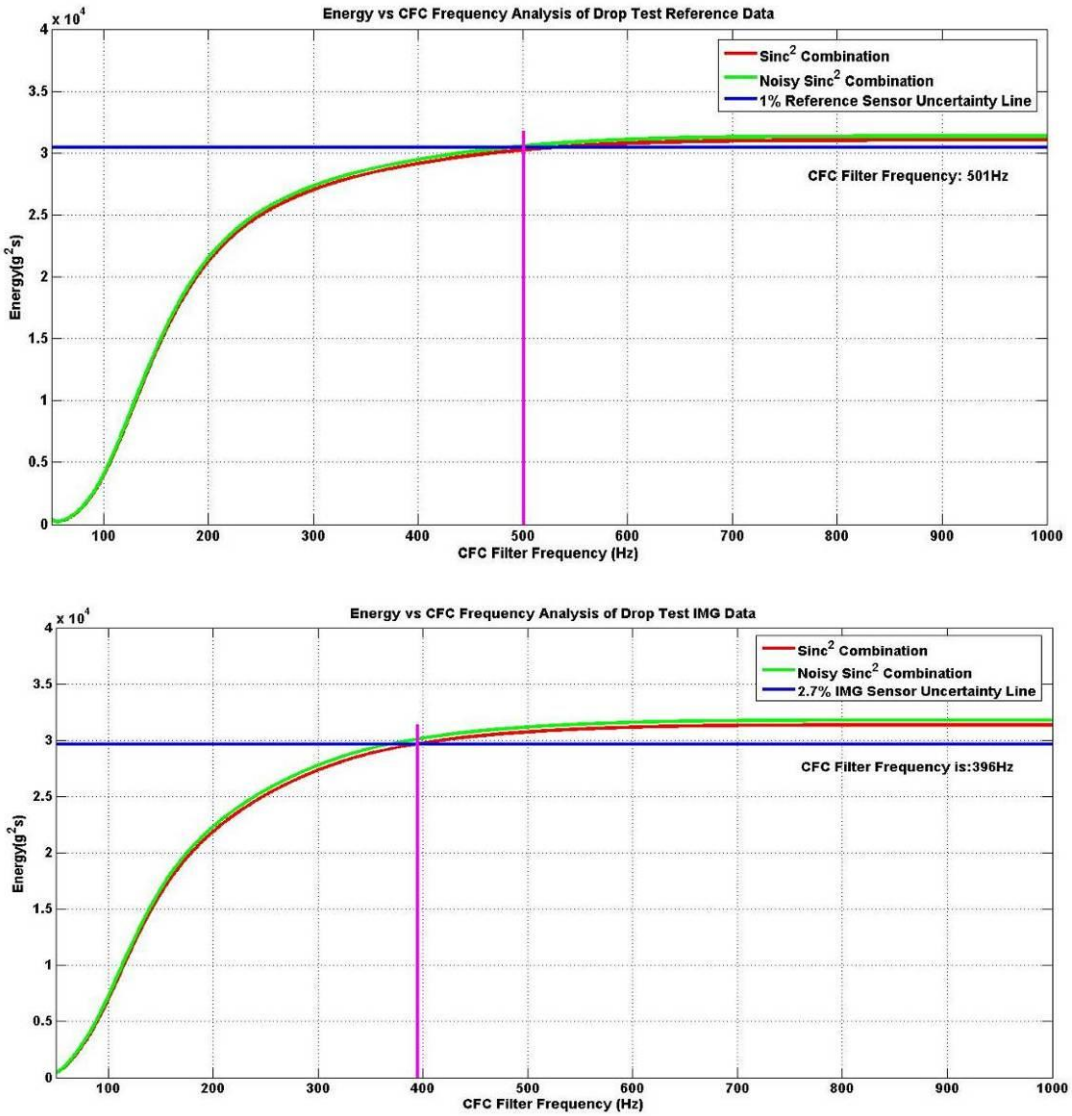

Figure 5.64 Determining the optimum CFC Filtering method based Energy Values for Reference (**top**) and IMG data (**bottom**). Blue lines represent lower levels of the uncertainty value for each sensor. Magenta lines show the frequency values where uncertainty lines intersect with peak values of True Signals, which were filtered with different CFC Filters, whose corner frequencies singly decrease from 1000Hz down to 1 Hz.

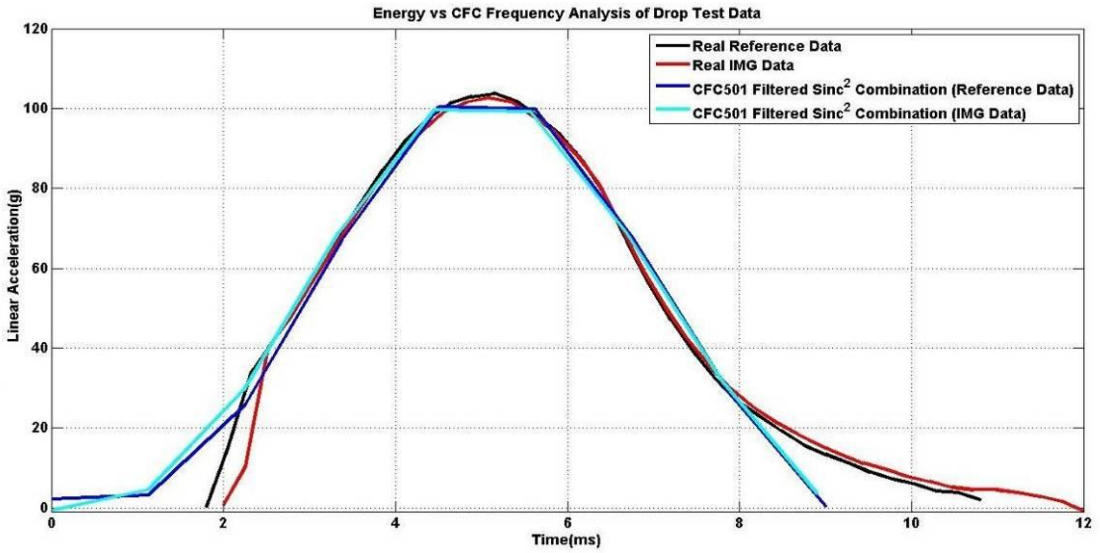

Figure 5.65 Comparison between Real Test Signals with Related CFC Filtered Sinc^2 Combinations Regarding Determining the Optimum CFC Filtering Method Based on Energy Values

Preliminary Conclusion

The reason why sinc^2 analysis was required was to determine the optimum corner frequency of CFC filter to be applied to test signals because some filtering problems were observed due to lack of information about amount of noise in each signal. In order to clarify this situation, the "true signal" of each reference data was generated by using several sinc^2 combinations that consisted of combinations of several numbers of sinc^2 functions. Percentages of matches between Reference data and true signals were in a range between 90-99% in terms of area under curve. This correlation was also accomplished for correlation between IMG data and corresponding true signals. These numbers proved that using combination of sinc^2 function may be a sufficient way to mimic real test signals. After generating true signals, the amount of noise in related test signal was computed and then added it into true signal to mimic a real test data pulse. One problem with this method might be the

limitation of phase shift for each $sinc^2$ function because the script is not capable to provide a phase shift for any $sinc^2$ function. Another problem for the $sinc^2$ analysis was because of strict windowing. It is known that FFT of a $sinc^2$ function is different than FFT of a strictly windowed $sinc^2$ function. However, in the practical case, it is necessary to window reference data to extract the region of interest of the signal.

After computing the optimum $sinc^2$ combinations for each test, the next step was to find out the most proper CFC filtering value for each test signal. Previously generated $sinc^2$ combinations were utilized as true signals and noisy true signals in this method. These signals were exposed to CFC filters whose corner frequencies were singly decreased from 1000 Hz down to 1 Hz. After that, optimum CFC filtering values of each sensor were obtained with respect to individual uncertainty values based on peak amplitude numbers. As a final step, real Reference and IMG data were plotted with CFC filtered noisy true signals of both data. Results show that CFC filtered noisy true signals were in the uncertainty range of both Reference and IMG data. This means new CFC filtering fashion based on peak values successfully worked to analyze test data.

Another way to compute the optimum CFC filtering values for each signal was to repeat the method explained above but this time, uncertainty values were re-calculated based on energy values of each test signal. As expected, uncertainty numbers based on energy values is greater than uncertainty numbers based on peak values because the analysis based on peak values considers only one point in a signal. In contrast, analysis based on energy values cover all data points. As a result of increase in uncertainty numbers, noisy true signals were exposed to stricter CFC filtering than CFC filtering based on peak analysis. Therefore, peak values of test signals in energy analysis were less than peak values in peak analysis. This was an

expected result because energy analysis was based on energy values of test signals, not based on the peak values. Interpretations for this method should be based on whole signal, not only one point, where the peak value of the signal. Consequently, energy based method needs more understanding to determine whether this method is useful for data analysis or not.

REFERENCES

1. Martin, P. G., Crandall, J. R., Pilkey, W. D., Chou, C. C., Fileta, B. B. Measurement Techniques for Angular Velocity and Acceleration in an Impact Environment. *SAE 970575, Proceedings of the SAE International Congress & Exposition (SAE SP 1264), Detroit Michigan* (1997).

2. Thomas, A. et al. Diffuse Axonal Injury and Traumatic Coma. *Annals of Neurosurgery, 12(6):564-574* (2004).

3. Pfister, B. J., Chickola, L., Smith, D. H. Head Motions While Riding Roller Coasters: Implications for Brain Injury. *Am. J. Forensic Med. Pathol., 30(4):339-345* (2009).

4. Fuller, C., Junge, A., Dvorak, J. A Six-Year Prospective Study of the Incidence, Etiology and Causes of Head and Neck Injuries in International Football. *Br. J. Sports Med.* (2005).

5. Fuller, C., Smith, G., Junge, A. An Assessment of Player Error as an Injury Causation Factor in International Football. *Am. J. Sports Med., 32:28S-32S* (2004).

6. Gerbeding, J. L., Steps to Prevent a Serious Public Health Problem. *Report to Congress on Mild Traumatic Brain Injury in the United States. pp. 1-5. The Centers for Disease Control and Prevention, Atlanta, GA* (2003).

7. Newman, J. A., Beusenberg, M. C., Shewchenko, N., Withnall, C., Fournier, E. Verification of Biomechanical Methods Employed in a Comprehensive Study of Mild Traumatic Brain Injury and the Effectiveness of American Football Helmets. *Journal of Biomechanics 38:1469-1481* (2005).

8. Edwards, K. J., Green, J. F. Analysis of the Inter-Relationship of Pedestrian Leg and Pelvis Injuries. *Proceedings of the 1999 International IRCOBI Conference on the Biomechanics of Impact, Sitges Spain* (1999).

9. Peng, R. Y., Bongard, F. S. Hypothermia in Trauma Patients. *Journal of the American College of Surgeons, 188(6):685-696* (1999).

10. Chidester, B., Isenberg, R. A., Final Report-The Pedestrian Crash Data Study. *National Highway Traffic Safety Administration, United States of America, 248* (2001).

11. Maki, T., Kajzer, J., Mizuno, K., Sekine, Y., Comparative Analysis of Vehicle-Bicyclist and Vehicle-Pedestrian accidents in Japan. *Accident Analysis and Prevention, Vol. 35, Issue 6, 927-940* (2003).

12. Toro, K., Hubay, M., Sotonyi, P., Keller, E. Fatal Traffic Injuries among Pedestrians, Bicyclist and Motor Vehicle Occupants. *Forensic Science International, 151(2-3):151-156* (2005).

13. Kong, L. B., Lekawa, M., Navarro, R. A., McGrath, J., Cohen, M., Margulies, D. R., Hiatt, J. R. Pedestrian-Motor Vehicle Trauma: An Analysis of Injury Profiles by Age. *Journal of the American College of Surgeons, 182(1):17-23* (1996).

14. Eigen, A. M., Martin, P. G. Identification of Real World Injury Patterns in Aid of Dummy Development. *In Proceedings of the 20th International Technical Conference on the Enhanced Safety of Vehicles, Washington, D. C. Paper No. 05-0219* (2005).

15. Craig, M. J., Viano, D. C., Bir, C. A. Jaw Loading Response of Current ATDs. *SAE International* (2009).

16. Annex I - Test Protocol for Occupant Safety Measurements and Injury Assessment. *North Atlantic Treaty Organization, Research and Technology Organization* (2006).

17. Nakos, J. T., Uncertainty Analysis of an Accelerometer DAQ System. *Sandia Report, SAND2000 – 1152* (2000).

18. Abernethy, R. B., Benedict, R. P., Dowdell, R. B. ASME Measurement Uncertainty. *Journal of Fluids Engineering 107, 161-164* (1985).

19. Basil, M., Sutherland, D., Yeung, H., Application of Probabilistic Uncertainty Methods (Monte Carlo Simulation) In Flow Measurement Uncertainty Estimation. *Flow Measurement, International Conference* (2001)

20. Martin, P. G., Hall, G. W., Crandall, J. R., Pilkey, W. D. Measuring the Acceleration of A Rigid Body. *Engineering and Technology Volume 5, No: 4*(1998).

21. Pfister, B.J., Chickola, L., Smith, D.H. Head Motions While Riding Coasters: Implication for Brain Injury. *Am J. Forensic Med. Path.; 30(4):339-345* (2009).

22. Gennarelli, T.A. Mechanism of Brain Injury. *J. Emerg. Med. 11 (Suppl 1):5-11* (1993).

23. Meaney, D.F., Margulies, S.S., Smith, D.H. Diffuse Axonal Injury. *Journal of Neurosurgery 95(6):1108 – 1110* (2001).

24. Margulies, S.S., Thibault, L.E. A Proposed Tolerance Criterion for Diffuse Axonal Injury in Man. *Journal of Biomechanics 25(8):917-923* (1992).

25. Funk, J.R., Cormier, J.M, Bain, C.E., Guzman, H., Bonugli, E. Validation and Application of a Methodology to Calculate Head Accelerations and Neck Loading in Soccer Ball Impacts. *SAE Technical Paper Series, 01-0251* (2009).

26. Shewchenko, N., Withnall, C., Keown, M., Gittens, R., Dvorak, J. Heading in Football. Part 2: Biomechanics of Ball Heading and Head Response. *Journal of Sports Med, 39 (Suppl. 1):i26-i32* (2005).

27. Rowson, S., Beckwith, J.G., Chu, J.J., Leonard, D.S., Greenwald, R.M., Duma, S.M. A Six Degree of Freedom Head Acceleration Measurement Device for Use in Football. *Journal of Applied Biomechanics, 27, 8-14* (2011).

28. Shewchenko, N., Withnall, C., Koewn, M., Gittens, R., Dvorak, J. Heading in Football. Part 1: Development of Biomechanical Methods to Investigate Head Response. *Journal of Sports Med, 39 (Suppl. 1):i10-i25* (2005).

29. Sulzer, J., Kamalakkannan, S.B., Wiechel, J., Guenther, D., Tanner, C.B., Morr, D.R. Simplified MADYMO Model of the IHRA Headform Impactor. *SAE Technical Paper Series* (2006).

30. Society of Automotive Engineers (SAE). Instrumentation for Impact Tests – Part I – Electronic Instrumentation. *SAE J211; Warrendale, PA* (1995).

31. Withnall, C., Shewchenko, N., Gittens, Dvorak, J. Biomechanical Investigation of Head Impacts in Football. *Br. J. Sports Med. ;39 (Suppl 1):i49-i57* (2005).

32. Pellman, E.J, Viano, D.C., Withnall, C., Shewchenko, N., Bir, C.A., Halstead, P.D. Concussion in Professional Football: Helmet Testing to Assess Impact Performance – Part 11. *Journal of Neurosurgery 58:78 – 96* (2006).

33. Scott, M.W. et al. Comparison of Human and ATD Head Kinematics During Low-Speed Rearend Impacts. *SAE Technical Paper Series, 930094* (1993).

34. Padgaonkar, A.J., Krieger, K.W., King, A.I. Measurement of Angular Acceleration of a Rigid Body Using Linear Accelerometer. *Journal of Applied Mechanics, pp. 552-556* (1975).

35. Hu, A.S. Validation and Instrumentation Module Using Rate Gyros and Linear Accelerometers. *Technical Report, Physical Science Laboratory, New Mexico State University* (1978).

APPENDICES

Appendix A

Model 64B Uncertainty

Methodology

Uncertainty analysis of model 64B sensor was more specific than ADXL001 sensor because each 64B sensor has its own specifications. In the test fixture, four model 64B sensors were attached two sides of the fixture. Two of them were located along the movement axis, and other two were perpendicular to the movement axis to measure transverse linear accelerations. In this part, uncertainty values of only two sensors located along movement axis were calculated. Like uncertainty analysis of the ADXL sensor, uncertainty analysis of model 64B sensor was mainly based on two specifications: non-linearity, and sensitivity. These two terms lead to precision error in sensor measurement. Additionally, zero-g-offset uncertainty was taken into account as a bias error.

Non-Linearity

Sensor uncertainty due to non-linearity was mentioned in model 64B specifications sheet provided from Measurement Specialties website (**Model 64B, Revision A).** According to the related sheet, non-linearity value for each sensor is equal to ±1% of readings.

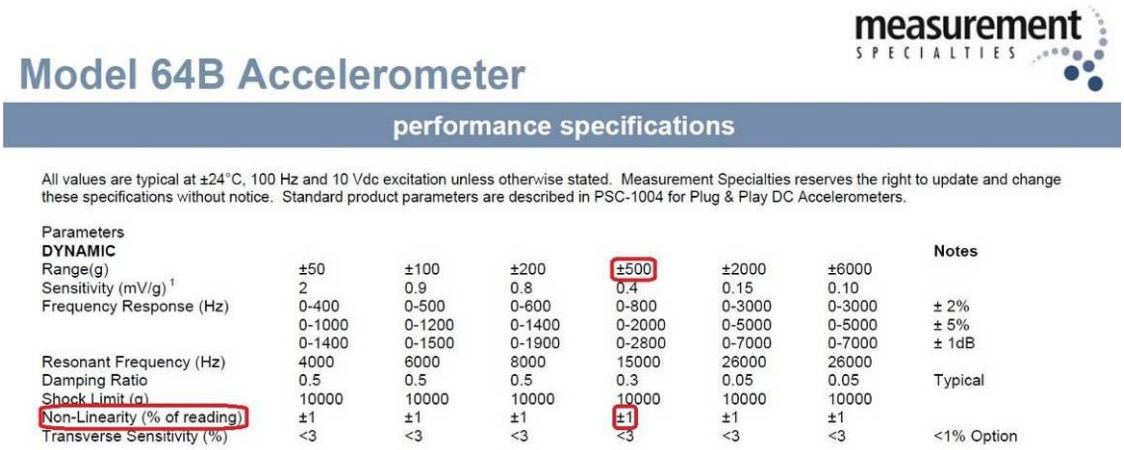

Model 64B Accelerometer

measurement SPECIALTIES

performance specifications

All values are typical at ±24°C, 100 Hz and 10 Vdc excitation unless otherwise stated. Measurement Specialties reserves the right to update and change these specifications without notice. Standard product parameters are described in PSC-1004 for Plug & Play DC Accelerometers.

Parameters							
DYNAMIC							**Notes**
Range(g)	±50	±100	±200	±500	±2000	±6000	
Sensitivity (mV/g) [1]	2	0.9	0.8	0.4	0.15	0.10	
Frequency Response (Hz)	0-400	0-500	0-600	0-800	0-3000	0-3000	± 2%
	0-1000	0-1200	0-1400	0-2000	0-5000	0-5000	± 5%
	0-1400	0-1500	0-1900	0-2800	0-7000	0-7000	± 1dB
Resonant Frequency (Hz)	4000	6000	8000	15000	26000	26000	
Damping Ratio	0.5	0.5	0.5	0.3	0.05	0.05	Typical
Shock Limit (g)	10000	10000	10000	10000	10000	10000	
Non-Linearity (% of reading)	±1	±1	±1	±1	±1	±1	
Transverse Sensitivity (%)	<3	<3	<3	<3	<3	<3	<1% Option

Figure A.66 Non-Linearity Numbers of Model 64B

Sensitivity

Each model 64B sensor has its own sensitivity number. This sensitivity number was mentioned in front of each sensor box. Serial numbers of two sensors located along movement axis were A063205 and A063203. Sensitivity of A063205 and A063203 were equal to 0.41mV/g and 0.37mV/g, respectively. Uncertainty due to the sensor sensitivity was accepted as zero because each sensor has a unique calibrated sensitivity.

Cross-Axis Sensitivity

According to model 64B specifications sheet, uncertainty due to transverse sensitivity was less than 3% of readings. However, in this part of the project, tests were performed along only one axis. This means uncertainty due cross-axis sensitivity

DID not affect total uncertainty of the system so long as cross-axis accelerations were minimized.

Results

As the result of model 64B uncertainty analysis, factors due to uncertainty were determined and according to related datasheet, the effect of each component was scrutinized and then combined with the contribution of RSS method. According to the analysis done previously, only non-linearity and sensitivity numbers were taken into account.

$$S = \left[(1)^2 + (0)^2\right]^{\frac{1}{2}}$$

$$U_{RSS} = \left[(1)^2 + \left((0)^2\right)\right]^{\frac{1}{2}}$$

$$U_{RSS} = 1\%$$

Conclusion of Model 64B Uncertainty Analysis

According to calculations related to the uncertainty analysis of model 64B sensor, 1% uncertainty ± 3% cross-axis sensitivity uncertainty were calculated. Results emphasize that because of high precision level, model 64B is capable to be a Reference sensor for IMG validation tests.

Appendix B

Gyroscope Testing – Detailed Results

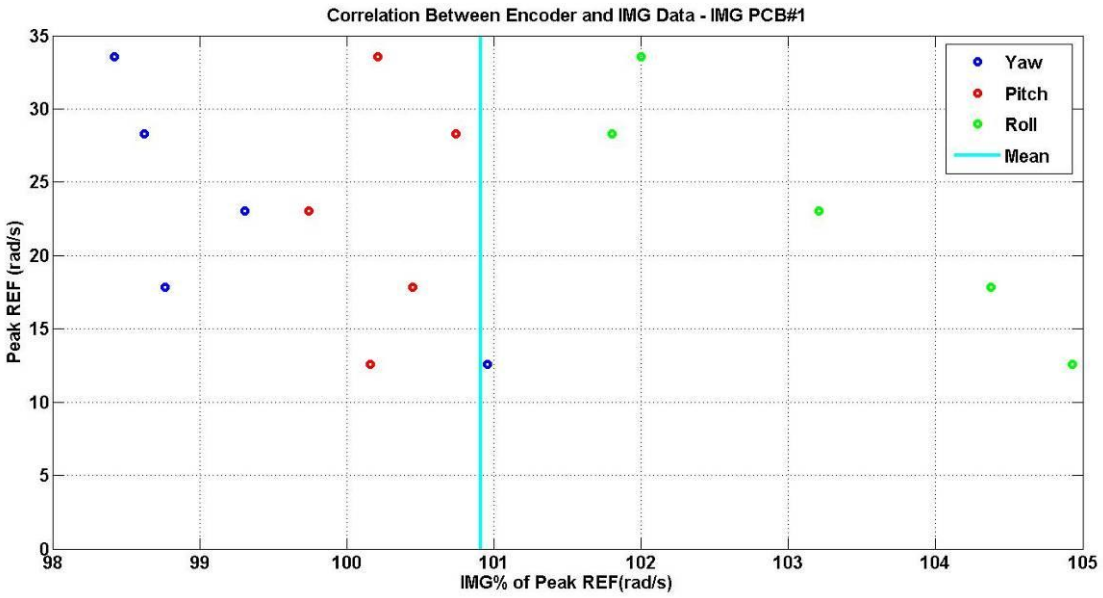

Figure A.67 System Bias and Random Uncertainty Values for IMG PCB#1.

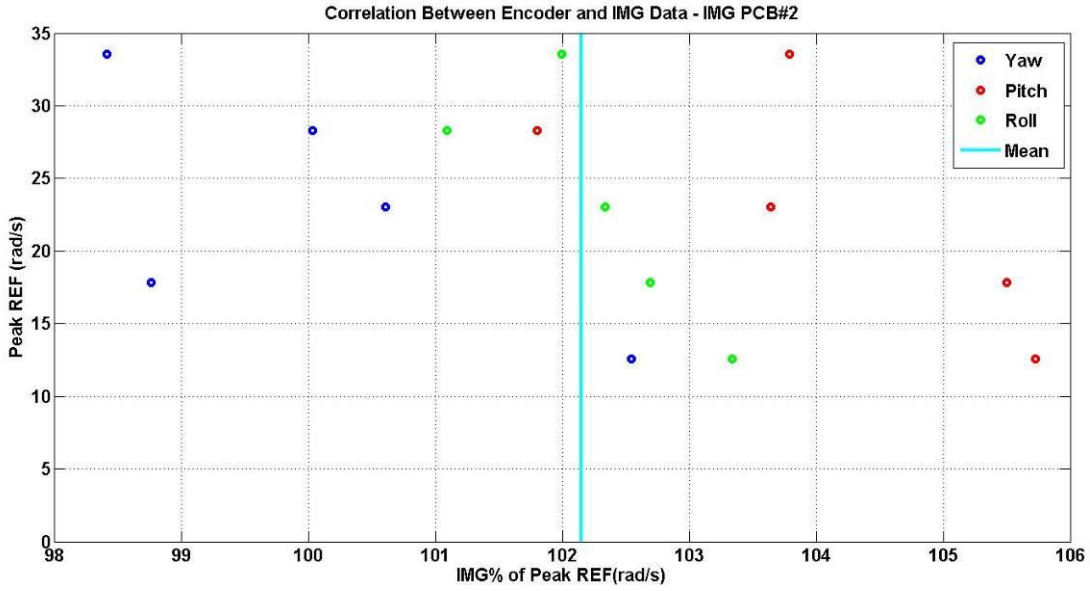

Figure A.68 System Bias and Random Uncertainty Values for IMG PCB#2.

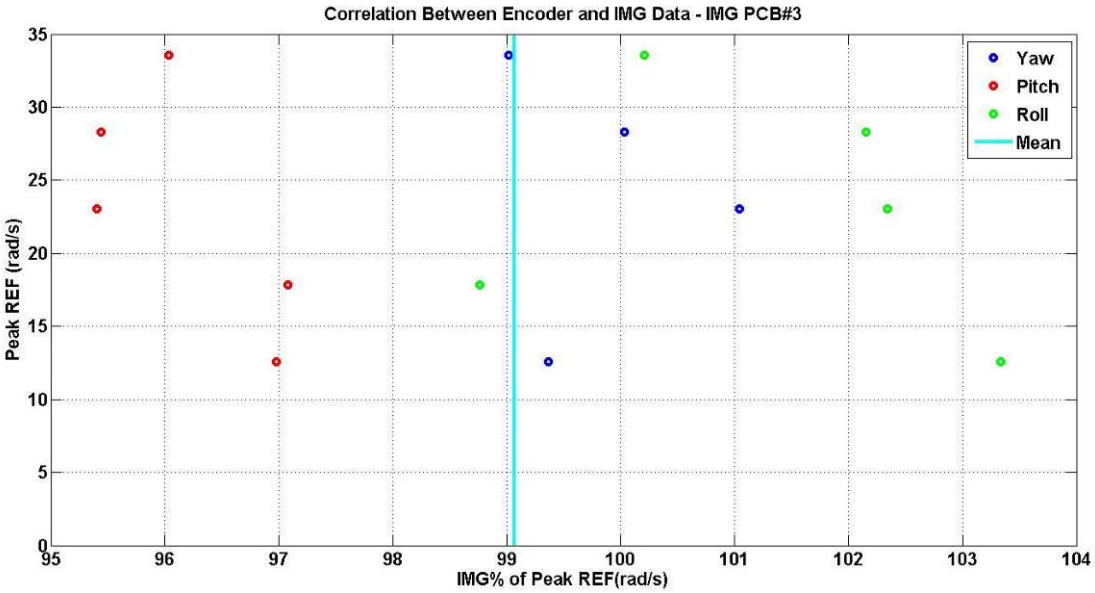

Figure A.69 System Bias and Random Uncertainty Values for IMG PCB#3.

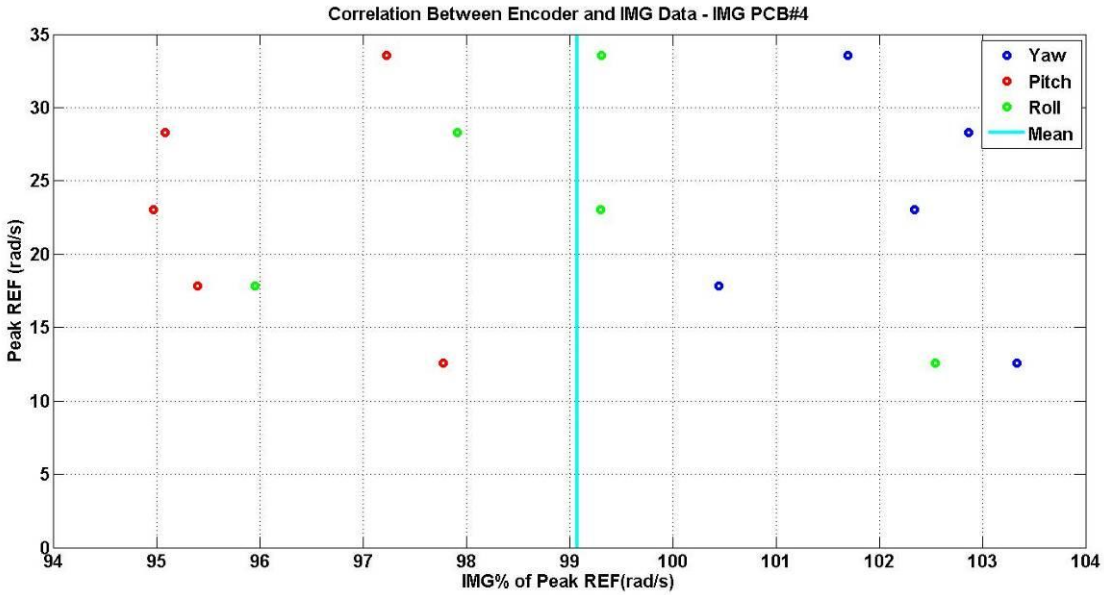

Figure A.70 System Bias and Random Uncertainty Values for IMG PCB#4.

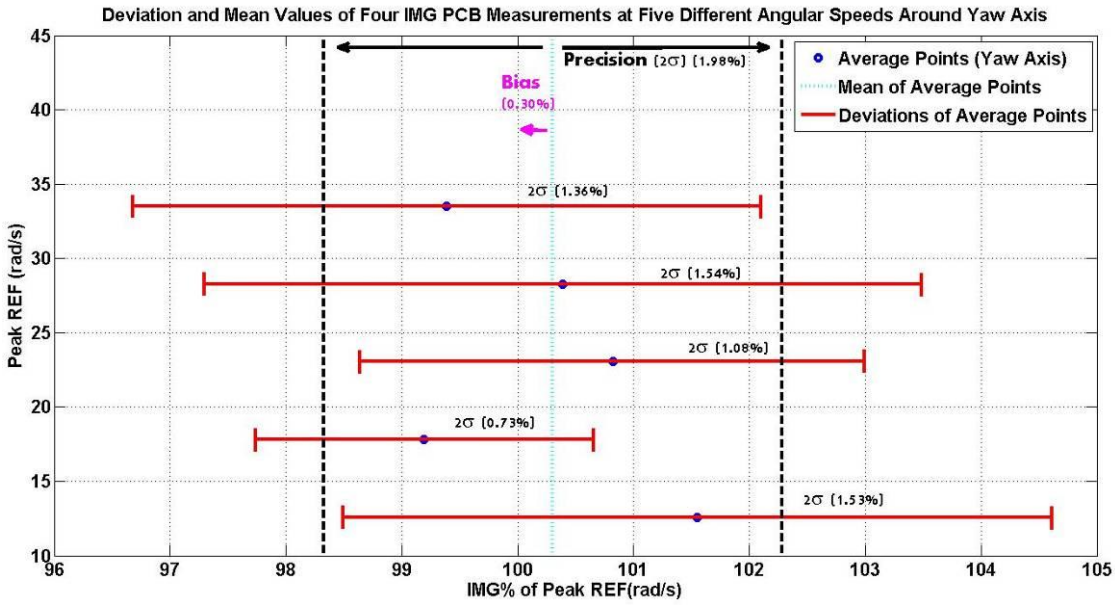

Figure A.71 System Mean and Deviation Values Based on Yaw Axis Test Results

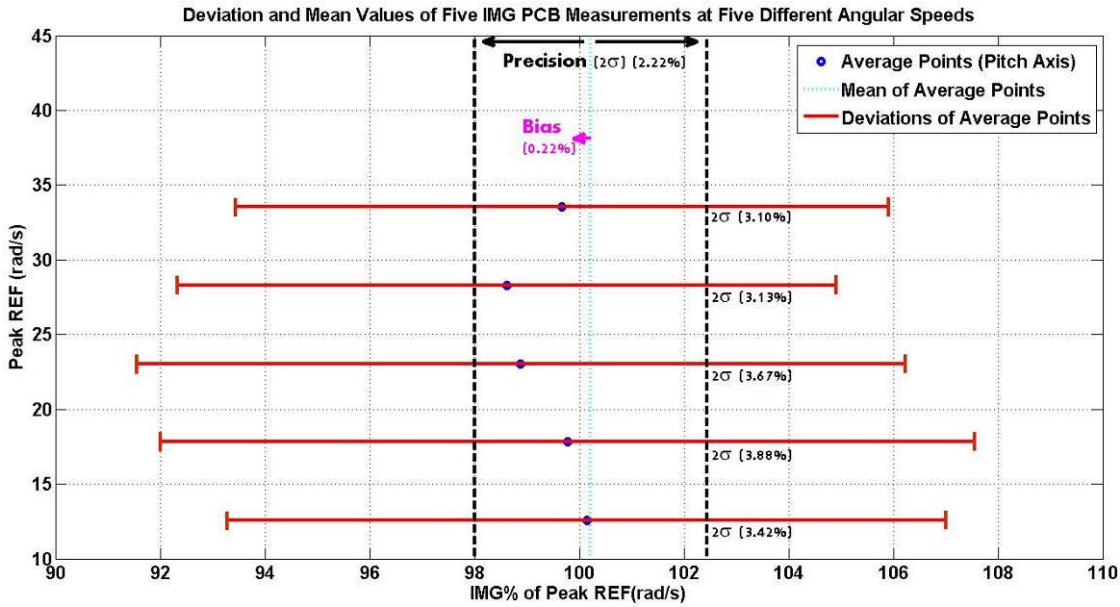

Figure A.72 System Mean and Deviation Values Based on Pitch Axis Test Results

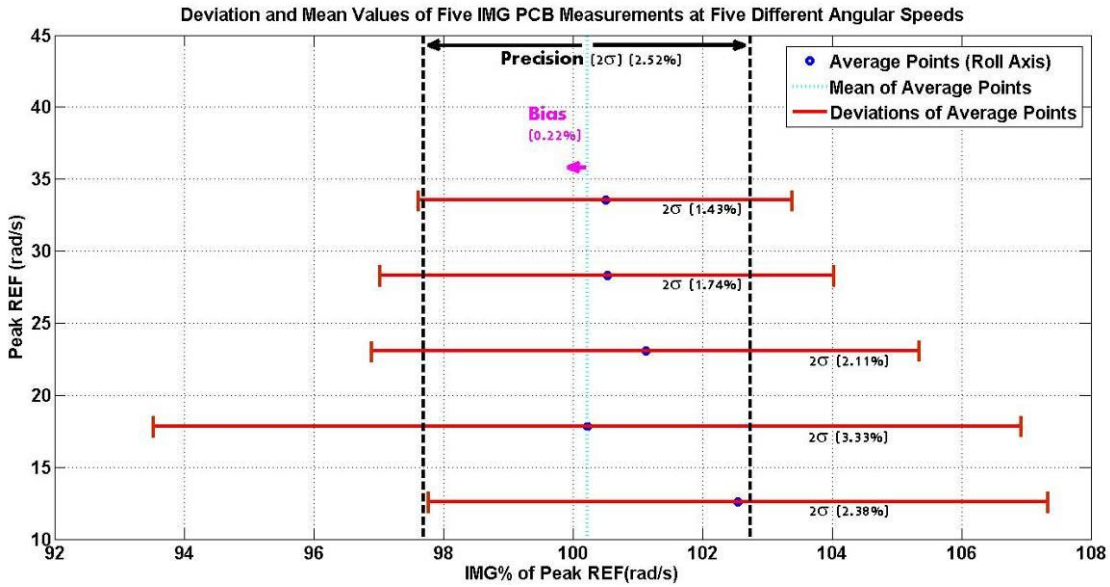

Figure A.73 System Mean and Deviation Values Based on Roll Axis Test Results

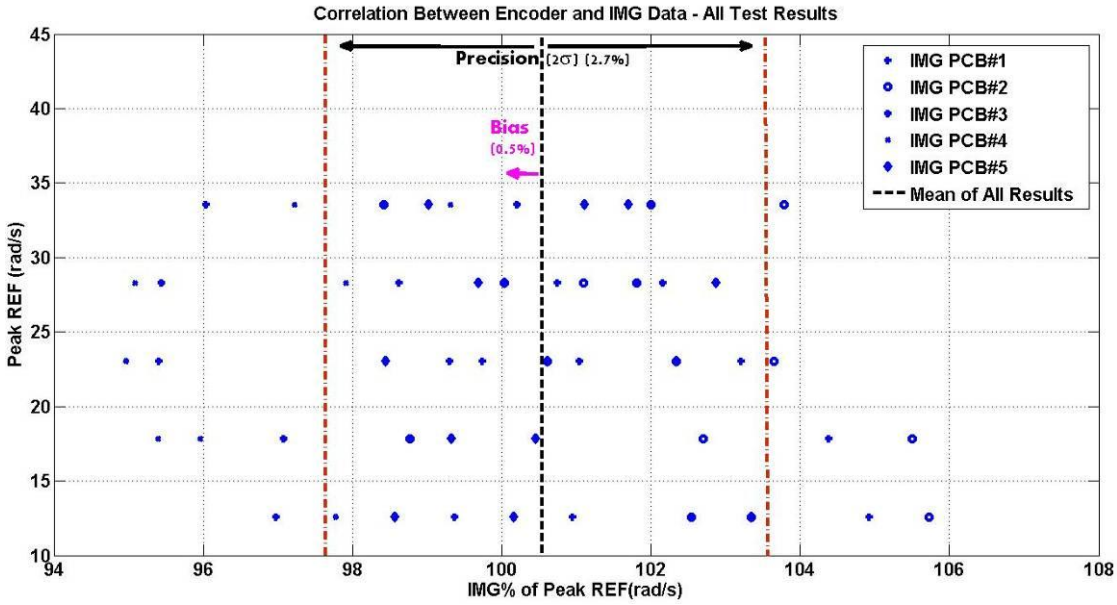

Figure A.74 System Mean and Deviation Values of All Gyroscope Test Results